A bulk and fraction-specific geochemical study of the origin of diverse high-grade hematitic iron ores from the Transvaal Supergroup, Northern Cape Province, South Africa

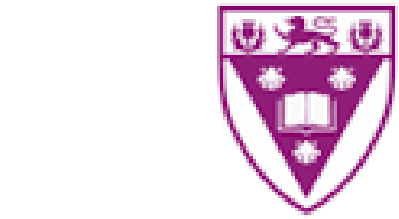

A thesis submitted to Rhodes University in fulfilment of the requirements for the degree of Master of Science

William Moloto

Supervised by

Professor H Tsikos

Co-Supervised by

Professor GM Watkins

February 2017

Department of Geology, Rhodes University

Abstract

The Paleoproterozoic Transvaal Supergroup in the Northern Cape Province of South Africa is host to high-grade, Banded Iron Formation-hosted hematite iron-ore deposits and is the country's most important source of iron to date. Previous studies suggest the origin of these iron ores to be ancient supergene, and that the ore forming process would have therefore pre-dated deposition of the basal Mapedi shales of the Olifansthoek Supergroup that unconformably overlies the Transvaal strata. The nature of the protolith to the ores has been suggested to be largely BIF of the Asbestos Hills Subgroup, and mainly the Kuruman BIF. The work presented in this thesis seeks to provide insights into the diversity of processes that are likely to have been involved during the genesis of these high-grade iron ores, in the context of constraining the pre-ore lithologies and the relative role of supergene-style, largely residual enrichment processes versus any possible metasomatic hydrothermal effects.

This study had as primary focus the application of combined bulk and fraction-specific geochemical applications on representative iron-ore samples from four different localities in the Northern Cape Province, namely King/Khumani, Beeshoek, Heuninkranz and Hotazel. The collected samples show a variety of textures and also capture different pre-unconformity stratigraphic sections of BIF. The key objective was to assess whether the fraction-specific analytical results could provide any firm constraints for the origin of the ferrous and non-ferrous matrix fractions of the ores, namely whether they represent any combinations of protolith residue, allochtonously-introduced detritus or hydrothermally-derived material, and whether the results are comparable and consistent across all samples studied. In particular, constraints were sought as to whether the ore protolith was exclusively BIF or may potentially have contained at least a fraction of other lithologic types, such as shale; and whether there is sufficient evidence to support solely a supergene model for the ores or the data suggest other more epigenetic models of ore formation involving the action of hydrothermal fluids.

Bulk-rock geochemical analyses reveal the overwhelming dominance of Fe-oxide (as hematite) in all samples, at concentrations as high as 99 wt.% Fe_2O_3. Major and trace-element abundances of all samples were re-calculated assuming only iron addition from the postulated protolith (average BIF and shale), and the results revealed atypical enrichments in the iron ores by comparison to average BIF, and more shale-like relative abundances when normalised against the Post-Archaean Average Shale (PAAS). Specifically, BIF-normalised diagrams show relative enrichments by as much as 53-95% for Al_2O_3; 11-86% for TiO_2; and 4-60% for

P_2O_5. By contrast, PAAS-normalised values display enrichments of 1-3% for Al_2O_3, 0.2-3% for TiO_2, and 3-13% for P_2O_5. Similar observations can be made for the greatest majority of trace elements when normalised against average BIF as compared to normalisation against PAAS. A suite of trace element that include alkali earths (e.g. Ba, Sr) and transition metals (e.g. Ni, Zn) show enrichments that are unrelated to the apparently detrital siliciclastic fraction of the ores, and are therefore linked to a possible hydrothermal input.

Fraction-specific extractions were performed *via* the adaptation of existing dissolution protocols using oxalic acid (iron-oxide fraction) followed by HF digestion (silicate-fraction). The analyses of the produced aliquots using ICP-MS techniques, focused mainly on the REE abundances of the separated ferrous and non-ferrous matrix fractions and their comparisons to bulk-rock REE signatures. The results lend further support to the suggestion that the ore samples contain a predominant shale-like signal which does not directly compare to published REE signatures for supergene or hydrothermal BIF-hosted iron-ore deposits alike. The data therefore collectively point to a post-unconformity epigenetic hydrothermal event/s of iron ore-formation that would have exploited not only BIF but also shale as suitable pre-ore protolith.

Acknowledgements

It would not be possible to complete this work without the help and guidance of the kind people that surround me to only some of whom it is possible to give particular mention here.

I thank Prof Harilaos Tsikos, my supervisor for providing me with the opportunity and resources to conduct fundamental research, thus paving the way for me to understand and appreciate dynamic thinking in research (as you always said: “research is all about ideas, if you have ideas you can make anything out of nothing”). I am humbled and honoured to have worked under your supervision. Your endless sense of humour also made working with you truly special. Thank you Prof “T”.

To Professor Gary Watkins, my chemistry supervisor: this work would not have been possible without free access to the labs and equipment. Thank you for making inorganic chemistry enjoyable and rewarding to me. You have laid the foundation of fundamental chemistry in me, so thank you for your contribution to this work.

To the PRIMOR group of 2014-15 (Paul, Vlassis, Sihle, Xolane, and David), I want to thank you for your contribution to this work and the ever fun Friday meetings I will always remember. Your endless engagement to this work has been really very important to me.

To my girlfriend Nonhlanhla, thanks for the support and encouragement.

To my sisters Ginah and Oupa, thank you for your constant support.

To my grandma, thank you for your prayers and support.

To my “F12” colleagues, your support and encouragement made coming to the lab as fun as it was challenging. I want to thank particularly Siya for teaching me how to operate the ICP-OES instrument, and Mr Magaji for his support and assistance with speciation chemistry.

A special appreciation must go to ASSMANG Ltd for providing access to the drillcores and samples for this study and for funding my project through PRIMOR. Affording me the opportunity to be part of such exciting fundamental research on iron and manganese ores is really appreciated.

Finally, a great thank-you to Rhodes University for becoming the academic home to me for 6 years, where every department and lab were always open for me to carry out this and other research. Thank you wholeheartedly.

Table of Contents

Table of Figures

1 Introduction

1.1 General

A vast amount of iron ore mined today comes from high-grade banded iron formation (BIF)-hosted deposits (Gutzmer & Beukes, 2008; Bekker *et al.*, 2010). The majority of these high-grade iron ore deposits are located in countries of the southern hemisphere that contain large occurrences of BIF, and specifically in the Harmersley District of Australia; the Carajas, Quadrilatero Ferrifero and Urucum Districts of Brazil; and the Transvaal Supergroup of South Africa (Fig. 1; Bekker *et al.*, 2010). Other, relatively smaller deposits have been exploited in the past or are presently being mined in India, USA/Canada (low-grade ores known as *taconites;* James, 1954) and the Ukraine (Krivoj Rog Supergroup). In South Africa, the iron-ore deposits associated with Superior-type BIFs of the Transvaal Supergroup in the Northern Cape Province (Beukes *et al.*, 2003), are by far the most economically important resources of iron for the country (Figure 1).

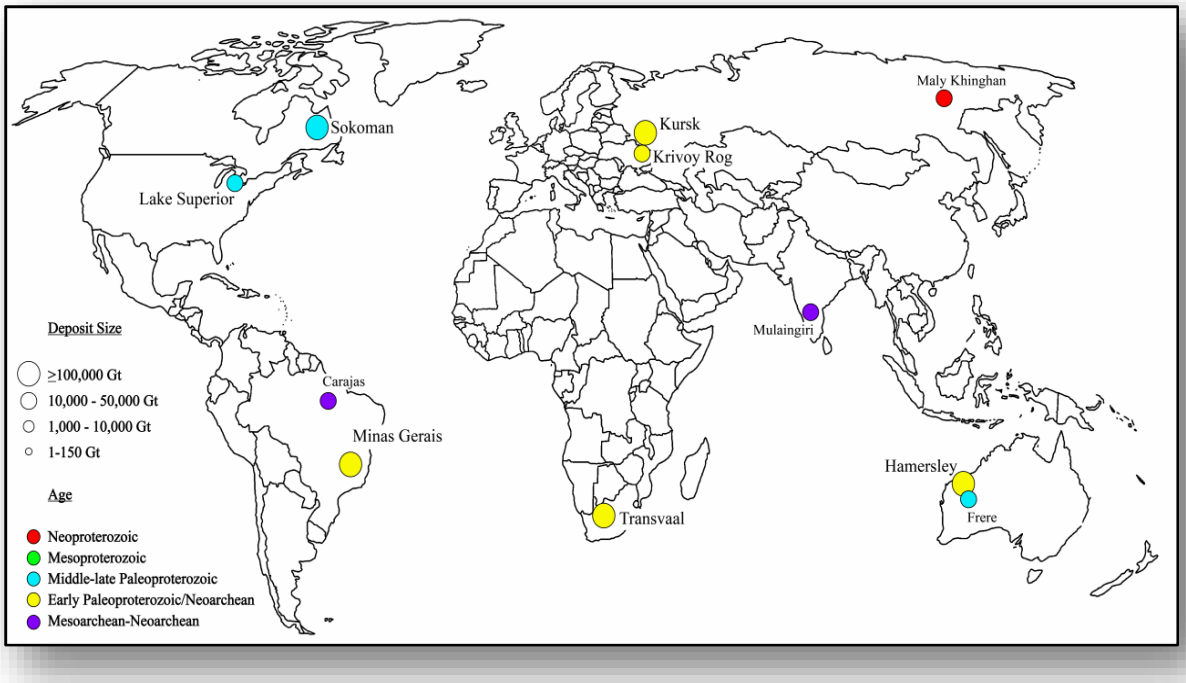

Figure 1. Distribution of major high-grade iron ore deposits and districts mined currently across the world (after Bekker *et al.*, 2010).

Other, smaller occurrences of sub-economic iron-ore deposits in South Africa are vein- and

lode-type deposits which are located in the Northern Cape, North West and Limpopo Provinces, and hold mainly specular hematite which is of economic interest chiefly to the pigment industry (Astrup *et al.*, 1998). There is also V-rich titaniferous magnetite in ultra-mafic magmatic rocks of the Bushveld Complex in the Gauteng, North West and Mpumalanga Provinces (Astrup *et al.*,, 1998). Although the Bushveld ores are targeted primarily for their V and Ti endowment, the iron content of these ores ranges from 50-67 wt. % Fe metal which has been - and currently still is - considered as economic. The presence of magnetite in the felsic magmatic rocks in the Phalaborwa Complex – where magnetite accounts for approximately 27% of the main ore body – is another economically noteworthy source of iron in terms of the South African iron ore market (Astrup *et al.*, 1998).

1.2 Banded iron formation (BIF): definition & classification

Banded iron formation is a chemically precipitated sedimentary rock that is composed of thin (millimetre- to centimetre-scale) alternating layers containing chert, iron oxide, iron silicates and/or iron carbonates, usually in poly-minerallic combinations (Gross, 1980). By convention, a rock must contain at least 15 wt. % of total iron to be classified as a BIF (James, 1954). The Precambrian period right up to the late Palaeoproterozoic (3.8-1.8 Ga) marks the time window during which BIF was primarily deposited (Bekker *et al*., 2010). BIFs occur in a variety of different stratigraphic settings with no consistent lithological associations before or after BIF deposition. However, Gole and Klein (1981) attempted to categorise different types of BIF, and the resultant classes are still in use today.

1. **Lake Superior-type** BIFs are banded, cherty and occasionally oolitic, iron-rich sedimentary accumulations, thought to have been deposited in a near-shore continental-shelf environment. Lithologically, they would have formed in association mainly with carbonate and generally only minor siliciclastic sedimentary rocks, occasional black shales and usually minor to absent volcanic rocks (James, 1954; Gross, 1980; Gole & Klein, 1981). The lack of a clear spatial association with volcanic rocks for these BIFS and their almost exclusively Palaeoproterozoic age, are key diagnostic characteristics (Gross, 1980; Beukes and Gutzmer, 2008). The high-grade iron ore deposits of Sishen and Kolomela (Sishen South) in the Northern Cape Province and Thabazimbi in the Limpopo Province of South Africa, are all considered to have formed at the expense of Lake Superior-type BIF (Beukes & Gutzmer, 2008). Other noteworthy iron-ore deposits associated with Lake Superior-type BIF are the

homonymous ores in the Lake Superior region of N. America; those of the Krivoj Rog Basin in the Ukraine; the *itabirites* of Minas Gerais, Brazil; as well as the world-class ores in Hamersley Province of Western Australia (Fig. 1; Bekker *et al.*, 2010).

2 **Algoma-type** BIFs are banded, cherty iron formations associated with greywacke-dominated sedimentary units and commonly known to be restricted to Archean greenstone belts (Klein, 2005). These BIFs have genetic and spatial association with volcanic rocks and are deposited along volcanic arcs and related submarine fracture systems (Gross 1980; Bekker *et al.*, 2010). Commercial iron ore deposits associated with Algoma-type BIF can be found in Brazil and India (Fig. 1).

1.3 Review of BIF and BIF-hosted iron-ore literature

In 1922, John W. Gruner, a pioneer in Precambrian geological research, published his first scientific paper on the origin of sedimentary BIF in the Mesabi Range, northern Minnesota. Gruner went on to publish several other scientific papers on the origin of BIF (Gruner, 1924, 1926, 1930); the mineral composition and structure of greenalite (Gruner, 1936), stilpnomelane (Gruner, 1937) and minnesotaite (Gruner, 1944); as well as a paper on the discovery of putative micro-organisms in Archean chert pebbles (Gruner, 1925). Harold James, another pioneer with regard to Precambrian BIF research, was best known for his interpretations of the petrology of structurally complex BIF (Barton, 2002). Harold James focused much of his research on the BIFs of northern Michigan, USA, which gave him the opportunity to publish three classic papers (James, 1954, 1955 and 1958). The paper entitled "Sedimentary Facies of Iron-Formation" published in the journal "Economic Geology" (James, 1954) ignited renewed interest in BIF and researchers once again began publishing papers on the origin, sedimentology, geochemistry and mineralogy of these unusual yet economically very important rocks.

Following numerous publications, UNESCO (1973) published a collection of papers in a volume titled "Genesis of Precambrian Iron and Manganese Formations". The Society for Economic Geologists (SEG) also published a special edition in the same year entitled: "Precambrian Iron-Formations of the World", which represents a compilation of papers on the spatial distribution of BIF, applications of various sub-disciplines (e.g. mineralogy, geochemistry) pertaining to BIF research, and on conceptual theories regarding the genesis of BIF and their associated iron ore deposits. Further research into the enigma of BIF over the

next 20 years resulted in the publication of two volumes in "Developments in Precambrian Geology". The first volume, published in 1982, was entitled: "Precambrian Banded Iron-Formations: Physicochemical Conditions of Formation" which was followed one year later by a volume titled "Iron-Formation: Facts and Problems". The latter publication includes research on the origin, genesis and bulk geochemical composition of BIF, rare earth element analysis, oxygen isotope applications and paleontological evidence of BIFs from around the world.

In 2008, Profs Steffen Hagemann, Carlos Rosière, Jens Gutzmer and Nicolas Beukes received enthusiastic support from the research community and industry to assemble a series of papers published in a special volume of Economic Geology, that captured the latest innovative research conducted on high-grade BIF-related iron ore deposits throughout the world (Hagemann *et al*., 2008). This publication in "Reviews in Economic Geology 15" titled: "Banded Iron Formation-related High-Grade Iron Ore" contains a collection of papers with emphasis on the origin, timing of iron mineralization, hypogene alteration, structural control, mineralogy, geochemistry of iron ores and the importance of hydrothermal *versus* supergene processes from both established and newly discovered iron-ore districts and deposits. This volume represents the latest summary of knowledge on high-grade BIF-related iron ore deposits.

A substantial amount of research has also been carried out specifically on the BIFs of the Transvaal Supergroup in South Africa, most notably work by La Berge (1966), Button (1976), Beukes (1983, 1984, 1986), Lamprecht and Hälbich (1988), Hälbich and Altermann (1992), Hälbich *et al*. (1992, 1993), Bau (1993), Tsikos (1994, 1999), Horstmann and Hälbich (1995), Tsikos and Moore (1997, 2005), Tsikos *et al*. (2003, 2010) and Beukes and Gutzmer (2008). There has also been some research specifically carried out on the BIF-hosted iron ores of the Transvaal Supergroup, in the Northern Cape Province of South Africa, by Beukes *et al.* (2003), Carney and Mienie (2003), Gutzmer *et al.* (2005), Gutzmer *et al*. (2006), Alchin *et al.* (2008), de Kock *et al.* (2008) and Gutzmer *et al.* (2008).

1.4 Review of genetic modelling of BIF-hosted iron-ores

The genesis of high-grade iron ore deposits in direct association with BIF is still not very well understood, with many aspects of the ore-forming process/es remaining elusive (Gutzmer *et al.*, 1996). There are iron-ore deposits that are suggested to be unequivocally hydrothermal in origin, such as those in the Hamersley Province of Australia (Taylor *et al.*, 2001). However, most BIF-related iron-ore deposits have at least a distinct supergene overprint due to deep, geologically recent lateritic weathering, which obscures every attempt to constrain and model the ore-forming process holistically (Beukes *et al*., 2003; Dalstra and Guedes, 2004; Gutzmer *et al*., 2008; Hagemann *et al*., 2008; Ramanaidou and Morris, 2010; Angerer *et al*., 2012). Albeit somewhat controversial, syngenetic models have also drawn some attention, whereby chert-free BIF may have formed during processes of early diagenetic silica loss in the primary depositional environment (Lascelles, 2006a,b).

Most researchers propose metallogenic models for the genesis of high-grade BIF-hosted hematite iron ore deposits which implicate epigenetic fluid-rock interaction processes of a supergene and/or hydrothermal nature (Taylor *et al*., 2001; Beukes *et al*., 2003; Morris, 2003; Dalstra and Guedes, 2004; Thorne *et al*., 2004; Lascelles, 2006a; Lascelles, 2006b; Lobato *et al*., 2008; Roy and Venkatesh, 2009). In this light, Beukes *et al*. (2003) classified hematite high grade ore and recognise three general genetic types of deposits, namely *hydrothermal*, *ancient supergene* and *supergene-modified* deposits, the latter being essentially a hybrid of the previous two types.

Arguably the most controversial aspect in the genetic modelling of some iron-ore deposits is whether they have formed *via* primarily hydrothermal processes or through ancient supergene enrichment which was subsequently obscured through burial compaction. Indeed, this is the subject of intense debate on some high-grade BIF-hosted hematite deposits (Hagemann *et al*., 2007). The “Sishen-type” iron ores found in association with BIF of the Transvaal Supergroup, on the Maremane dome in the Northern Cape Province of South Africa, are thought to represent the main type-example of such deposits (van Schalkwyk and Beukes, 1986; Beukes et al., 2003; Fig. 1).

The “Sishen-type” ores are believed to be the lithified products from previous saprolitic ores that developed in the ancient supergene environment (Beukes *et al*., 2003). The iron ores

typically occur immediately below a major regional unconformity, which separates the Transvaal Supergroup from the overlying Olifantshoek Supergroup. This unconformity is host to numerous iron-ores but also manganese deposits, and appears to have played a major role in the genesis of these deposits in the Northern Cape region (Tsikos *et al*., 2003, Beukes *et al*., 2003; Moore *et al*., 2011; Fig. 2). This is due to the folded and tilted nature of the Transvaal Supergroup which results in the unconformity transecting a variety of rock types from the Transvaal Supergroup (Beukes *et al*., 2003). High-grade (65-67 wt. % Fe) iron-ore deposits have developed in locations where the unconformity has truncated the banded iron-formations (BIF) of the Transvaal Supergroup (Beukes *et al*., 2003, Fig. 2). Thick, economically important deposits of high-grade iron ore specifically occur in karstic settings, where the BIF of the Asbestos Hills Subgroup has slumped into dissolution structures in the underlying Campbellrand carbonates (von Plehwe-Leisen and Klemm, 1995; Beukes *et al*., 2003; Carney and Mienie, 2003; Fig. 3). In areas outside of these karstic settings, thin layers (1-2m thick) of high-grade hematite ore are also known to be preserved below the Transvaal-Olifantshoek unconformity (Grobbelaar *et al*., 1995; Beukes *et al*., 2003).

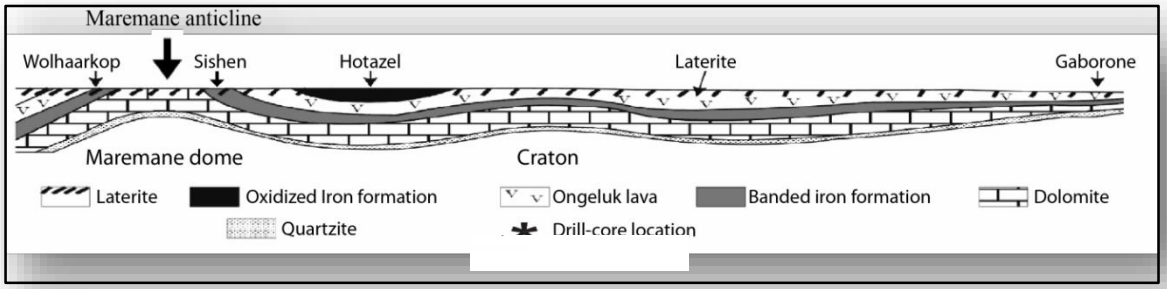

Figure 2: A cross-section of the Transvaal Supergroup illustrating the truncation of the stratigraphy by the Transvaal-Olifantshoek regional unconformity. The Maremane anticline and associated iron ore deposits (Sishen and Wolhaarkop) are shown (modified after Beukes *et al*.,2003).

The hard hematite iron ores in ancient supergene deposits of South Africa are characterized by mainly laminated, massive and brecciated iron ore units (Beukes *et al*., 2003). The karstic setting of these deposits results in highly irregular thickness variations throughout the ore-bodies. The unconformity-bound nature of the deposits and their common association with these karstic structures (Fig. 3) forms the basis for their suggested supergene-related genesis by various workers (Beukes *et al*., 2003; Dalstra and Rosière, 2008). These large, high-grade hematite iron ore deposits are thought to have formed by a series of processes that have upgraded the Asbestos Hills BIF into an economically viable high-grade iron ore. These

include dissolution-induced collapse of BIF into karstic depressions, and effective leaching of SiO_2 from the Asbestos Hills BIF through circulation of meteoric waters during sub-surface weathering (Grobbelaar *et al.*, 1995; von Plehwe-Leisen and Klemm, 1995; Beukes *et al*., 2003; Carney and Mienie, 2003). The close link between the Maremane ores and supergene processes is strengthened by the fact that paleomagnetic data indicate that the ores were formed at low latitudes near the equator, where warm humid tropical conditions favour possible supergene enrichment processes (Evans *et al*., 2001).

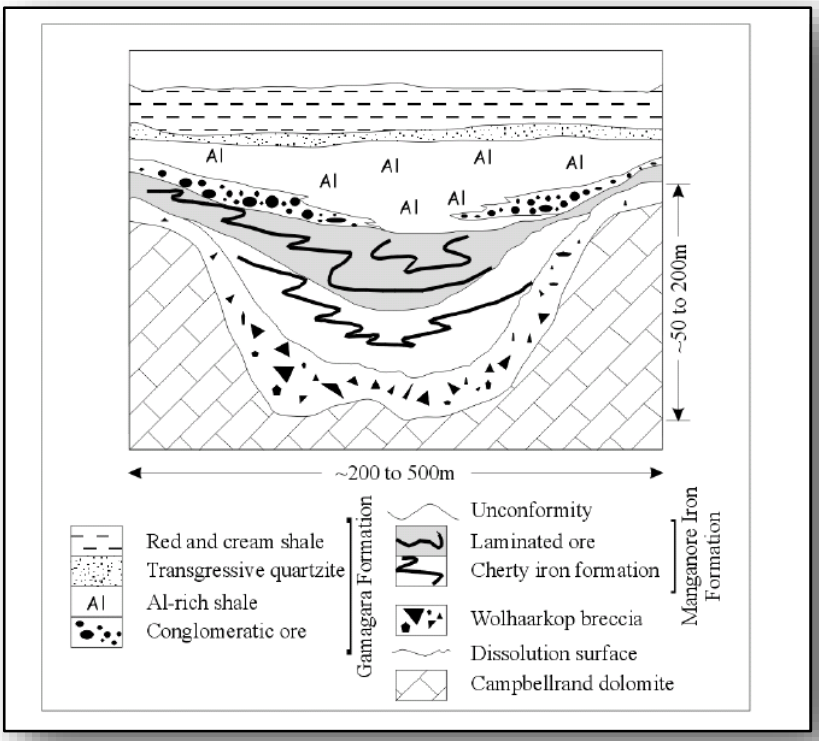

Figure 3: A schematic cross-section of a typical karstic sinkhole hosting massive Sishen-type iron ore in the Transvaal Supergroup (modified after Beukes *et al.,* 2003).

Iron-ore deposits of a strictly hydrothermal origin exhibit distinct characteristics that distinguish them from ancient supergene ones. As mentioned earlier, the Australian deposits in the Hamersley Province represent classic examples in this category. These hydrothermal ores do not appear to be associated with any unconformity surfaces, and mineralisation grades laterally or from the bottom upwards into an unmineralised BIF (Figure 4; Taylor *et al*., 2001; Beukes *et al*., 2003). The main ore bodies usually occur above black shale units (Taylor *et al.*, 2001), and the mineralisation in hydrothermal-type ores is suggested to be associated with

faulting (Taylor *et al*., 2001; Thorne *et al*., 2008). The high-grade hematite iron ores develop as a result of silica leaching from the BIF by warm, highly saline fluids (1st stage) and recrystallization of iron-rich phases to specular hematite and martite caused by moderately warm, low salinity, oxidized fluids (2nd stage) (Taylor *et al*., 2001). Studies conducted on hydrothermal-type deposits reveal a relatively restricted temperature range of ore formation for all deposits: these temperatures range from 150°C to 320°C (Taylor *et al*., 2001) during ore formation with the $\delta^{18}O$ of the hydrothermal fluid being estimated at approximately -2‰ relative to standard mean oceanic water (SMOW) (Beukes *et al*., 2003). It is thus suggested that the fluids involved are of shallow crustal origin (meteoric water) and have not interacted with any silicate rocks (Taylor *et al*., 2001; Beukes *et al*., 2003). The study conducted by Taylor *et al*. (2001) suggests that iron enrichment can be accounted for by simple silica leaching and an increase in porosity. Intrusive igneous rocks and shale units, present in most hydrothermal-type ore deposits, are believed to be important controls in the distribution of ore bodies.

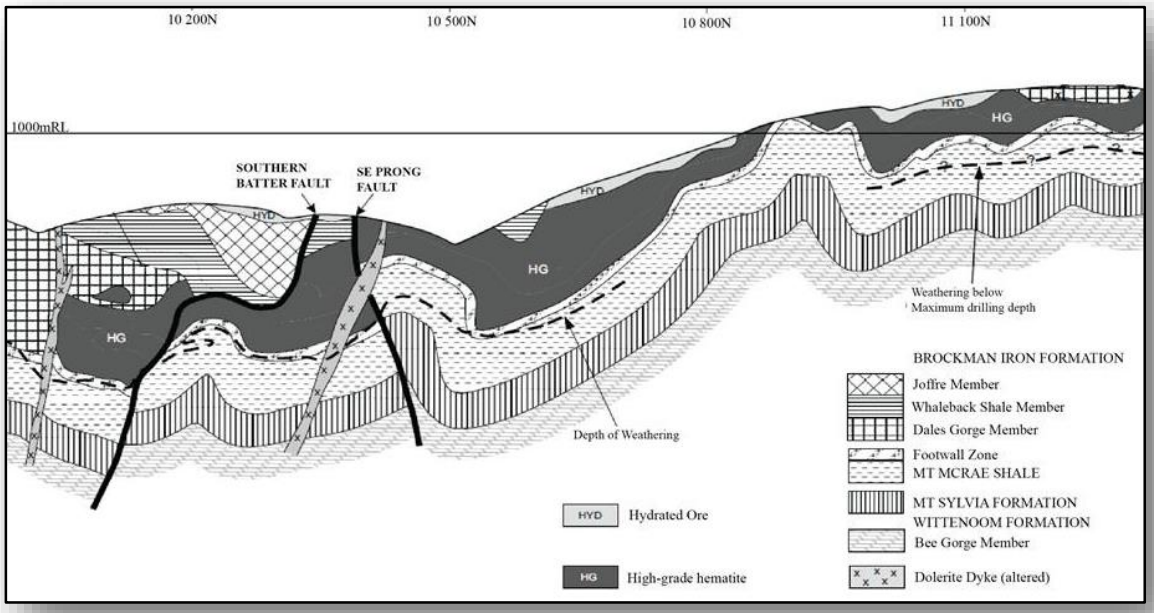

Figure 4: Schematic cross-section through the Mount Tom Price mine in the Hamersley Province of Australia, illustrating the main mineralisation horizons that parallel the prevailing trend of major fault zones (modified after Taylor *et al.*, 2001).

The modified magmatic-meteoric hydrothermal and supergene-modified hydrothermal type of iron-ores are encapsulated by the deposits from Brazil (Carajas district) and India (Noamundi district), respectively (Beukes *et al*., 2008; Figueiredo *et al*., 2008; Figueiredo *et al*., 2013). The Noamundi deposit is regarded as being of hydrothermal origin but have later experienced

deep chemical weathering in geologically recent times (Dalstra and Guedes, 2004; Gutzmer *et al*., 2008). The supergene overprint is believed to have contributed significantly to the further upgrading of the ore in terms of both tonnage and grade. The supergene-related ores are usually comprised of soft saprolitic ores which are the direct consequence of supergene enrichment. The hydrothermal-related hard laminated or massive hematite iron ores occur beneath the soft saprolitic-type ores in supergene-modified hydrothermal deposits (Dalstra and Guedes, 2004). The modified magmatic-meteoric hydrothermal fluid model for the Carajas hard hematite ores was suggested by Figueiredo *et al*. (2013), whereby a saline, ascending modified magmatic fluid caused oxidation of magnetite to hematite. The authors then suggest that this was followed by influx of meteoric water and mixing with ascending magmatic fluids, with the later stages of alteration being dominated by low-salinity meteoric-sourced fluids which maintained temperatures of 240° to 310°C forming late-stage tabular hematite.

1.5 Regional Geology of the Transvaal Supergroup

The Paleoproterozoic Transvaal Supergroup in the Northern Cape Province of South Africa was deposited between 2.65 to 2.05 Ga and its rocks cover an area of approximately 250 000 km^2 (Figure 5; Button, 1976; Moore *et al.*, 2001; Tsikos *et al*., 2003; Beukes & Gutzmer, 2008). The Transvaal Supergroup in this area consist of two major Groups, namely the **Ghaap** Group and the **Postmasburg** Group (Figure 6).

The **Ghaap** Group is composed from base to top of the *Schmidtsdrift*, *Campbellrand*, *Asbestos Hills* and *Koegas* Subgroups (Fig. 6). The lowermost (and therefore older) Schmidsdrift Subgroup comprises fluvial, shallow marine and intertidal arenites and lesser carbonate sediments (Beukes, 1986). The conformably overlying Campbellrand Subgroup represents a succession between 1500 and 1700m in thickness of carbonate rock (Beukes, 1987). Beukes (1987), subdivided the Campbellrand Subgroup into two major facies, namely the Ghaap Plateau facies and Prieska facies.

The Ghaap Plateau facies, which characterises the larger part of the Transvaal Supergroup in the Northern Cape, consists of eight formations, namely the basal Monteville followed by the Reivilo, Fairfield, Klipfonteinheuwel, Papkuil, Kogelbeen and the uppermost Gamohaam Formations (Errickson and Altermann, 1998; Altermann and Siegfried, 1997). The Monteville Formation is dolomitic and oolite-rich, whilst the overlying Reivilo Formation consists of

shallow-water stromatolitic carbonates which extend laterally into deeper-water, laminated carbonates (Altermann and Siegfried, 1997). The Reivilo and overlying Fairfield Formation are marked by the development of a distinct marker zone of the so-called *Kamden Member*. This marker consists of laminated carbonate overlain by banded iron formation (BIF) in the southern Ghaap Plateau facies (Beukes, 1987). The BIF continues towards the north, ultimately giving way to ferruginous dolomite and chert (Beukes, 1987). The Fairfield Formation generally consists of chert-pebble conglomerates and dolomitic breccia (Altermann and Siegfried, 1997).

Dolomitic breccia forms the base of the Klipfonteinheuwel Formation, which consists of chert beds and silicified stromatolitic dolomite (Altermann and Siedfried, 1997). Stromatolitic dolomites and limestones also form the largest part of the Papkuil Formation (Beukes, 1987). The overlying Klippan Formation consists of predominantly stromatolitic and microbial laminated dolomite at the base, with void-filling quartz in places. At the top of the Klippan Formation, dolomite and chert breccia in a shale matrix become predominant (Altermann and Siegfried, 1997).

The upper part of the Ghaap plateau Facies is made up of the Kogelbeen and Gamohaan Formations (Beukes, 1987). The Koegelbeen Formation consists of dolomite, limestone and some chert. The overlying Gamohaan Formation is dominated by stromatolititc mats and laminated carbonates (Altermann and Siegfried, 1997). Towards the stratigraphic top, black shales and iron-rich cherts (Klein Naute and Tsineng Members respectively) develop and constitute a transitional zone between the dolomites of the Campbellrand Subgroup and the BIF of the Asbestos Hills Subgroup (Altermann and Siegfried, 1997).

The Asbestos Hills Subgroup comprises two stratigraphic Formations, namely the lower (older), microbanded *Kuruman* BIF and the upper (younger) predominantly clastic-textured *Griquatown* BIF (Beukes, 1983). The Kuruman BIF is made up of the Kliphuis, Groenwater and Riries Members. Chert mesobands alternating with ankerite-rich mesobands of the Kliphuis member form the base of the Kuruman BIF (Beukes, 1983). The overlying Groenwater Member consists of bands of siderite-magnetite rhythmite, magnetite-hematite rhythmite and stilpnomelane lutite (Beukes, 1983). The Riries member completes the Kuruman BIF Formation and is made up largely of siderite-greenalite rhythmite (Beukes, 1983). The Griquatown BIF conformably overlies the Kuruman BIF, and is subdivided into three stratigraphic Members upwards, namely Middlewater, Danielskuil and Pietersberg (Beukes,

1983). The lower Middlewater and Danielskuil members grade from siderite-hematite to siderite-greenalite mudstones with mud-clast conglomerates at the top (Beukes, 1983). These two members are overlain by shallow-water to lacustrine, greenalite-rich muds and siliclastics which complete the Griquatown Iron Formation (Beukes, 1983).

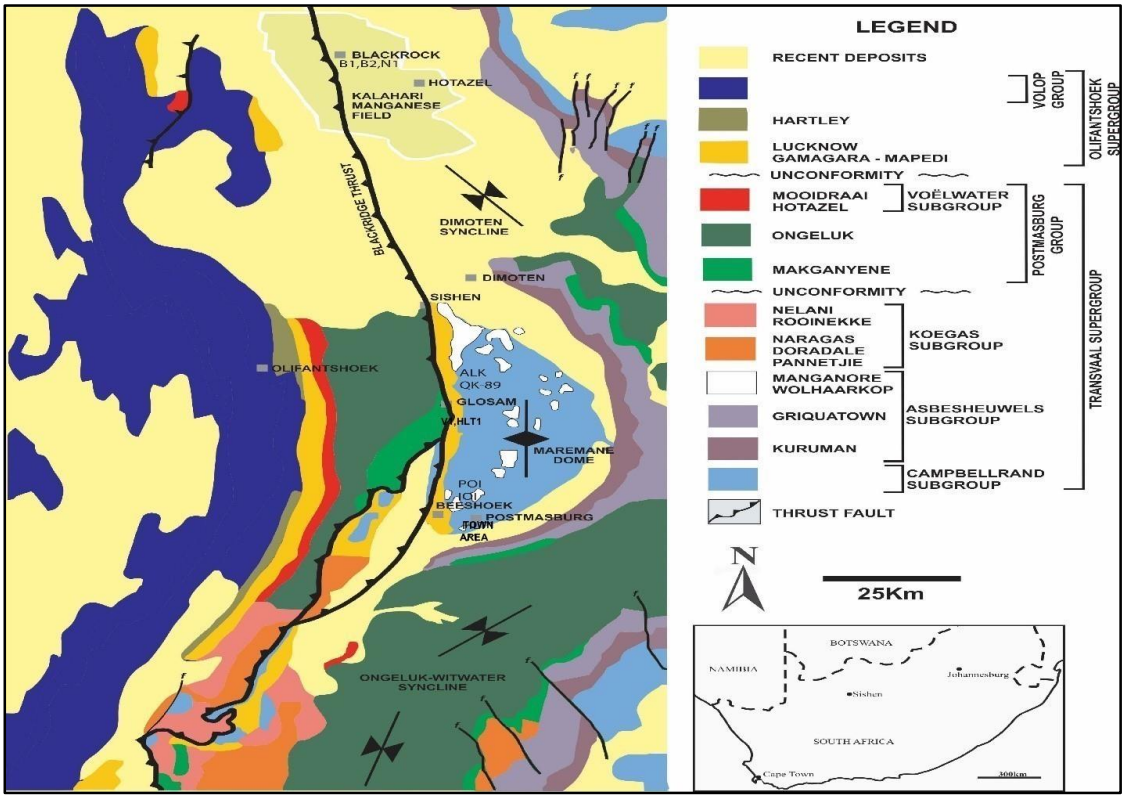

Figure 5: Regional geological map showing the distribution of the Transvaal Supergroup in the Northern Cape Province, widely also known as Griqualand West Supergroup. Localities of drillcores or individual samples used in this thesis, are also shown (modified courtesy of Assmang, 2005).

As mentioned earlier, the regional unconformity separating the Transvaal and Olifantshoek Supergroups (Fig. 2) results in dissolution collapse of BIF in areas where the unconformity contact truncates the contact between the Campbellrand Subgroup carbonates and overlying Kuruman BIF Formation. The BIF that is slumped into karstic sinkhole structures develops highly folded and brecciated occurrences that are often hard to link directly to a precursor part of the Kuruman BIF stratigraphy; this BIF has thus been variously termed in the literature as *Manganore Iron Formation* (Beukes, 1983; Alchin and Botha, 2006; Fig. 3). The *Wolhaarkop breccia* separating the Manganore BIF from the underlying Campbellrand carbonates (Fig. 3) develops in a residual fashion by dissolution of cherty, manganese-bearing Campbellrand

dolomite, thus causing residual build-up of insoluble material (mainly chert, manganese- and iron-oxides) making up the breccia matrix and clasts (Gutzmer and Beukes, 1996a).

The Koegas Subgroup conformably overlies the Asbestos Hills Subgroup but is only developed in the southern parts of the Northern Cape Province (Beukes, 1983; see Fig. 4). The subgroup consists of five formations (Pannetjie, Doradale, Kwakwas, Naragas and Rooinekke) which lithologically represent a cyclic siliciclastic succession intercalated with BIF and lesser black shale and carbonate (Beukes,1983; see also Figure 5). According to Beukes (1983), each siliciclastic-chemical sedimentary cycle represents a progradational sedimentary increment consisting of distal iron formation and proximal, ferruginous chloritic mudstones, siltstones and quartz wackes.

The Postmasburg Group overlies the Ghaap Group and is composed of the Makganyene, Ongeluk, Hotazel and Mooidraai Formations (Moore *et al.*, 2001; Tsikos *et al*., 2003). The Hotazel Formation represents the youngest BIF in the Transvaal Supergroup and contains three conspicuous Mn-rich layers. The volume and concentration of Mn metal in the Hotazel Formation renders it the largest continental deposit of manganese on Earth (Bekker *et al*., 2010).

The age range of the Postmasburg Group remains controversial: Beukes (1986) asserts that there was a period of uplift and erosion that led to the development of a regional unconformity between the upper Ghaap Group and the Makganyene diamictite Formation in the lowermost part of the Postmasburg Group. Such an interpretation conforms with the ~2.22Ga whole-rock model age of the Ongeluk volcanic sequence (Cornell *et al*., 1996) that overlies the Makganyene diamictites, but not with the ~2.39Ga of the Mooidraai carbonate Formation at the top of the Postmasburg Group (Bau *et al*., 1998; Fairey *et al*., 2013). Recent work by Polteau *et al*. (2006), and Moore *et al.* (2001, 2003, 2011) disputes the stratigraphic interpretation of Beukes (1986) and suggests instead that no unconformity exists between the Ghaap and Postmasburg Groups, thus lending support to more recent literature that challenges the 2.22Ga age of the Ongeluk Formation (Kampmann *et al*., 2015; Gumsley *et al*., 2017).

SUPER GROUP	GROUP	SUBGROUP	FORMATION	LITHOLOGY	APPROXIMATE THICKNESS (IN METRES)
TRANSVAAL	POSTMASBURG	VOELWATER	Mooidraai	Dolomite, Chert	250
			Hotazel	Mn, Fe-Formation	
			Ongeluk	Andesitic lava	900
			Makganyene	Diamictite	50-150
	GHAAP	KOEGAS	Nelani	Shale	240-600
			Rooinekke	Fe-formation	
			Naragas	Quartz-wacke, shale	
			Kwakwas	Riebeckitic shale	
			Doradale	Fe-formation	
			Pannetjie	Quartz-wacke, shale	
		ASBESTOS HILLS	Griquatown	Clastic textured Fe-formation	200-300
			Kuruman	Microbanded Fe-formation	150-750
		CAMPBELLRAND	Gamohaan	Sparry limestone, shale	1500-1700
			Kogelbeen	Dolomite, limestone	
			Klippan	Cherty dolomite	
			Papkuil	Dolomite	
			Klipfonteinheuwel	Cherty dolomite	
			Fairfield	Sparry dolomite	
			Reivelo	Micritic dolomite	
			Monteville	Dolomite, limestone, shale	
		SCHMIDTSTDRIF	Lokammona	Shale	10-250
			Boomplaas	Dolomite, limestone, shale	
			Vryburg	Quartzite, lave, shale	

Figure 6: Simplified stratigraphic column of the Palaeoproterozoic Transvaal Supergroup (after Beukes, 1986; Dorland, 1999; Tsikos and Moore, 1997).

1.6 Thesis outline and objectives

This study focusses on providing insights into the diversity of processes that are likely to have been involved during the genesis of high-grade iron ores from different localities across the Transvaal Supergroup, as it develops at the easternmost margin of the Northern Cape Province of South Africa. The intellectual stimuli behind this thesis combine the passion of the author to engage in fundamental geochemical research, with the need to make a

contribution to the knowledge of the genesis of the high-grade iron ores in the Transvaal Supergroup, which is a topic that remains controversial to date.

It should be noted that the present study does not constitute an attempt to provide full and conclusive resolution to the complex genetic history of the ores in question; rather, it is aimed at shedding further light into the geochemistry of these deposits on a regional scale, with emphasis on the geochemical relationships and controls exerted by the ferrous- versus non-ferrous (referred to also as "matrix" in this text) fractions of the ores from one locality to the next. The key objectives for this study can be summarized in the following four milestones:

1. To gain a better understanding of the geochemistry of the iron ores in question, by combining bulk with fraction-specific analytical methodologies;
2. To assess whether the fraction-specific analytical results provide any firm support for the origin of the ferrous and non-ferrous fractions of the ores, namely whether they represent any combinations of protolith residue, alloctonous detritus or hydrothermally-derived material, and whether the results are comparable and consistent (or not) across all samples studied;
3. To constrain, where possible, whether the iron ores are related primarily to a BIF protolith or potentially other protoliths too (i.e. shale), depending on the exact process of iron enrichment; and ultimately,
4. To provide constraints where possible as to whether the iron ores are predominantly hydrothermal, paleo-supergene, or have a mixed origin.

The four key objectives summarized in the foregoing lines will be achieved through assessing the chemical signatures and in some cases stratigraphic variations of the sampled ores. Representative ore material was obtained exclusively from drillcores that were drilled at four different localities of the Transvaal Supergroup in the Northern Cape, namely Hotazel, Beeshoek, King/Khumani and Heuninkranz. As also indicated earlier, bulk-rock analyses (XRF, ICP-MS) as well analytical applications (ICP-OES, ICP-MS) on partial extracts of the ores have been applied. The ICP-OES measurements were carried out by the author at the Department of Chemistry, Rhodes University, whereas the other measurements themselves were conducted at the Universities of Cape Town and Stellenbosch.

There are 5 chapters that form the main body of this thesis. The first chapter presents introductory aspects of the research such as general information regarding iron as a commodity, BIF-hosted high-grade iron ore deposits, regional geology of the Transvaal Supergroup, a

review of current literature as well as a summary of the objectives of the thesis and methodologies that were employed. The second chapter of the thesis presents the whole-rock geochemistry of the iron ores, where major and a wide array of trace element compositions excluding rare-earth elements (REE) are presented and evaluated. The third chapter presents a comprehensive account of the fraction-specific approach employed in this study. The chapter reviews the analytical protocols that have been routinely employed in previous studies for the dissolution of iron ores, and proceeds with the optimisation of the protocol for this study and its application. The results and some implications of the analytical protocol are also presented in this chapter. The fourth chapter presents exclusively bulk and fraction-specific REE results, on the basis of the prior extensive use of REE as a tracer of provenance and hydrothermal signature of iron ores. Finally, the fifth chapter provides a comprehensive discussion of the results presented in the foregoing chapters. Here, emphasis is placed on providing suggestions with regards to the pre-ore lithologies and the type of fluids that are potentially involved in the generation of these deposits, and highlights new specific geochemical signatures of direct interest to ore-forming processes. The discussion chapter concludes with a series of broad, all-encompassing conclusions and remarks derived from this research as well as some suggestions for future follow-up research.

1.7 Sample selection, processing, and methodological overview

A total of 29 samples of massive hematite iron ores were used for the geochemical analyses presented and evaluated in this thesis. The samples were collected exclusively from borehole core material which was diamond-drilled by the mining sector, and represent four different geographical areas in the Northern Cape containing different types of iron ore (see Fig. 5). These include:

- 18 samples of massive and micro-breccia style iron-ore from King/Khumani Farms, as currently being exploited by ASSMANG Ltd south of the town of Kathu in the Northern Cape Province and intersected in drillcores ALK (8 samples); QK (7 samples) and WK (3 samples);
- 6 samples of micro-breccia style iron-ore from the Beeshoek mining area, also operated by ASSMANG Ltd, as captured in drillcores PO (3 samples) and IO (3 samples);
- 3 samples of massive to crudely laminated/contorted iron-ore from two drillcores that intersect the uppermost highly ferruginised Hotazel BIF in the Black Rock Mn Mine area of ASSMANG Ltd (samples B1, B2 and N1); and,

- 2 samples of massive to laminated iron ore from corresponding prospecting drillcores obtained by KUMBA IRON ORE at locality Heuninkranz approximately 20km NW of the town of Postmasburg (V1, HLT1).

Sample selection was carefully carried out by avoiding any visible secondary veining that may affect geochemical homogeneity. Representative visual material of the iron ore samples as obtained during field logging, sampling and sample processing, are more comprehensively illustrated in the Appendix A.

All samples collected represented quartered-core intersections of a length not exceeding 5cm at the most. Once in the lab, they were thoroughly rinsed with deionised water, prior to them being crushed using a chromium steel ring-mill at the Geology Department of Rhodes University. The mill was cleaned through crushing fragments of pure quartz in between each ore-sample. The ore powders were subsequently stored in clean glass vials and labelled accordingly, and placed in a dessicator prior to further processing and analysis.

The sample powders were analysed using bulk-rock techniques (XRF, ICP-MS) as well as wet chemical analyses of fraction-specific aliquots of the original samples (ICP-MS, ICP-OES). Details on the analytical protocols employed in each stage of this geochemical study will be presented at the beginning of each of the respective chapters that follow. Below follows an overview of the three main instrumental analytical techniques employed in this work.

1.8 Overview of analytical techniques used in this thesis

1.8.1 X-ray Fluorescence (XRF)

An X-ray fluorescence (XRF) spectrometer is an x-ray instrument used for routine, relatively non-destructive chemical analyses of rocks, minerals, sediments and fluids (Beckhoff *et al*., 2006). It works on wavelength-dispersive spectroscopic principles that are similar to an electron microprobe (EPMA) (Rollinson, 1993). However, an XRF cannot generally make analyses at the small spot sizes typical of EPMA work (2-5 microns), so it is typically used for bulk analyses of larger fractions of geological materials (Beckhoff *et al*., 2006). The relative ease and low cost of sample preparation, and the stability and ease of use of X-ray spectrometers make this one of the most widely used methods for analysis of major and trace elements in rocks, minerals, sediments and soils alike (Jenkins and De Vries, 1973). The analysis of major and trace elements in geological materials by XRF is made possible by the

behaviour of atoms when they interact with x-ray radiation (Jenkins and De Vries, 1973). An XRF spectrometer works because if a sample is illuminated by an intense X-ray beam, known as the *incident* beam, some of the energy is scattered, but some is also absorbed within the sample in a manner that depends on its chemistry. The incident X-ray beam is typically produced from an Rh target, although W, Mo, Cr and other sources can also be used, depending on the application (Buhrke *et al*., 1998).

The applications of XRF include investigations that involve bulk chemical analyses of major elements (Si, Ti, Al, Fe, Mn, Mg, Ca, Na, K, P) in rocks and sediments (Beckhoff *et al*., 2006). Bulk chemical analyses of trace elements (in abundances >1 ppm; Ba, Ce, Co, Cr, Cu, Ga, La, Nb, Ni, Rb, Sc, Sr, Rh, U, V, Y, Zr, Zn) in rocks and sediments are also routinely analysed (Beckhoff *et al*., 2006). The detection limit of XRF is in the order of parts per million, or ppm (Jenkins and De Vries, 1973). In theory, the XRF has the ability to detect X-ray emission from virtually all elements, depending on the wavelength and intensity of incident x-rays. However, in practice, most commercially available instruments are very limited in their ability to precisely and accurately measure the abundances of elements with Z<11 in most natural earth materials (Buhrke *et al.*, 1998). XRF analyses cannot distinguish variations among isotopes of an element or ions of the same element in different valence states, so these analyses of rocks and minerals are done with techniques such as wet chemical analysis.

1.8.2 Inductively coupled plasma-optical emission spectrometry (ICP-OES)

ICP-OES (Inductively coupled plasma – optical emission spectrometry) is a technique in which the composition of elements in (mostly water-dissolved) samples can be determined using plasma and a spectrometer (Mermet, 2005). The technique has been commercially available since 1974 and thanks to its reliability, multi-element options and high throughput, it has become a widely applied one in both routine research as well as more specific types of analytical purposes (Hieftje, 1982). The solution to be analysed is conducted by a peristaltic pump though a nebulizer into a spray chamber (Hieftje, 1982). The produced aerosol is led into an argon plasma. Plasma is the fourth state of material, next to the solid, liquid and gaseous state. In the ICP-OES, the plasma is generated at the end of a quartz torch by a water-cooled induction coil through which a high frequency alternate current flows (Mermet, 2005). As a consequence, an alternate magnetic field is induced which accelerates electrons into a circular trajectory. Due to collision between the argon atom and the electrons ionisation occurs, giving

rise to a stable plasma. The plasma is extremely hot, at 6000-7000 K (Mermet, 2005); in the induction zone it can even reach 10000 K. In the torch, desolvation, atomisation and ionisation of the sample takes place (Hiefjie,1982). Due to the thermic energy taken up by the electrons, they reach a higher "excited" state (Mermet, 2005). When the electrons drop back to ground-level, energy is liberated as light (photons). Each element has an own characteristic emission spectrum. By means of an Echelle grating, a prism, and a focussing mirror, these emitted photon in various frequencies are captured simultaneously on a CCD chip (Charged Coupled Device) (Mermet, 2005). ICP-OES is suitable for the trace analysis of metal elements (0.0002-1000ppm) and a limited number of non-metallic elements (e.g. S, P) (Hieftjie, 1982). The OES instrument can measure the relative amounts of up to 60 elements per single sample run in less than one minute (Mermet, 2005; Figure 5).

1.8.3 Inductively coupled plasma-Mass spectrometry (ICP-MS)

ICP-MS (inductively coupled plasma-mass-spectrometry) is a technique to determine low-concentrations (range: ppb = parts per billion = µg/l) and ultra-low-concentrations of elements (range: ppt = parts per trillion = ng/l) (Yip and Sham, 2007). Atomic elements are led through a plasma source where they become ionized. Then, these ions are sorted on account of their mass. The advantages of the ICP-MS technique above AAS (Atomic Absorption Spectroscopy) or ICP-OES are its extremely low detection limit, a large linear range and possibilities to detect isotope composition of elements (Baranov and Tanner, 1999). The ICP-MS technique has a multi-element character and a high sample throughput, like ICP-OES, but it allows one to perform more sensitive measurements (Greenfield, 1994). Disadvantages and weaknesses of the ICP-MS detection are the occurrence of spectral and non-spectral interferences and the high costs. The sample introduction of ICP-MS is similar to ICP-OES. The sample solution is introduced into the device by means of a peristaltic pump. There, it becomes nebulized in a spray chamber (Greenfield, 1994). The resulting aerosol is injected into an argon-plasma that has a temperature of 6000-8000 K (Baranov and Tanner, 1999). Inside the plasma torch, solution is removed from the sample and also atomisation and ionization occur (Yip and Sham, 2007). Only a small amount part of the ions produced in the plasma further penetrate to the mass-spectrometer part (Greenfield, 1999).

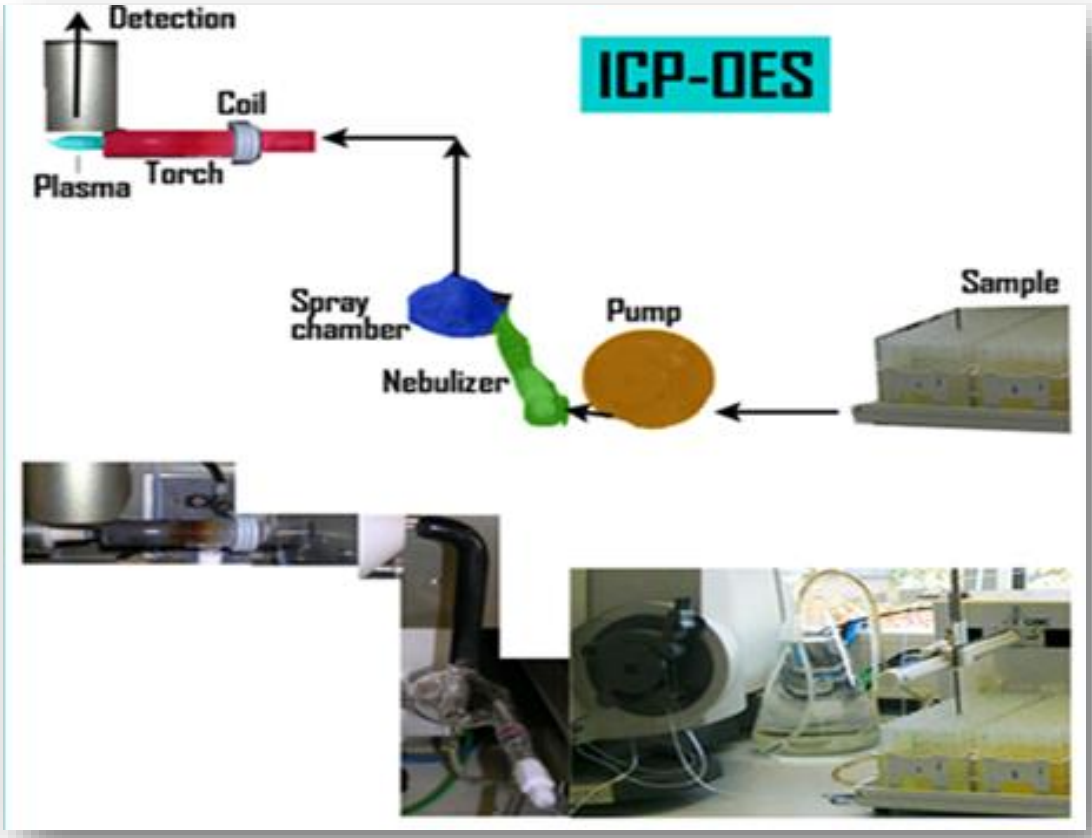

Figure 7: Schematic diagram showing the principles of ICP-OES

2 Whole-rock geochemistry

2.1 Introduction

Traditional whole-rock geochemical data for high-grade iron ore deposits are relatively scant throughout the published literature, revealing the remarkably little use of whole-rock geochemical techniques in attempts to quantify the transformation process of iron-rich sedimentary rocks to high-grade iron ore (Gutzmer *et al*., 2008). Researchers have focussed much of their attention instead on petrographic and specialised geochemical techniques, such as rare earth element (REE) and stable isotopes, with little focus on the importance of whole-rock geochemistry (Gutzmer *et al*., 2008). A key factor for this can perhaps be attributed to the largely monomineralic nature of these ores through the overwhelming abundance of hematite, which naturally obscures the significance that other elements in much lower concentrations may have on the overall geochemistry of the ore and on the understanding of their origin and distribution.

It is possible, that accurate high quality whole-rock geochemistry could aid in elucidating processes involved in the formation of these world-class iron ore deposits and particularly of the ores that form the subject of this study. It has been proposed that the South African iron ore deposits associated with BIFs of the Transvaal Supergroup are largely ancient supergene in origin (Beukes *et al*., 2003); they therefore contrast with most other iron ores of similar association worldwide. The application of whole-rock geochemistry may yet hold the key in furthering our understanding of the genesis of the South African ores, and understandably forms one of the core parts of this thesis.

In this chapter, major and trace element data of the samples collected from the four localities are presented and evaluated. Initially, the data are presented in the form of binary diagrams illustrating basic inter-elemental relationships, and are assessed in the context of standard mineralogical controls that they may reveal. Thereafter, comparative spidergrams involving data normalisation against average shale and BIF are used, in order to draw connections with likely protoliths and provide a benchmark for the evaluation of the fraction-specific and REE results which will be presented later in the thesis.

2.2 Sample collection and analytical techniques

Details with regard to sample collection, preparation, bulk analytical techniques and raw analytical results are already available in Chapter 1 and Appendices A and B. All 29 samples collected for this study were analysed for both major and trace elements. These include samples from locality King/Khumani as derived from boreholes ALK (8 samples; hereafter grouped as "A"), QK-89 (7 samples grouped as "Q"), and WK (3 samples, grouped as "W"); Beeshoek mine and environs, which includes boreholes PO and IO (3 samples each; all grouped as "B"); Hotazel Formation at Black Rock mine (samples B1, B2 and N1; grouped as "H"); and two ore samples from one exploration drillcore obtained at locality Heuninkranz approximately 20km NW of Postmasburg (samples V1 and HLT1, both grouped as "D"). Sampling across selected drillcore intersections of iron ore was carried out at a moderate stratigraphic resolution where possible (i.e. boreholes ALK & QK-89), in order to capture potential stratigraphic trends in bulk geochemistry. In all cases, sample selection was done taking extra care in avoiding secondary veining that may affect sample homogeneity.

Whole-rock analytical data for major element oxides were obtained via x-ray fluorescence spectroscopy (XRF) at the Department of Geology, University of Stellenbosch on sample powders fused into lanthanum-bearing, lithium borate glass discs. The latter were also used for trace element determinations by LA-ICP-MS, also at Stellenbosch University. Details of the analytical protocols used are included in the Appendix A.

2.3 Major and trace elements- results

2.3.1 Binary plots of major and trace elements versus Al_2O_3

The variation of bulk composition of terrigenous clastic sediments and sedimentary rocks are controlled by changes in the chemical composition of the source material. The geochemical composition of sedimentary rocks therefore provides important information about their origin (Calvert and Pedersen, 1993). In the case of the samples for this study, the origin of the material making up the iron ores is still not fully understood; prevailing ancient supergene models would predict enrichment of iron at the expense of a BIF, largely through residual processes. Simultaneous strong depletion in other elements that would have been present in the initial protolith, such as Si, would also be typical. However, as the influence of later fluids in the origin of the ores is also likely, the bulk geochemistry of the ores may be used to also

demonstrate a variety of other interconnected processes and effects beyond weathering, and perhaps help in understanding the relative influence of each process.

Aluminium has been used by many researchers as indicator of terrigenous clay detritus in sedimentary rocks, as it is mainly derived from weathering and is generally immobile during diagenesis, weathering and metamorphism (Somayajulu *et al*., 1994). It is therefore a conservative element that was chosen here to illustrate simple binary relationships with every other major and trace element measured, and help assess relative mobility behaviour. In principle, good statistically positive relationships of an element with Al would indicate a connection with an assemblage of minerals of common detrital origin; no relationship would possibly indicate a different source or process involved.

Major element oxides are plotted against whole-rock Al_2O_3 in Figure 8. The range of Al_2O_3 values of our samples is from 0.2 to just below 8wt%, which implies that some of the high Al samples selected for this study do not strictly fall under the term "iron-ore". A similar range of concentrations is seen for bulk SiO_2 as well. Most Al-rich samples come from the A-group of locality King/Khumani, and are also K-enriched (K_2O: 0.9-1.6wt%). Among all major elements plotted against Al-oxide, it is in fact the oxides K_2O, SiO_2 and to a lesser extent TiO_2 that show good positively correlations and therefore support a common detrital origin. Whereas K is expected to be present as fine-grained mica (sericite/muscovite), Si will occur as free quartz besides the amount corresponding to the structure of sericite and other detrital minerals. With regard to titanium oxide, abundances are always <0.3wt% and could be present in the ores in the form of particulate ilmenite ($FeTiO_3$), sphene ($CaTiSiO_5$) and/or TiO_2 polymorphs such as rutile.

Lack of any statistically significant correlation between other major oxides with Al_2O_3 suggests that other additional factors may have contributed to their distribution. Low P_2O_5 is probably a result of variable apatite content, and this would also account for most – if not all – of the bulk CaO. Only samples with wt%-level Ca are the Mn-enriched samples of group "H" from Hotazel, and sample W2 from King/Khumani, where much of the Mn may be present in carbonate minerals. Finally, the high-Mn iron-ore samples of group H are a notable exception to the overall sample set, and probably owe their origin to Mn re-mobilisation and re-precipitation during fluid alteration of the manganiferous Hotazel Formation (Gutzmer & Beukes, 1996).

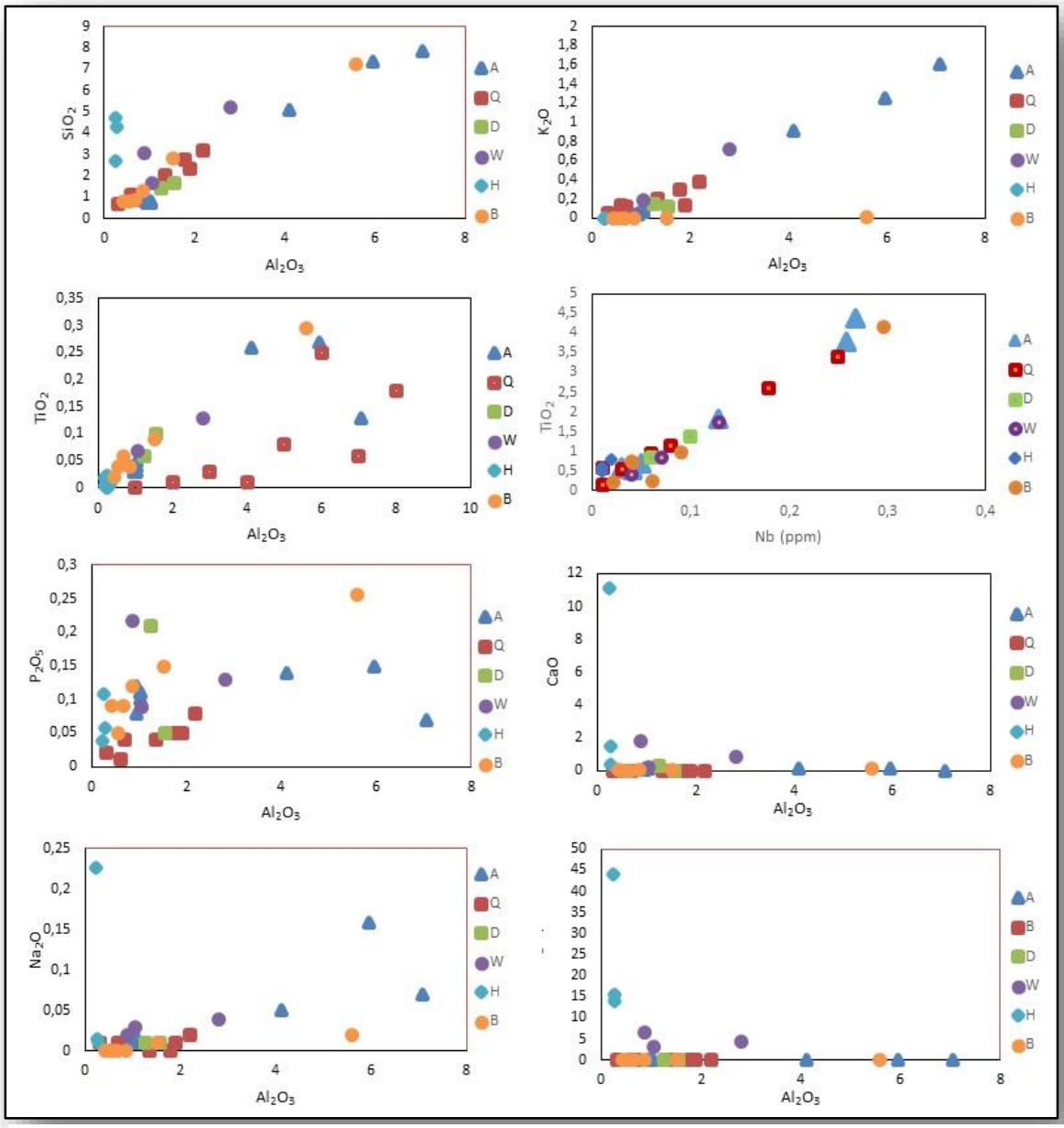

Figure 8: Bivariate plots of whole-rock major oxides versus Al_2O_3 and TiO_2 versus Nb. Major oxides are measured are measured in wt.% and Nb measured in ppm.

Trace element analyses of the selected samples show concentrations of barely above detection for Hf, Ta, Th and Pb; a few ppm on average for Sc, Co, Rb, Y, Nb, Mo and U; in the order of tens of ppm for V, Cr, Ni, Cu, Zn; and up to hundreds ppm for Ba and Sr. Exception to the above rule are basically the Mn-rich samples from Hotazel and King/Khumani, which show substantially larger values in elements such as Co, Ba and Pb, and less so for Zn and Ni. There is a notable correlation between Nb and Ti and this correlation may be indicating similar

relations but different siliciclastic materials (i.e we do observe detritus input but from different sources).

Binary plots of trace element concentrations against bulk Al_2O_3 are shown in Figure 9. Statistically good positive correlations for the greatest majority of samples are seen for Hf, Zr, Rb, Nb, and Sc and is indicative of a common detrital source for these elements (Figure 9). Zircon is the obvious expected detrital host for Zr and Hf, whereas High field strength elements (HFSE) such as Nb as well as Zr and Hf may also be hosted in detrital Ti-minerals such as rutile (Nagasawa 1970 and Belousova *et al*., 2002). The enrichment of transition metals such as V, Cr and less so Mo would be hosted also in Ti phases such as titanite, ilmenite and rutile

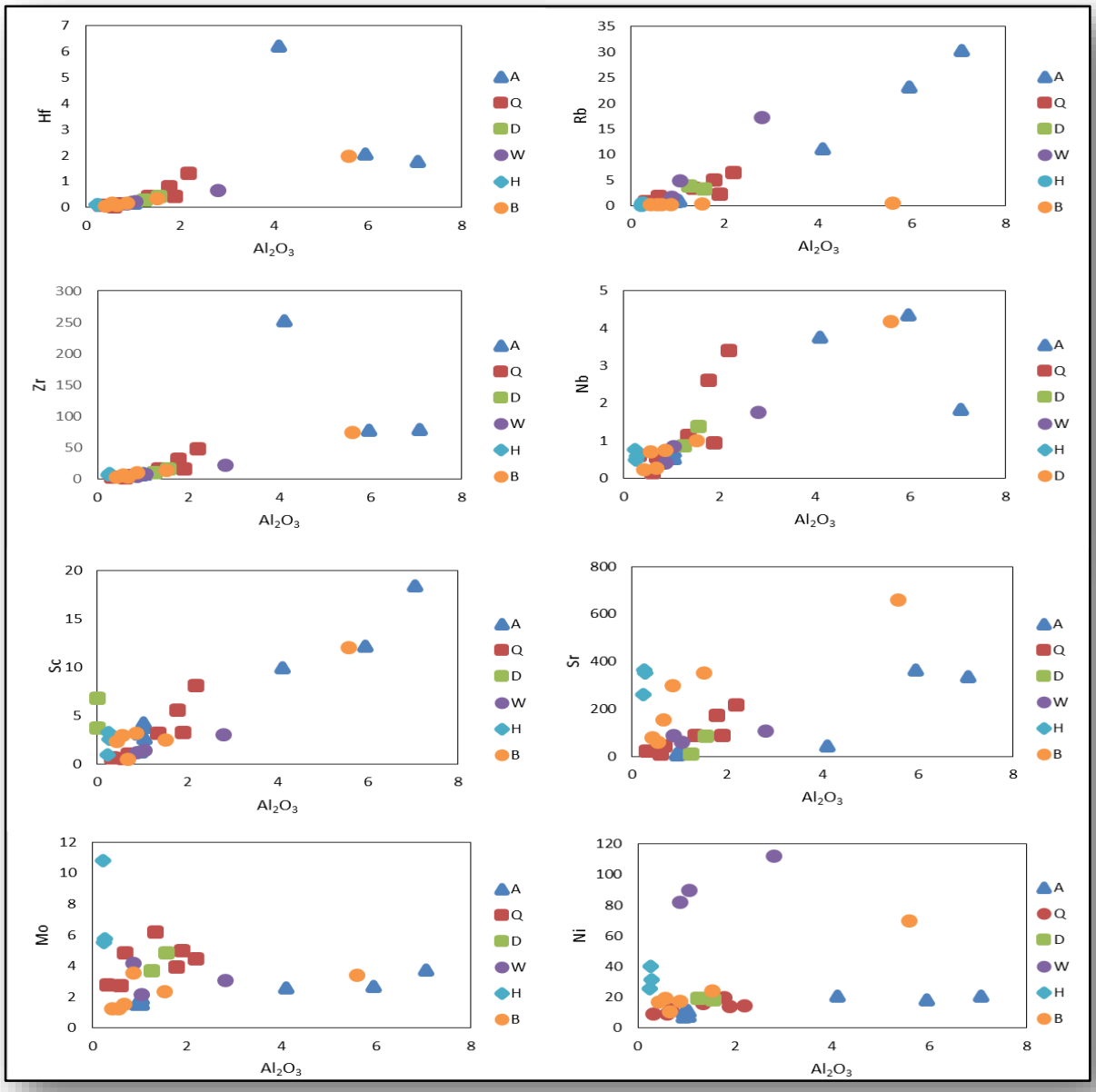

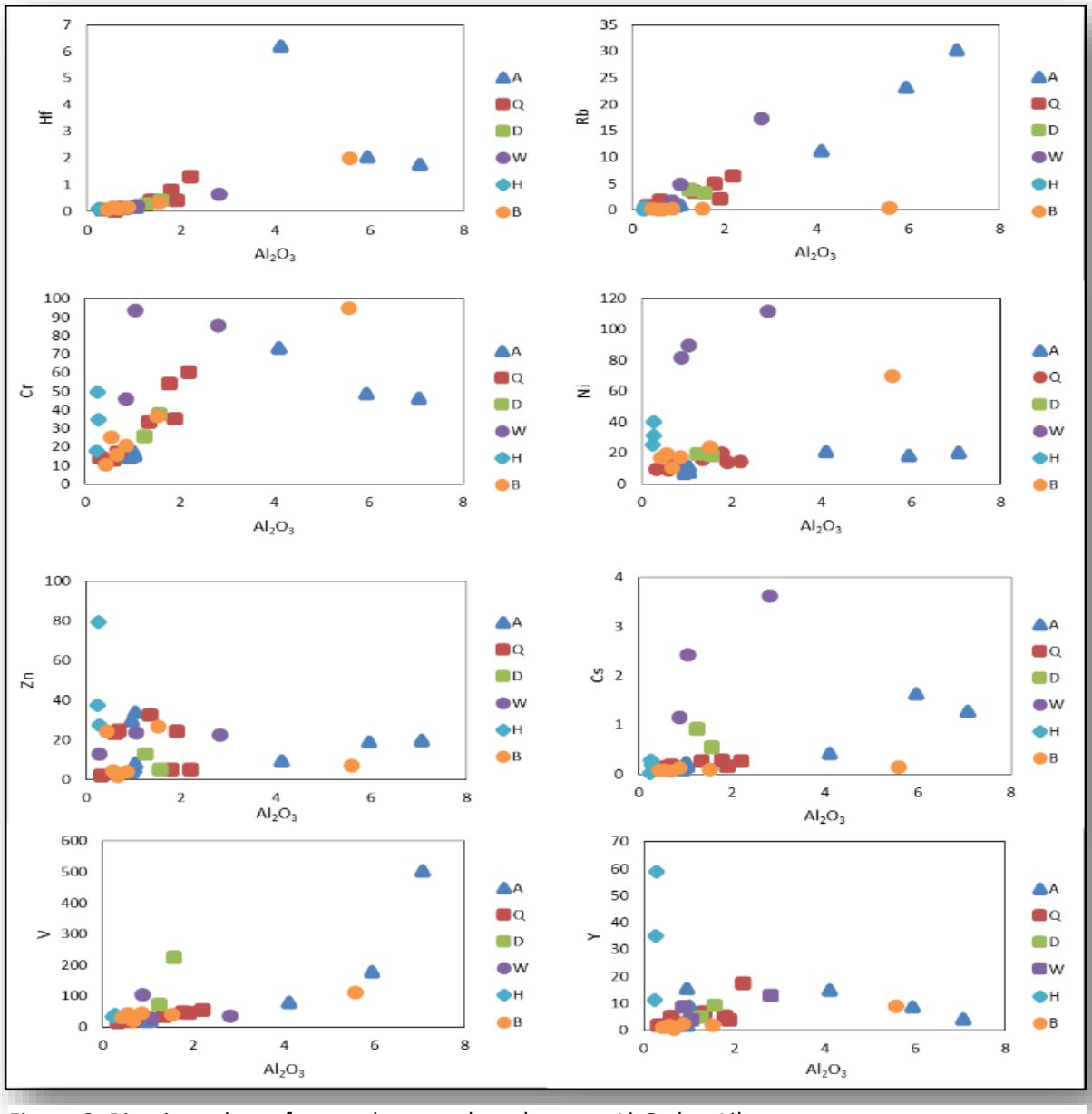

Figure 9: Bivariate plots of trace elements (ppm) versus Al_2O_3 (wt.%).

(Deer *et al*., 1992). Rb does not form any minerals on its own, but it is commonly present in several minerals substituting for potassium, mainly micas such as muscovite and to lesser extent in K-feldspar such as orthoclase (Deer *et al*., 1992).

2.3.2 Major element spidergrams

High-grade hematite ores are, by definition, anomalously enriched in iron oxide to concentrations as high as >99 wt.%. For that reason, they are chemically extreme rocks by comparison to a standard sedimentary rock such as BIF or shale. In order to constructively assess bulk-rock geochemical data from iron ores against geochemically more “normal” rocks

such as BIF or shale, it is important to eliminate the skewing factor that extremely high bulk iron-oxide concentrations exert on the other bulk geochemical data. Therefore, an assumption has been made in this thesis that the iron ores studied were formed by the addition of only iron to an original protolith such as BIF, or potentially even shale, while every other component in the rock behaved conservatively. In order to implement that assumption practically, enough iron was hypothetically "removed" from the analyses of each sample, so that by re-calculating the remaining data to a total of 100 wt.%, the Fe-oxide abundance for each sample would become the same as that of average BIF or shale. That way, the recalculated ratio of bulk Fe-oxide against that of average BIF or shale would be at a constant value of 1 for every sample, and therefore the relative concentrations of all other elements would be assessed against a "constant iron" basis for every sample. In classic spidergrams such as those that follow in the present section, that constant iron ratio would be manifested as a line parallel to the x-axis with origin the value of 1 on the Y-axis.

That above assumption clearly cannot be considered to be realistic with respect to the natural geological environment, as the behaviour and mobility of each element can be affected by a multitude of factors, particularly in rocks as old as the ones dealt with in this thesis. What it does, however, is to simplify and streamline comparisons with the presumed dominant protolith/s and also permit the extraction of some important first-order conclusions concerning the variations of the various elements against one another as well as those of the protolith, and the possible controls for these variations.

The average composition of BIF used here was compiled from unpublished data of the Kuruman BIF by Oonk (2017), whereas the Post Archean Australian Shales (PAAS) average composition was sourced from Taylor and McLennan (1985). Normalised data have been plotted on a logarithmic scale throughout as typically done in the literature, in order to facilitate the visual presentation of the normalised data in light of the very large variations in absolute values for each element and across different elements.

2.3.2.1 Major element spidergrams normalised relative to average Kuruman BIF

Figure 10 presents the results of BIF-normalisation of the iron ore re-calculated data on the basis of constant iron. There are essentially six class groups identified, namely three from the King/Khumani area (QK, ALK and WK), one from the Beeshoek area (Group "B", samples "P" and "I"), one from the Heuninkranz area (group "D", samples HLT1 and V1), and one

from the Hotazel area (group “H”. samples B1, B2 and N1). For simplification purposes, the QK, ALK and WK data from King/Khumani are simply referred to here as Q, A and W respectively.

In general, the “Q” and “A” sample groups from King/Khumani show a similar pattern of primary enrichment in TiO_2, K_2O, P_2O_5 and Al_2O_3, relative to Kuruman BIF. There is an enrichment factor for TiO_2 between 11 and 86, for Al_2O_3 between 53 and 92, for P_2O_5 between 4 and 60, and between 5 and 51 for K_2O. The same samples appear mostly depleted in MgO and CaO relative to average Kuruman BIF, with many of them showing values below detection. Normalised SiO_2 values plot very close to the constant Fe line, whereas bulk Mn-oxide is somewhat more erratic, with some values showing enrichments and some depletions by a factor of 2-3 relative to the constant Fe line. Minor enrichment of Na_2O up to a factor of 3 is also observed in samples with detectable Na (“A” group).

The two samples from the Heuninkranz area (HLT1, V1) appear to be directly comparable to those from the King/Khumani area in terms of their large enrichments in TiO_2, K_2O, P_2O_5 and Al_2O_3. The same applies to the Beeshoek samples (“P” and “I”) with the exception of K_2O which is very low to undetected at Beeshoek. Enrichment factors for the Beeshoek samples are 31 to 73 for TiO_2, 20-69 for P_2O_5, and 60-80 for Al_2O_3. SiO_2 again plots on or very close to the constant Fe line while Mn-oxide fluctuates erratically about the constant Fe line.

The “W” sample group from King/Khumani shares similarities with the other samples from King/Khumani and those from Beeshoek, at least with respect to the strong enrichment in Al_2O_3 and P_2O_5 relative to average Kuruman BIF. Moreover, a strong enrichment in Mn-oxide is present here too, and this is accompanied by enrichment in CaO. K_2O values are either enriched than or similar to average BIF, whereas SiO_2 and Na_2O can be depleted or enriched but both with values close to the constant Fe line. Finally, the Hotazel group of samples also show, as pointed out earlier, marked enrichment in bulk Mn-oxide. The SiO_2 and MgO oxides show apparent depletion relative to average Kuruman BIF, whereas all other oxides (CaO, Al_2O_3, P_2O_5, TiO_2 and Na_2O) are more erratic and plot close to the constant Fe line.

2.3.2.2 *Major element spidergrams normalised relative to PAAS*

In marked contrast to the BIF-normalised spidergrams of the previous section, the PAAS-normalised spidergrams show a much "tighter" data distribution around the constant Fe line(i.e more closer to the constant Fe line relative). Starting with the "Q" sample group from King/Khumani, these show marked relative enrichments only for Mn-oxide (factor between 2 and 30) and for P_2O_5 (factor between 3 and 13). Bulk Al_2O_3 plots close to the constant iron line with an enrichment factor not higher than 3. Normalised SiO_2 data plot just below the constant

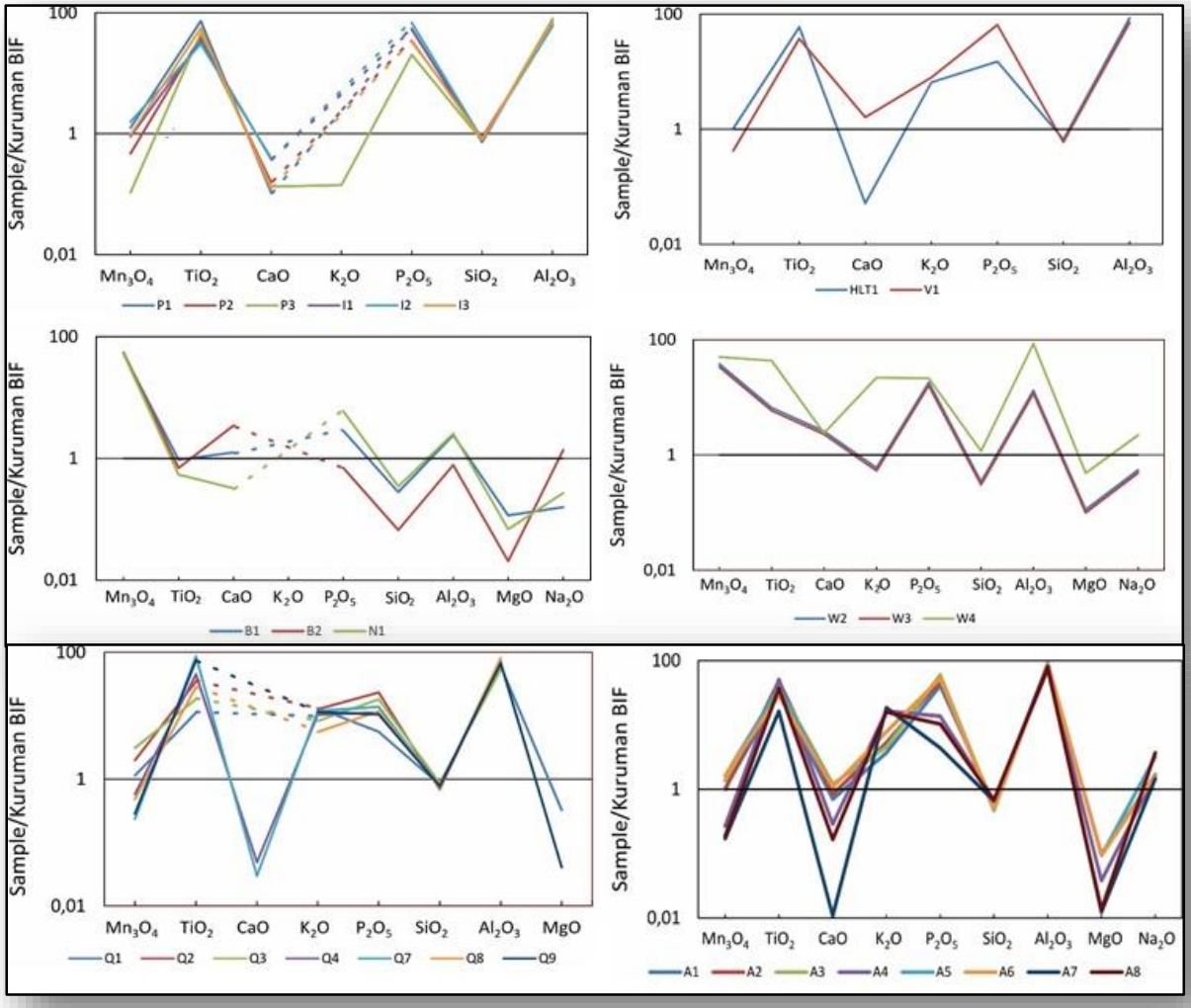

Figure 10: Kuruman-BIF normalized major elements (Kuruman BIF; Oonk, 2017, unpublished).

Fe line, whereas K_2O plots also just above or below the constant Fe line. TiO_2 values are more erratic with most samples plotting above the constant Fe line with an enrichment factor up to 5, though some samples also plot below it. The CaO and MgO measurements were below detection limit in most samples, but where they were measured, they show marginally lower values below the constant Fe line, relative to PAAS.

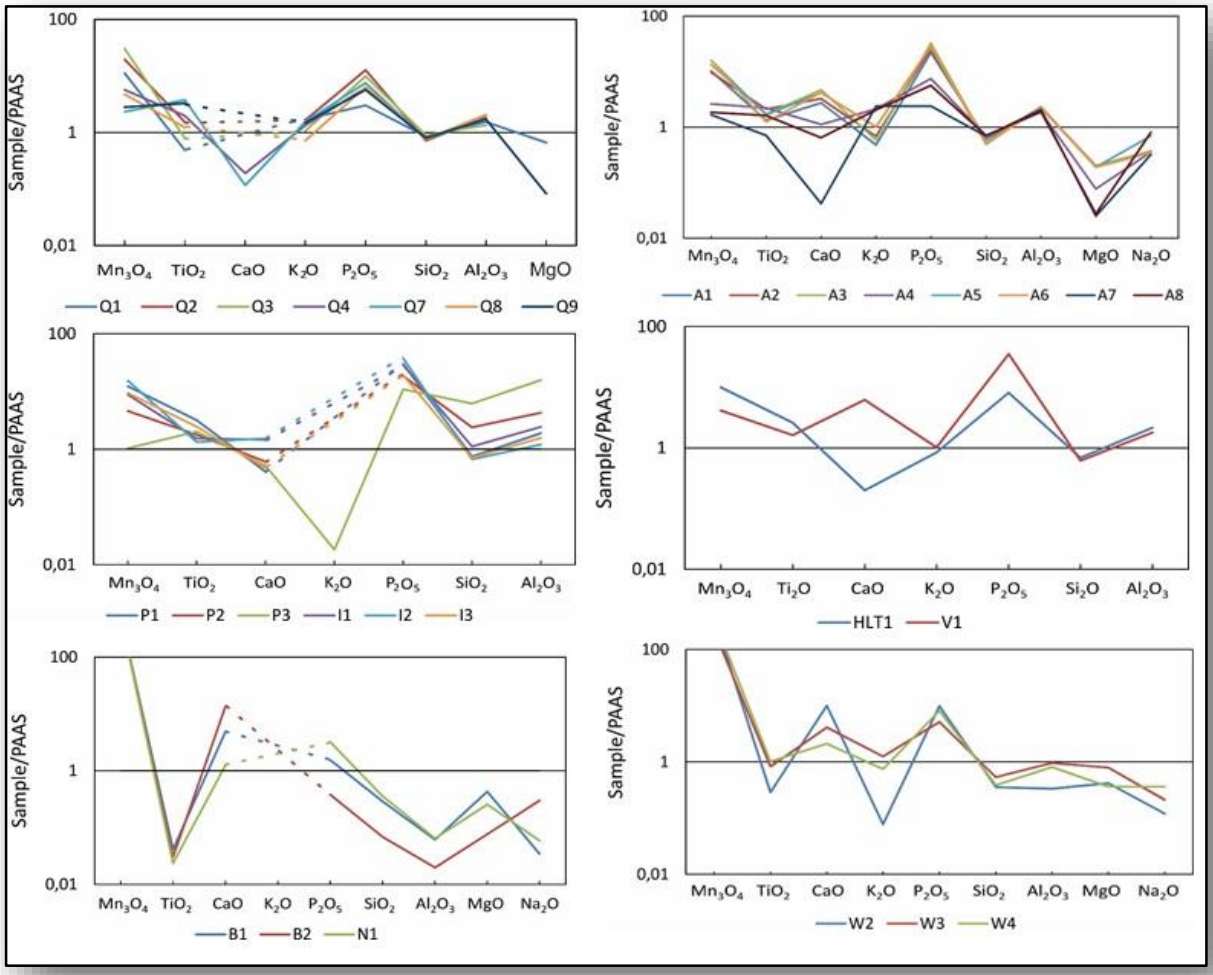

Figure 11: PAAS normalized major element spidergrams (PAAS data from Taylor and McLennan, 1985).

Sample group "A" from King/Khumani is very similar to that of the "Q" group. The enrichment factors for Mn-oxide is between 2 and 16 relative to PAAS, whereas for P_2O_5 lies between 2 and 33. Al_2O_3 values plot very close and slightly above the constant Fe line, whereas SiO_2 values also plot close to PAAS albeit slightly below. The TiO_2 values are also similar to that of the "Q" samples, where most of them plot close to the constant Fe line, with some above (enrichment factor up to 2) and some below. The CaO values show also rather erratic behaviour with some samples depleted and others enriched (by a factor of around 2) relative to the constant Fe line. K_2O shows similar behaviour as that of CaO with most values plotting just

below the constant Fe line, and a few above (enrichment factor up to 5). MgO plots variably below the constant Fe line, and the same applies to Na_2O though the latter is relatively less depleted by comparison to PAAS.

The sample class from the Heuninkranz area north of Postmasburg (samples V1 and HLT1) is essentially very similar to the "Q" and "A" classes from King/Khumani presented earlier. These two samples show enrichments in Mn-oxide and P_2O_5 relative to PAAS. By contrast, Al_2O_3 , SiO_2, K_2O and TiO_2 values plot very close to the constant Fe line, with Al_2O_3 appearing slightly enriched. CaO can either be enriched or depleted in these samples.

With regard to the samples from the Beeshoek area, again the Mn oxide values for these samples are either enriched or plot close to the PAAS signal, with a maximum enrichment factor of 15. P_2O_5 is also enriched with an enrichment factor up to the value of 37. There is also variable enrichment of Al_2O_3 with a factor between as low as 1 and as high as 16. The values of SiO_2 appear to show the same kind of variation with Al-oxide though at slightly smaller enrichment factor compared to PAAS. The TiO_2 values plot mostly close to the constant Fe line with enrichment factor not higher than 3. In contrast to the samples from King/Khumani, K_2O values here mostly are below the detection limit for most samples and very low by comparison to PAAS where measured. Likewise, Na_2O and MgO were below detection for all Beeshoek samples. Finally, CaO is quite variable and generally plots just above the constant Fe line (enrichment factor of up to 2).

The Mn-rich "W" sample group from King/Khumani shows the expected high degree of enrichment in Mn relative to PAAS, with enrichment factors that reach the value of 376. Most other oxides, namely TiO_2, Al_2O_3, K_2O, MgO and Na_2O, show values that fall either below or at the constant Fe line with only one K_2O value plotting above the constant Fe line. The only oxides that register values higher relative to PAAS are CaO and P_2O_5. The samples from the Hotazel area have an even higher Mn content than the "W" group, and therefore record a much larger enrichment relative to PAAS. P_2O_5 is relatively enriched as well but can also show values below the constant Fe line, but also show minor depletion. Similar to the "W" sample set, the oxides TiO_2, Al_2O_3, K_2O, MgO and Na_2O all plot below the constant Fe line, but show even greater relative depletions than the "W" samples do.

2.4 Trace element results normalised to BIF

Trace elements were recalculated at constant Fe, normalised against PAAS and BIF and plotted using the same procedure as with the major and minor element oxides. The trace elements are presented in spidergrams broadly separated mainly into HFSE on the left hand side of the x-axis, and predominantly transition metals on the right-hand side.

In the Kuruman BIF-normalised spidergrams (Figure 12), the samples were grouped according to their corresponding locality as previously. Although all patterns are distinctly "spiky" because of the relatively different behaviour between the individual elements, they form essentially flat patterns parallel to the x-axis. Furthermore, some distinct first-order characteristics that are common to all samples must be highlighted. Firstly, the data show significantly higher enrichments by comparison to average Kuruman BIF for all elements except for Rb and Cs, resulting in the spidergrams plotting well above the constant Fe line in almost all cases. The only samples that show relatively smaller trace element enrichment relative to BIF are the Mn-rich samples from Khumani ("W" group) and Hotazel ("H"group, samples B1, B2 and N1). In these samples, Rb and Cs plot either about the constant Fe line or below it.

In terms of specific trace element enrichments, there is a set of elements that shows consistent behaviour across all iron ore samples from King/Khumani, Beeshoek and Heuninkranz. These are specifically the elements Ba, Sr, U, Ni, V, and to a smaller and more variable extent the elements Pb, Sc and Mo. Zn and Cu appear to be much more erratic across different localities. Elements such as Ba and V can reach enrichment values as high as 100 times or more that of average Kuruman BIF. With regard to the HFSEs, these show smaller and more erratic enrichments relative to BIF, especially for Zr and Hf at locality King/Khumani, but still much higher than the constant Fe line.

The Mn-rich iron-ore samples from King/Khumani, as well as those from Hotazel, show some similarities but also some differences to the rest of the samples. One of the main characteristics is that the Ba abundances are extremely high relative to the average BIF, and suggest that Ba-rich minerals such as the barium sulphate mineral barite must be present in these samples. Along with the very high Ba, U and Sr also appear relatively enriched at both localities. Most transition metals show a general enrichment in both localities too, especially V, Ni, Co, and Pb. Most other trace elements show generally smaller enrichment relative to BIF as are

distinctly higher for all W samples, A3, A5, and A6 and for all Hotazel samples (B1, B2 and N1). Most of the remaining trace elements and HFSE, with the exception of Y perhaps, show values that are either very close or at the constant Fe line.

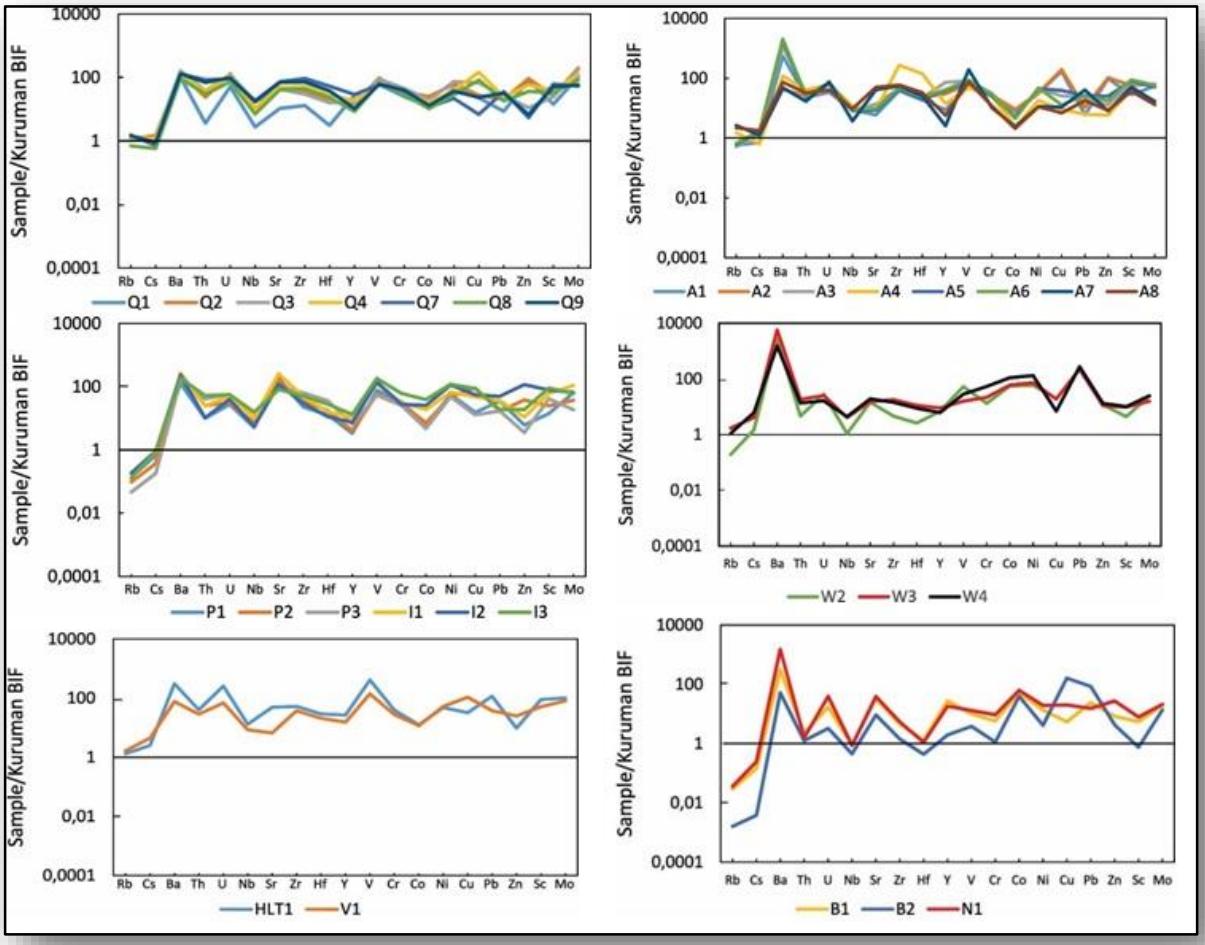

Figure 12: BIF-normalized trace element spidergrams (average BIF from Oonk, 2017, unpublished).

2.5 Trace element results normalised to PAAS

The same trace element compositions for the same localities normalised and presented against the average Kuruman BIF, are also presented normalised to PAAS in the form of spidergrams (Taylor and McLennan, 1985). In general, the PAAS-normalised trace elements plot a lot closer to, if not at the constant Fe line for almost all samples (Figure 13). The patterns remain spiky across the different samples due to the variable behaviour of the various elements. In general, the spidergrams have a gently positive slope from the HFSE side of the x-axis to the transition metal side. This slope looks distinctly steeper and more spikey for the Hotazel samples, and less steep and smoother for all other sample groups from Khumani/King, Beeshoek and

Heuninkranz. In general, therefore, the samples appear relatively more enriched in transition metals than they are in HFSEs, although the behaviour of each element may vary from one sample to the next.

There are similarities and differences in terms of relative behaviour of the normalised trace elements between the BIF-normalised and PAAS normalised plots. Firstly, the Ba spike that is seen in all BIF-normalised plots is now only present in a few samples of the "A" group from King/Khumani. Otherwise, norrnalised Ba values mostly plot very close to the constant Fe line. Exception to this is again the Mn-rich samples from both King/Khumani and Hotazel, where there is a distinct enrichment spike for Ba for all but few samples. The elements Sr and U

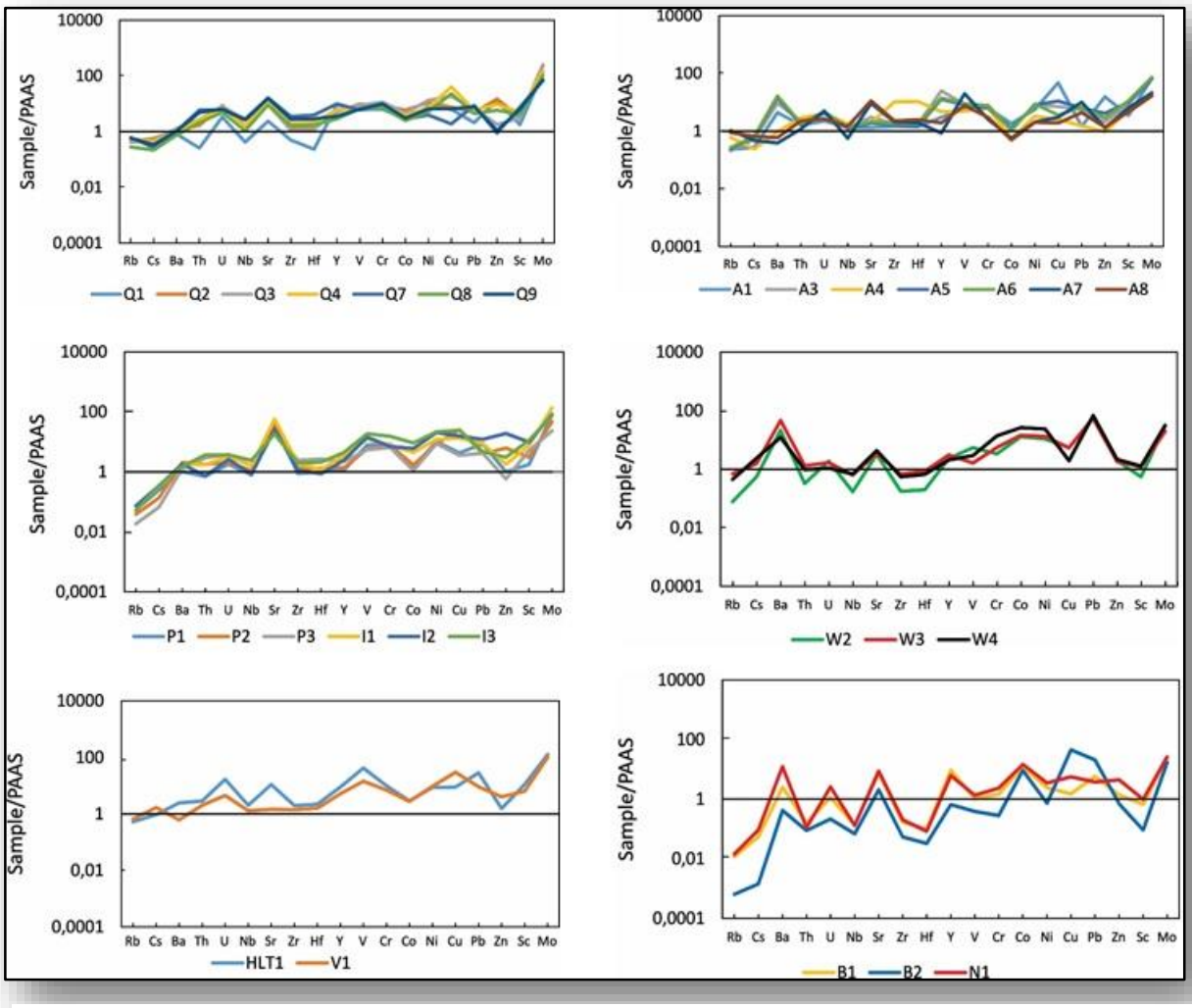

Figure 13: PAAS-normalized trace element Spidergrams (PAAS data from Taylor and Mclennan, 1985).

appear enriched relative to PAAS, as they do for BIF-normalised samples, except for the Beeshoek samples where U plots very close to the constant Fe line and Sr is most enriched. All other HFSE on the left hand-side of the x-axis, plot very close or on the constant Fe line, and

this applies to essentially all samples, except for the Hotazel ones where they plot below the constant Fe line.

As mentioned above, the transition metals show a general enrichment relative to PAAS and this applies mainly to the Mn-poor samples of iron ore from King/Khumani, Beeshoek and Heuninkranz and less so in the Mn-bearing samples of group "W" from King Khumani. The only elements that do not seem to agree with that pattern are Co, Zn and Sc, which show values that appear relatively depleted against PAAS. The same applies to the Mn-rich W samples with Pb being the most enriched trace element, whereas Cu here is also depleted relatively to PAAS. The element Mo appears to be the relatively most enriched by comparison to PAAS for most samples, with enrichment factors reaching up to the value of 100 or higher.

Finally, the Hotazel samples are the ones that show the spikier and steeper slope and they are also the ones where the spidergrams lie on average closer to the constant Fe line. The elements Ba, U, Sr, Y, Co, Cu, Pb and Mo appear relatively enriched in at least some of the samples, whereas Rb, Cs, the HFSE, Cr, V, Zn and Sc appear relatively depleted by comparison to PAAS, and plot mostly below the constant Fe line.

2.6 Summary of bulk geochemical signatures

Below is a summary of all salient bulk geochemical characteristics of the examined iron ore samples of this study as presented in this chapter:

- Among all major elements plotted against Al-oxide, it is the oxides of K, Si and to a lesser extent Ti that show good positively correlations and therefore support a common detrital origin. Most Al-rich samples come from locality King/Khumani, and these are also K-enriched (K_2O: 0.9-1.6wt%). For the greatest majority of samples, good positive correlations also exist between bulk Al_2O_3 and the trace element Hf, Zr, Rb, Nb, and Sc. These are likewise indicative of a common detrital source.
- Abundances of the elements Ba, Sr, Pb and Zn, particularly in Mn-rich samples from Hotazel and King/Khumani ("W" group) show lack of any meaningful statistical correlation with bulk Al-oxide and are thus thought to be potentially sourced from exotic sources (e.g. hydrothermal fluids).

- In BIF-nornalised major element plots, abundances of TiO_2, K_2O, P_2O_5 and Al_2O_3, appear much enriched for most samples. Partial exception to this with respect to their very low K_2O are the Beeshoek samples ("P" and "I" groups). Mn-rich samples also display strong enrichment in Al_2O_3 and P_2O_5 relative to average Kuruman BIF, and this is accompanied in most cases by an enrichment in CaO.
- BIF-normalised trace element spidergrams are distinctly "spiky" but show significantly higher enrichments by comparison to average Kuruman BIF for all elements except for Rb and Cs, resulting in the spidergrams plotting well above the constant Fe line in almost all cases. The only samples that show relatively smaller trace element enrichment relative to BIF are the Mn-rich samples from Khumani ("W" group) and Hotazel (samples B1, B2 and N1).
- In marked contrast to the BIF-normalised major element spidergrams, the PAAS-normalised spidergrams for most samples shows a much "tighter" data distribution about the constant Fe line. In terms of specific trace element enrichments, there is a set of elements that shows consistent behaviour across all iron ore samples from King/Khumani, Beeshoek and Heuninkranz. These are specifically the elements Ba, Sr, U, Ni, V, and to a smaller and more variable extent Pb, Sc and Mo. Zn and Cu appear to be much more erratic across different localities. Elements such as Ba and V can reach enrichment values as high as 100 times or more that of average Kuruman BIF.
- PAAS-normalised trace elements spidergrams plot very close to or at the constant Fe line for almost all samples. In general, a relative enrichment in transition metals is seen compared to HFSEs, although the behaviour of each element may vary from one sample to the next. Co, Zn and Sc have normalised values relatively depleted against PAAS, whereas Mo appears relatively enriched by comparison to PAAS.

3 Fraction-specific geochemistry

3.1 Review of iron oxide dissolution

This section describes first the work done on the dissolution of iron in order to appreciate how much progress has been done to date. The literature review details the mechanisms involved to better understand the steps involved during dissolution of iron. The experimental section optimises the best method that has been employed by other researchers for the dissolution of iron to achieve the objectives of this work.

Iron oxide dissolution plays an important role on an industrial field, especially in hydrometallurgy, the passivity of metals and cleaning of metal surfaces, in leaching iron oxide (Panias *et al*., 1996). There are several factors that affect the dissolution process of iron oxides. These include the temperature of the system, the properties of the solid phase (such as particle size distribution), the chemical composition and surface area, and the composition of the liquid phase, such as pH, redox potential and concentration of the solvent.

In this chapter, basic mechanisms surrounding the process of dissolution of iron oxides in organic acids are discussed. The chapter is broadly subdivided in two parts: in the first, a general literature overview is presented and emphasis is placed on the dissolution of the mineral hematite, as this is the solitary Fe-phase of the iron ores studied here. The second part of the chapter provides details on the application of fraction-specific geochemistry on the study samples, and includes a quality assessment of the protocol applied.

3.2 Mechanisms of dissolution

Stumm and Furrer (1987) carried out extensive work on the mechanisms of dissolution of metal oxides, whereas more recently, Cornell and Schwertmann (2003) further discuss the mechanisms and kinetics of dissolution of iron oxides. There are three distinct mechanisms involved during the dissolution of iron oxides as reported by Panias *et al*. (1996): (1) protonation (adsorption), (2) complexation, and (3) reduction. Protonation is a slow mechanism whereas reduction which takes place later in the process of dissolution is the fastest. Banwart *et al*., (1989) have suggested that these three mechanisms can in fact co-exist, and that ligand-promoted reductive dissolution, combining both complexation and reduction, would result in the most desired effect for the kinetics of dissolution. It is commonly known that the Fe atom

in iron oxide can act as Lewis acid which in aqueous systems is associated with hydroxyl ions or water molecules. The latter commonly dissociates prior to adsorption, leaving the surface with hydroxyl groups.

3.2.1 Protonation

Protonation is a process between protons and the surface groups of solid iron oxide. This is generally accepted as the first step of the dissolution reaction on the surface of iron oxides. The general reaction between Fe (III) oxide and protons proceeds according to Eq (1):

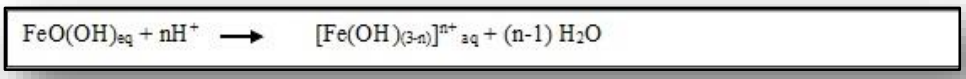

(1)

This is a simplified reaction mechanism but actually consists of several steps. According to Stumm and Furrer (1987), the iron oxide particle is suspended in an acidic solution, and electrical double layer forms on the interface. In other words, the OH group adsorbs a proton, changing the neutral surface group in a positively charged group (i.e. OH/OH_2 become Fe(III) $(OH_2)^{2+}$. Two more protons are then adsorbed, which promotes the polarisation and resulting in weakening of the Fe-O bond. Once the metal-oxygen bond is loosened due to the protonation process, the surface hydroxyl groups (-OH) become active sites for the subsequent adsorption of organic ligands (Sidhu *et al*. 1981). The adsorption of protons onto the surface of the oxide is commonly fast, and the actual rate-determining step is the detachment of iron oxide from the lattice.

Dissolution of iron oxide by hydrochloric acid (HCl) and nitric acid (HNO_3) is governed by protonation, but the anions of the acids are not without importance. The anions can promote the dissolution of iron oxides by replacing the surface OH group and facilitating the detachment of Fe atoms when dissolving different iron oxides with HCl and perchloric acid ($HClO_4$) (Sidhu *et al*., 1981). In an experiment to determine the efficiency of two acids to dissolve synthetic iron oxide, hydro- and oxy-hydro were contrasted by Sidhu *et al.* (1981) to which they found the dissolution to be faster in HCl and an increased dissolution rate in the presence of proton and chloride. The dissolution was found to be via proton attack (Sidhu *et al*., 1981); dissolution in HCl involves protonation of the oxide surface together with formation of a chloride-Fe

surface complex, followed by the rate determining step, namely the breaking of the Fe-O bond (Sidhu *et al.* 1981). The same conditions were used for both hydro and oxy-hydro. From the experiment it was also found that the formation of iron-chloride complexes assists in the dissolution process. Additional to this, the usage of sodium chloride increases the ionic strength of HCl and enhances the dissolution rate. From their experiment, Sidhu *et al.* (1981) were able to conclude that protons are the most essential components in the dissolution of iron oxides.

3.2.2 Complexation

Complexation is simply a ligand-promoted dissolution, whereby a reaction between the surface groups of the oxide and the complexing ligand of the solvent occurs, and in turn promotes the detachment of the iron together with the ligand from the surface of the solid.

$$Fe(III)(OH)_s + L^- + H^+ \longrightarrow Fe(III)L_s + H_2O \longrightarrow Fe(III)L_{aq} + H_2O \qquad (2)$$

Complexation is initiated by adsorption of the ligand onto the surface and followed by the detachment, or desorption, of the metal with the ligand and their subsequent transfer into the solution phase. At this stage, the surface is left with reactive O^- and OH^- sites which are protonated and the surface is restored. Reductive dissolution takes place once Fe(II) ions have been generated in the solution after an induction period. Fe(II) is present in the lattice in magnetite, so Fe(II) can be generated through dissolution. For hematite, however, that contains no lattice Fe(II), the generation of Fe(II) is through electron transfer from the ligand to the Fe(III) ions. After the generation of Fe(II), the dissolution process becomes autocatalytic and the rate of dissolution is increased significantly. The factors affecting the dissolution mechanism include the pH and temperature of the solution, illumination by UV light and the addition of bivalent iron to the initial solution (Panias *et al.*, 1996). Panias *et al.* (1996) have also shown oxalic acid as a good complexing agent. The oxalate ion can be adsorbed onto the surface of the oxide to form a strong surface complex (Eq. 3). After the metal atom detaches the surface with the ligand, the negative surface is restored by protonation.

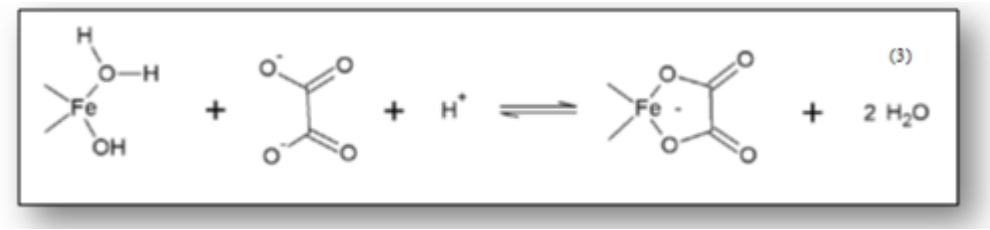

3.2.3 Reduction

Reduction is a process where lattice Fe(III) is reduced to Fe(II). The process requires electron transfer, which can take place either through adsorption of the electron donor, through cathodic polarisation of a supporting electrode, or through electron transfer from a ternary surface complex. As a result, reduction is a complicated mechanism and cannot simply be explained by generic reaction equations. When Fe(III) is reduced to Fe(II), the loss of charge and the change in the physical size of the atom facilitate the detachment of Fe(II) from the lattice. Several different reductants for the dissolution of iron oxide have been studied. Dithionite has been shown to be an efficient dissolving agent for iron oxides but it decomposes rapidly, producing hydrogen sulphide in an acid medium. The use of sodium bicarbonate ($NaHCO_3$) as a buffer has been reported to reduce the effect of dissolution the decomposition of dithionite (Mehra and Jackson, 1960). The $NaHCO_3$ maintains the pH 7.3, with sodium sulphate (Na_2SO_4) added in a solid form to avoid any precipitation of S and FeS.

3.3 Review on hematite dissolution

Although many iron oxides have been studied extensively and reported in literature with respect to their solubility behaviour, for the purpose of this study only hematite will be reviewed because is essentially the sole oxide phase in the iron ores of the Transvaal Supergroup.

The acidic dissolution of hematite has been studied by Wells *et al.* (2001), who found that the Avrami-Erofe'ev equation governs the rate of dissolution of substituted hematite in HCl. Sidhu *et al.* (1981) used HCl at 60°C and observed that hematite had the slowest rate of dissolution per unit surface area after goethite. Gorichev and Kipriyanov (1984) have also provided an extensive review on the dissolution of metal oxides in acidic media. In their review they discuss the influence of protons on the dissolution as well as the anions of the acids. They also show that there is a direct correlation between the increase in concentration of protons and rate of

dissolution. Hematite dissolution in HNO_3 has the order of reaction between 0.5-0.6 with respect to hydrogen ions (Gorichev and Kipriyanov 1984). The anions of the acid form complexes with the oxide surface and in the process increase the rate of dissolution. When hematite is dissolved using NO_3^-, the order of reaction have been reported to be 0.3.

Oxalate dissolution of hematite was studied by Banwart *et al.* (1989), who reported that dissolution of hematite in the presence of oxalate is purely ligand-promoted and no redox reaction takes place. It is also shown that ascorbate as a reducing agent can increase the rate of reductive dissolution. The pH was not reported to increase at any time during the dissolution. Panias *et al*. (1996) suggested that the dissolution by oxalic acid involves a step of reductive dissolution, and thus that ligand mechanism is not exclusively involved. Additional studies using oxalic acid for the dissolution of metal oxides were conducted by Taxiarchou *et al*. (1997a, 1997b). These authors studied the effect of temperature, oxalate concentration and the pH on the dissolution of hematite. They found that the dissolution rate of hematite was dependent on temperature as well as on pH. Oxalate concentration was found not to affect the dissolution when it lies between 0.1 and 0.5 mol/L at the pH value of 1. The concentration of divalent iron in the solution was found to be a significant factor for the dissolution of hematite, whereas the oxidation of Fe^{2+} to Fe^{3+} was found to depend on pH.

More recent studies were conducted by Lee *et al*. (2006), who suggested that dissolution of hematite by oxalic acid is not governed by complexation but rather by solid-state reduction of the lattice Fe(III). Lee *et al.* (2006) have also shown that the formation of solid Fe(II) oxalate can in fact inhibit the dissolution of hematite. The solid oxalate forms only between pH values of roughly 1.6-3.2 (Lee *et al.*, 2007). Where the pH and concentration is investigated, the two are shown to be not co-dependent. Oxalic concentration was adjusted with oxalic acid, while NH_4OH was used to determine the pH. This means that the pH effect was studied at a constant oxalic acid concentration.

Finally, ultraviolet wavelength radiation has been reported to enhance dissolution of hematite using oxalic acid (Panias *et al.*, 1996). The same effect can be brought about via the use of several chelating agents such as EDTA (Chang and Matijevic, 1983). EDTA specifically enhances dissolution of hematite at low temperatures in basic systems (Chang and Matijevic, 1983).

3.4 Experimental

3.4.1 Materials

The 29 high-grade hematite iron ore samples used in this study were initially crushed to a very fine powder (Appendix A). The effects of particle size were not considered in this study, although the particle size distribution plays a major role in the dissolution kinetics and possibly also in thermodynamics (Sidhu *et al.,* 1981). Oxalic acid powder ($H_2C_2O_4$) (99.99%), nitric acid (65% HNO_3), hydrofluoric acid (45% HF) and ammonium hydroxide (NH_4OH) of purity higher than 95%, were purchased from Sigma-Aldrich (South Africa). All reagents were of analytical or HPLC grade. Ultrapure water was prepared at the Chemistry Department, Rhodes University.

3.4.2 Dissolution of ore-hematite using the oxalic acid method

Oxalic acid was chosen as the solvent because the iron ores in this study are largely hematite and the oxalate has been reported to dissolve hematite at a fast rate (Pinias *et al*., 1996).The dissolution experiments were conducted in a well-ventilated fume-hood. All experiments were conducted in 0.7 mol/L oxalic acid at a temperature of 60°C at first and ultimately at 100°C. Reaction solutions were prepared in ultrapure water. The initial mass of the fine crushed powder of hematite in the dissolution experiments was chosen to be approximately 0.5 g for each reaction; the exact amount about that value was recorded to the fourth decimal for each sample, and reported in the Appendix C. The initial pH in the experiments was 2.5 and pH was constantly measured with a probe. The pH at 2.5 should eliminate the risk of formation of an inhibiting product layer, as the solid Fe oxalate has been shown not to be stable at such low pH (Cornell and Schindler, 1987).

The oxalic acid dissolution method for dissolving iron oxide described by Lee *et al*. (2006) was employed with slight modification. An aqueous solution of oxalic acid ($H_2C_2O_4$) (0.7 mol/L) was prepared in a rounded bottom flask (1 L) using 0.5 L of distilled water with continuous stirring for 10 minutes. A 100-1000 µL pipette was used to add NH_4OH (0.2 M) under vigorous stirring until a pH of 2.5 was achieved. The solution mixture was then placed on a hotplate with a condenser connected to the round-bottom flask with continuous stirring. The solution mixture was left on the hotplate until 60°C was reached. After the solution mixture reached the required temperature of 60°C, approximately 0.5g of fine hematite powder from a

test ore sample collected from the Beeshoek iron-ore open-pit was added in the hot solution mixture. After addition of the hematite powder, the solution turned brown reddish in colour. The resultant reaction "slurry" was initially left for 24 hours on the hotplate for the reaction to reach completion. After the first 24 hours, the brown-reddish slurry solution mixture remained unchanged. The solution mixture was then left for an additional 48 hours after which the colour of the solution continued to remain unchanged, suggesting that the dissolution rate was slow. The reaction was left on a hot plate for another 24 hours, until it was observed that the colour of the solution mixture started to change to a golden-yellow colour. The latter was therefore observed only after a total of 96 hours had passed before for the iron oxide-rich powder had started to dissolve appreciably. Complete reaction of the iron oxide was only achieved after reaction at 60°C over a time period exceeding six days.

The experiment was therefore further optimised by increasing the temperature to 100°C at pH 2.5 and 0.7mol/L concentration of the acid. The reaction was found to reach complete dissolution of iron oxide after 76 hours at temperature of 100°C. It was therefore at this temperature that all dissolution experiments were eventually conducted. It is obvious after the initial tests that temperature and pH affect the dissolution rate of iron oxide exactly as originally reported by Panias *et al.* 1996. The diagram in figure 14 shows the reaction schematic of oxalic acid dissolution of iron oxide.

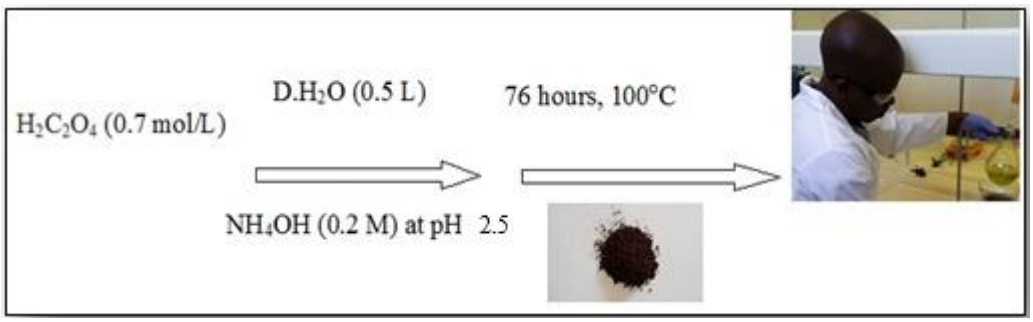

Figure 14: Schematic representation of oxalic acid dissolution of iron oxide

3.4.3 Collection and dissolution of the non-ferrous fraction

Upon each dissolution routine, the hot golden-yellow solution for each sample was removed from the hotplate and allowed to cool for 1 hour. After cooling, 150mm of qualitative filter paper (8 µm pore size) was used to collect the non-ferrous (matrix) residue. This was arguably one of the most testing steps in the process, as the residues were found to be very fine and of

sometimes very small volume and quantity to be trapped efficiently on a filter paper. Each sample solution was transferred into a 50 mL centrifuge tube. The solution was centrifuged for 40 minutes to recover the matrix residue. After the centrifugation step, the particle-free ferrous solutions were transferred back into the beakers, while the residues corresponding to the non-ferrous, matrix fraction of the original powders were dried in an oven at 50°C, and stored in clean glass vials.

The stored matrix powders were subsequently transferred into clean, small Savillex beakers. In a fume-cupboard, hydrofluoric acid (HF) (4mL) was added to each sample beaker. Once the samples were fully digested, the beakers were opened and the solutions were left on the hotplates and allowed to evaporate to complete dryness. Once the samples had dried down they were removed from the hotplates and allowed to cool. Using a 100-1000 µL pipette and a clean pipette tip, 4 mL of 5% nitric acid (HNO_3) was added to each sample. The beakers were then closed and placed on the hotplates until the samples were completely dissolved. Once the samples had completely dissolved the beakers were opened and the solutions left on the hotplates to evaporate to complete dryness. The process of adding another 4 mL of 5% HNO_3 to each sample was repeated, using a 100-1000 µL pipette. The amount of 6mL of ultrapure water was added to each beaker rendering the samples ready for further dilution prior to instrumental measurement.

3.4.4 Solvent evaporation and Fe-oxide collection/digestion

Each ferrous solution was evaporated to remove the solvent. After complete removal of the solvent, the remaining residue for each sample comprised an assemblage of crystalline, ferrous organic deposits of a characteristic greenish-yellow colour. The total mass of this residual material was weighed on a microbalance and the weight was recorded. Approximately half of the total residue for each sample was then transferred into a clean, dry fused-silica crucible. The crucibles were placed in a preheated furnace for 24 hours, with the purpose of breaking down ("ashing") the produced ferrous organic salts back into pure Fe-oxide. Over the first 4 hours, the oven temperature was incrementally increased to the maximum temperature (i.e. from 110°C until 150°C, with 10°C increments) to prevent "bubbling" of the collected material over the crucibles and consequent partial sample loss. The crucibles were thereafter left in the furnace for another 20 hours to effect complete ashing of the sample. After 24 hours, a residual, dry red iron oxide powder had been produced for each sample, which was placed in a desiccator

to allow cooling. After about 8 hours in the desiccator, the mass of each sample was weighed to the fourth decimal and the weighed samples were transferred into clean glass vials.

Approximately 50 mg of each iron-oxide sample powder were transferred into clean, small Savillex beakers. In a fume-cupboard, hydrofluoric acid (4mL) was added to each beaker. The beakers were tied sealed and placed on a 50-60°C hotplate for 48 hours. Once the samples were fully digested, the beakers were opened and the solutions were left on the hotplates and allowed to evaporate. Once the samples had dried they were removed from the hotplates and allowed to cool. Using a 100-1000 µL pipette and a clean pipette tip, 2 ml of concentrated 65% nitric acid (HNO_3) was added to each sample. The beakers were then closed and placed on the hotplates until the samples were completely dissolved. Once the samples had completely dissolved, the beakers were opened and the solutions left on the hotplates to evaporate to complete dryness. The process of adding another 2 mL of concentrated nitric acid (HNO_3) to each sample was repeated, using a 100-1000 µL pipette. The samples were then allowed to evaporate again to complete dryness, removed from the hotplates and allowed to cool. Using a 1-10 mL pipette and a clean pipette tip, 4 mL of internal standard stock solution was added to each sample beaker. The sample beakers were then placed in an ultrasonic bath for 60 minutes to dissolve completely.

3.4.5 Preparation of non-ferrous and ferrous fraction solutions for ICP-MS analyses

The following steps were applied to both non-ferrous and ferrous solutions en route to analysis via ICP-MS. The dissolved samples were quantitatively transferred to a 50 mL centrifuge tube. The sample beaker was then washed with 2 mL of internal standard stock solution, with care being taken to collect any droplets on the beaker walls, and transferred to the centrifuge tube. On a microbalance, the dissolved sample was then made up to 50 g using internal standard stock solution**.** The sample solution represented a 1000-fold dilution of the original solid sample in each fractions and was then ready for further dilution.

The ferrous solutions were diluted by a further 5-fold using the internal standard stock solution. The solutions then represented a 5000-fold dilution of the original solid iron-oxide sample. The internal standards used during the analytical process include international standard BHV- 02 and internal standard stock solution containing 5% HNO_3 with 4 additional standards. In

addition, a total procedural blank (TPB) was run in order to establish the levels of contamination in the preparation and analytical processes.

A binary plot was plotted in Figure 15 to test whether the separation experiment was successful. The bulk iron-oxide content of the samples as analysed using XRF was plotted against the mass of iron oxide recovered after the dissolution protocol was applied. Samples B1, B2 and N1 from the Hotazel area which contain significant bulk quantities of Mn were excluded from the plot, as Mn-hosting species were also evidently dissolved through the dissolution process applied (see also Appendix C, Table 1). A regression of an R^2 value at 0.902 suggests that the analytical protocol followed here resulted in a generally good quantitative dissolution and re-capturing of the ferrous oxide fraction of the ores, on the assumption that all Fe in the iron ores is hosted in hematite only. It is therefore contended that the oxalic acid method at 100 °C was ultimately successful and suitable for the efficient extraction of hematite, even in samples as rich in Fe-oxide as the studied ores.

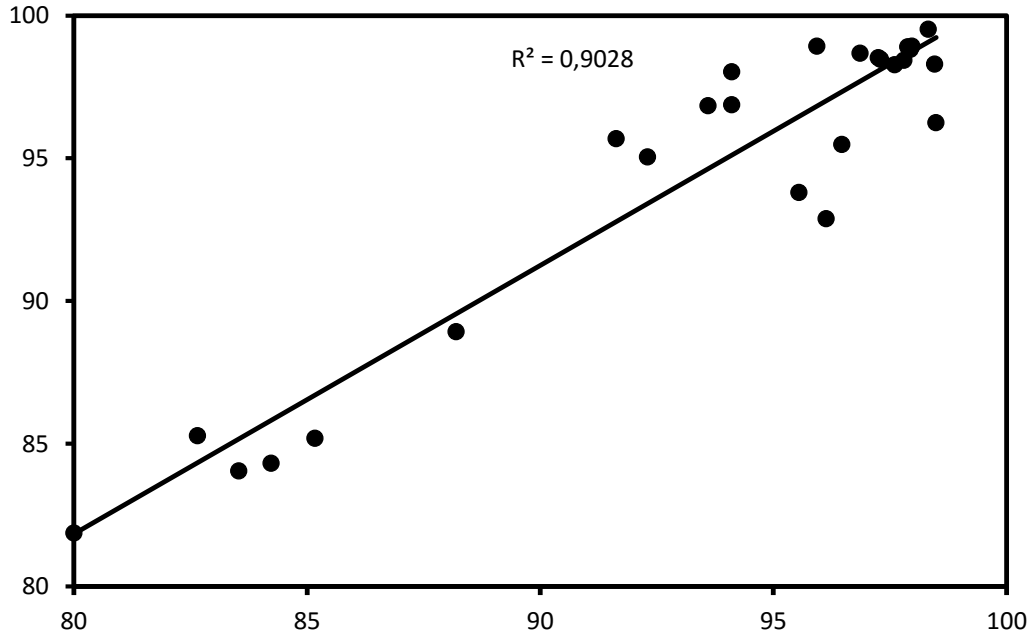

Figure 15: Binary graph illustrating whole-rock iron oxide concentrations as determined via XRF versus the corresponding mass of iron oxide as estimated following collection after partial oxalic acid dissolution of the same samples.

3.4.6 Analytical results and quality assessment

Major oxide concentrations were carried out using ICP-OES on the ferrous and non-ferrous solutions to further assess the efficiency and suitability of the dissolution method employed here, in the context of further geochemical applications. The raw data for the ferrous and non-ferrous fractions are presented in Appendix B4. Since digestion of powders was performed via HF dissolution, it is obvious that Si determinations are not shown as all silica would have evaporated during digestion as a fluoride complex (Tsolakidou *et al*., 2002).

As expected, the ferrous fraction is dominated by Fe_2O_3 at >98wt% for 22 out of the 29 samples analysed, and most other element oxides are present in extremely low to undetectable abundances. The detectable Al_2O_3 content of up to 3.5wt% (sample A8) present in the ferrous fraction of mainly the "A" samples from locality King/Khumani, may in fact be a constituent of the iron-oxide itself, through Fe(III) substitution by Al(III) during the geological history of the ores. Exception to this might be sample A8 itself which is the one with highest K content of 0.9wt%, which may imply the presence of very small amounts of reacted Al-silicate.

Sample B1 from the Hotazel area has a much lower Fe_2O_3 relative to other elements, which is due to the very high Mn content present in that sample associated with interbedded Mn-rich layers in the Hotazel formation. That Mn has evidently dissolved almost completely during the application of the oxalic acid protocol. The remaining Hotazel samples (B2, N1) are also enriched in Mn but only by a few wt%. In the case of sample B2, most of the Mn did not dissolve with the ferrous fraction as the data for the corresponding non-ferrous fraction shows (Appendix B4). Other Mn-rich samples are from the Khumani area and belong to the "W" group, and are associated with a manganiferous zone that characterises some of the iron ores in the Postmasburg region (Moore *et al.,* 2011). Again, Mn at the wt% level is detected in the ferrous fraction of at least sample W2. Another oxide that is detected in somewhat elevated concentrations with the Mn-rich samples B1 and W1 is CaO (2,9 and 1,1wt% respectively).

By contrast, the non-ferrous fraction data are dominated by mainly Al_2O_3 and variable concentratuions of alkalis and alkali earths, namely K, Na and Ca. These species are expected to be hosted mainly in phyllosilicate minerals (micas), whereas the Ca may also be contained in carbonate mineral species, particularly in the Mn-rich samples. As expected, elevated manganese concentrations are recorded in the samples of the manganiferous "W" group from King/Khumani and in the Hotazel group (B1,B2,N1). The very high Mn concentrations in

samples B2 and W4 suggests that Mn here was probably not in an oxalic acid-soluble form (unlike samples B1 and W2 earlier) and therefore was enriched in the non-ferrous matrix residue. Finally, the concentration of Fe_2O_3 across all non-ferrous matrix samples is highly

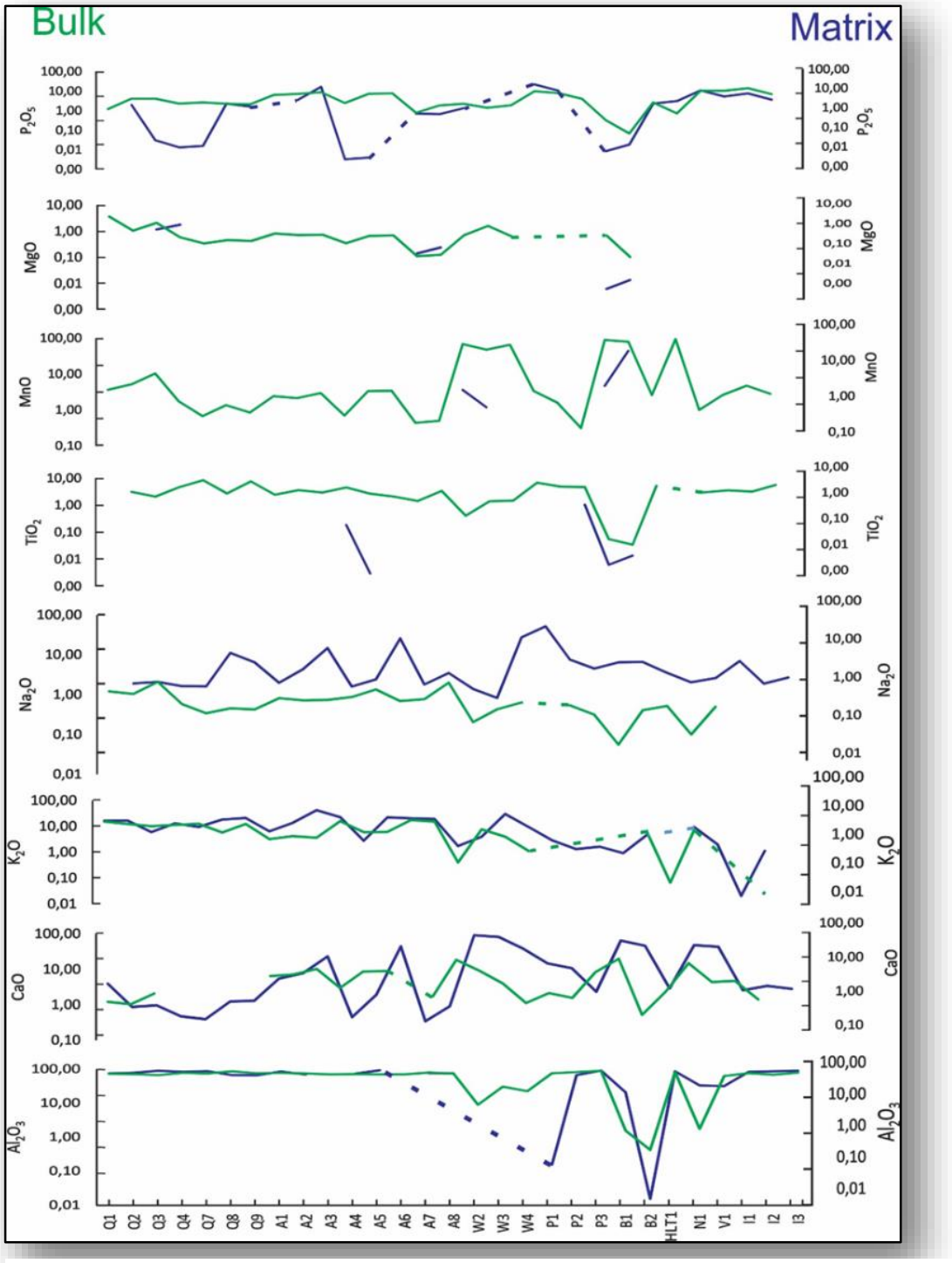

Figure 16: Bulk oxide abundances (via XRF, chapter 2 of this thesis) normalised to 100% on a Si-free basis, against corresponding normalised data from the measured major-element oxides in the non ferrous matrix via ICP-OES.

variable, from as low as undetectable (sample A6) to as high 48wt% (sample Q3). This may suggest that either Fe is present in the matrix in minerals not soluble by oxalic acid (i.e. silicates), and/or that very small amounts of hematite remain undissolved and therefore "contaminated" the non-ferrous residue. Due to the extremely low concentration of matrix material collected for most of the processed samples, it is impossible to constrain whether one and/or the other factor may affect the non-ferrous analytical results. Therefore, any conclusions drawn from the non-ferrous fraction analyses for REE as presented in the next chapter, will have to be treated with great caution.

Figure 16 plots the major oxide concentrations of the non-ferrous fraction against the values as determined from bulk sample XRF analyses, both normalised to 100% excluding total Si- and Fe-oxides. The plot was made to test whether the results and the protocol for the non-ferrous matrix fractions are broadly consistent with what would be expected from the bulk analyses, assuming all Fe is assigned to ore hematite (i.e. the ferrous fraction). The diagram shows that there is generally good agreement for Al_2O_3, K_2O, and P_2O_5, and to a much lesser degree for CaO and Na_2O. Most other element oxides had concentrations too low for most non- ferrous fraction samples to allow meaningful comparisons. In general, the analyses of the non-ferrous fractions have produced somewhat mixed results and reinforce the need expressed earlier for treating them with great caution.

4 Rare earth element geochemistry

4.1 Introduction

This chapter deals with the application of rare earth element (REE) geochemistry on the bulk and fraction-specific samples of iron ore selected for this study. A number of researchers have previously focused on rare earth element (REE) and stable isotope (mainly oxygen) applications on iron ores, with relevant results having being published from various iron ore deposits around the world (e.g. Powell *et al*., 1999; Gutzmer *et al*., 1996; Lobato *et al*., 2007; Figueiredo *et al*., 2008; Gutzmer *et al*., 2008; Roy and Venkatesh, 2009; Thorne *et al*., 2009). Gutzmer *et al.* (2008) have proposed that unique rare earth element geochemical fingerprints typify supergene high-grade hematite ores, which allow them to be classified accordingly. The same authors specifically argue that there are distinct enrichments in light rare earth elements (LREE) relative to heavy rare earth elements (HREE) that characterize all supergene high-grade iron ore deposits. This signature has likewise been observed in modern low-temperature environments affected by intense chemical weathering, whereby the mobilisation of HREE in weathering profiles and the concentration of LREE in the weathering residue is documented (Nelson *et al*., 2003).

In terms of constraining the likely protolith to iron ores, application of REE analyses can also be particularly useful. This can be done on the assumption that the REE can behave as immobile constituents in a variety of geological environments affected by fluids. In that case, the inference can be made that the REE patterns of bulk iron ore samples may preserve those of the parent rock that underwent iron replacement, which in the case of BIF has a well-documented seawater-like signature when normalized against average shale (e.g. Tsikos and Moore, 1997). By contrast, other rock types such as shales that may have also been protoliths to iron ore, may also be preserved through their characteristically expected flat REE patterns when normalized against average shale.

The aim of this part of study is to present, evaluate and discuss the results for rare-earth element measurements of bulk sample powders and their corresponding ferrous and non-ferrous matrix fractions. An attempt will be made to constrain whether the data are:

(i) Consistent across the entire sample set or vary from one locality to the next, within a single locality or even across a single drillcore;

(ii) whether or not the bulk signals are replicated by the ferrous fraction of the samples and/or the non-ferrous matrix fractions; and,

(iii) Whether or not the results can be interpreted collectively as a result of a single protolith control, multiple protoliths, inputs by exotic fluid/s, or any combination thereof.

It is important to stress that no attempt will be made to quantify certain parameters that are traditionally used in REE applications in geochemistry, such as Eu and Ce anomalies or quantitative expressions of the shape (e.g. slope) of the REE patterns (Taylor and McLennan, 1985). The iron ores investigated in this study represent complex assemblages of pre-existing rock fragments such as BIF and potentially other rocks as well, mixed with interstitial material of possibly diverse provenance that may have varied from one locality to the other. Furthermore, the ores are possibly also overprinted by REE and other chemical introductions through one or more generations of fluids that may have passed through the ores. Because of the complex history of the iron ores, and the fact that the fraction-specific analyses performed, especially for the non-ferrous matrix, did not produce unambiguous results, it is beyond the scope of this thesis to over-analyse and over-interpret the REE analyses. Instead, the data will be compared qualitatively and conclusions will be drawn on the basis of the relative variations of REE patterns across different localities and within a specific locality, where possible.

As indicated earlier, bulk REE analyses were obtained by means of the LA-ICP-MS technique on fused glass discs which were used also for major oxide and remaining trace element determinations (see Chapter 2). Fraction-specific analyses were performed also using the ICP-MS technique but on corresponding solutions at the Department of Geological Sciences, University of Cape Town. All raw data are presented in Appendix B**.**

4.1.1 Results: bulk REE normalised against average BIF

Bulk REE data show the following ranges across the entire sample-set: La concentration range between 1.18-29.53 ppm; Ce between 2.48-64.4 ppm; Pr between 0.26-7.06 ppm; Nd between 1.0-30.98 ppm; Gd between 0.35-8.03 ppm; Eu between 0.08-1.96 ppm; Tb between 0.03-1.22 ppm; Dy between 0.15-1.89 ppm; Ho between 0.08-2.26 ppm; Er between 0.16- 1.45 ppm; Tm between 0.01-0.25 ppm; Yb between 0.08-4.75 ppm; and Lu between 0.01-0.85 ppm.

The concentrations of REE in each iron-ore sample were first normalized and graphically presented in the form of spidergrams against the average Kuruman-BIF (Oonk 2017,

Unpublished). The diagrams facilitate comparisons with the Kuruman BIF as one of the most probable protoliths for the iron ores dealt with in this thesis, as well as between different samples. In the BIF-normalised spidergrams, four distinct groups of REE patterns are present (Fig. 17). Figure 17a shows a pattern of slight to moderate enrichment of the "middle" REE (Sm to Ho) relative to either both the HREE and the LREE (sample V1), or to the HREE only (sample HLT1). This results in the characteristic middle "hump" pattern as shown in Figure 17a. Both these samples are from the iron-ore exploration area 20km NW of Postmasburg at locality Heuninkranz. Figure 17b shows a clear flat pattern and relatively lower values for the LREE (La-Sm), followed by a steep positive slope from Sm to Tb and then flat but relatively enriched HREE. This pattern applies to samples A5 and A6 from the King locality. Figure 17c displays relatively "flat" REE pattern for a total of nine samples, which show positive, negative or no anomalies in their Ce. These are the samples with the most obvious BIF-like pattern in their REE distribution and come from the King-Khumani locality. It is worth noting that the negative Ce anomalies are observed only in samples from the Hotazel area, implying a possible connection with the high Mn content recorded in those specific samples. Finally, in Figure 17d there is a generally negative slope observed in all remaining 16 REE patterns, that is, there is a progressive decline in the normalized abundance of REE from the lightest to the heaviest. Like with the patterns in diagram 17c, there are variably positive and negative Ce anomalies observed across all samples in this class. The implication of these observations will be discussed later in more detail in chapter five.

4.1.2 Bulk REE normalized relative to PAAS

The concentrations of REE in each hematite sample were also normalized and graphically presented in the spidergrams against Post-Archaean Average Shale (PAAS; Taylor and Mclennan, 1985). The graphs are presented below in Figure 18, which summarizes the patterns seen again into three broad categories, in a similar fashion to the BIF-normalised ones. Diagram 18a includes all samples for which PAAS-normalised REE data show a flat to marginally-positive pattern, the latter suggesting a slight depletion of LREE relative to HREE. The great majority of samples belong to this class, and show highly variable positive and negative Ce and Eu anomalies. These samples are derived from essentially all localities and exhibit patterns that are most shale-like, hence the flat distribution. By contrast, plot 18b shows three samples

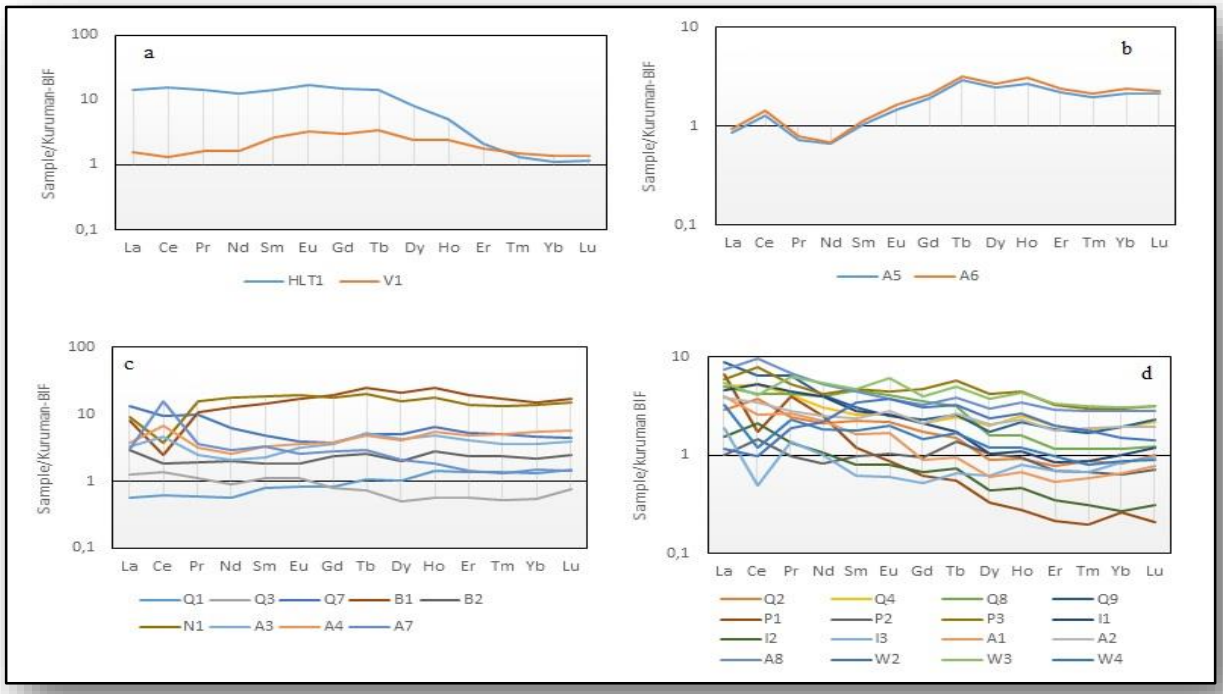

Figure 17: Bulk REE data normalised against average Kuruman BIF (BIF data from Oonk, 2017, unpublished).

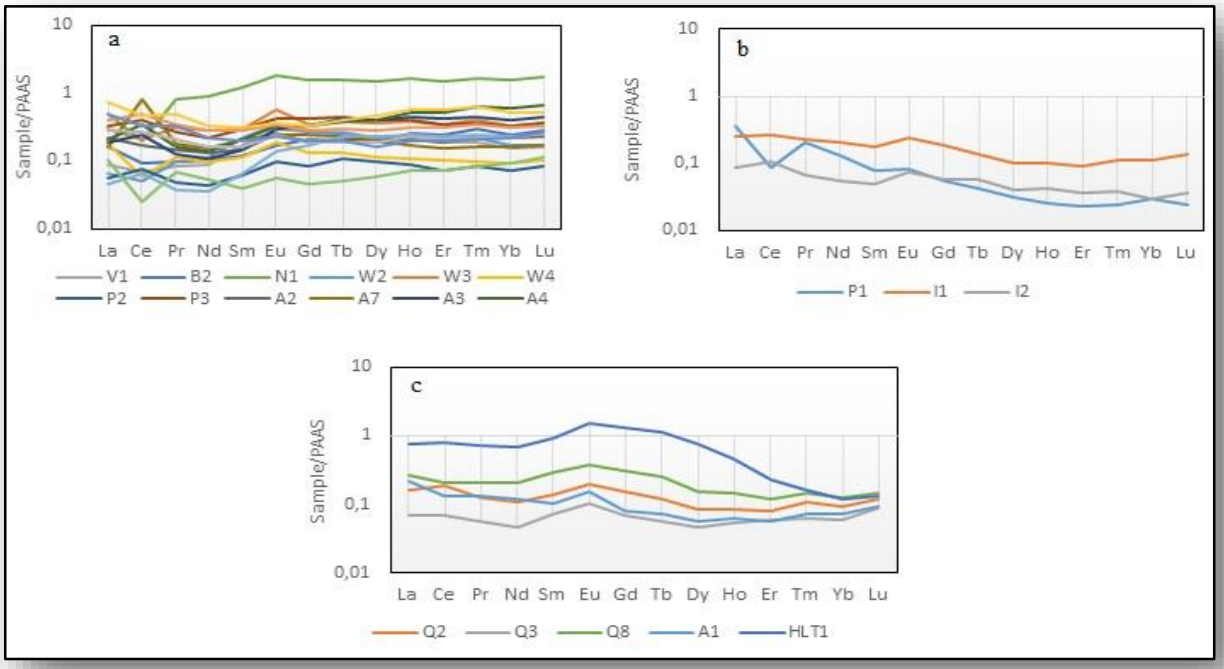

Figure 18: summary of bulk REE data normalised against PAAS (Taylor and Mclennan, 1985)

(all fom the Beeshoek area) in which a slight depletion in HREE relative to LREE is observed, resulting in a negative slope. The same samples also show appreciable variation in their Ce behavior. Finally, Figure 18c shows five samples which appear to share a distinct enrichment of MREE (Nd-Dy), resulting in an obvious middle “hump” which looks most prominent in the

samples with the highest abundance of REE.

4.2 Fraction-specific REE controls

In the previous chapter was presented a detailed account of the protocol used to separate the non-ferrous matrix from the abundant Fe-oxide (as hematite) in solution. This exercise was undertaken for the first time ever for the iron ores of the Northern Cape Province of South Africa, to assess what the relative chemical effect of each fraction is in the ores across space, and therefore interrogate and understand better the bulk REE geochemical signatures. The analytical results cast some doubt on whether the technique used was an unqualified success. Firstly, the great majority of the ore samples are overwhelmed so much by the abundance of hematite that the matrix volume recovered was invariably very small and extremely hard to collect clean and whole in most instances. The matrix analyses have also shown that there is measurable amount of iron in many samples (Appendix B4). This makes it difficult to ascertain whether the iron that is present represents residual unreacted hematite, or iron contained in silicate minerals of the matrix, that is, iron in minerals other than hematite. Therefore, the matrix analytical data cannot be considered as truly representative of the non-ferrous fraction of the ores, unless a very detailed mineral-specific analytical study were to be undertaken on the non-hematite mineralogy of every ore sample used in this study. Such an approach is practically very challenging and was beyond the scope of the present thesis.

On the above basis, it is very difficult to treat the matrix REE data produced in this thesis without a great deal of uncertainty and caution. However, the fact that the ferrous fraction represents essentially pure hematite, means that the data for the ferrous fractions themselves can be used far more constructively, at least in their comparisons with the bulk REE data. One of the issues with the iron ores of this study concerns exactly what the matrix represents: Is it residual rock material from the original rock that was replaced by iron to form the ores? Is it exotic particulate material introduced during the period of supergene weathering thought to have formed the ores? Is it material introduced in solution by hydrothermal fluids? Or is it variable combinations of all these three (or more) possible sources? Moreover, what is the partitioning of the REE in the ores? Are they hosted mainly in the ferrous (hematite) fraction, or is it possible that the matrix may contain accessory minerals that have a disproportionate effect on the REE distribution (such as the phosphate phases apatite or monazite) and thus

control the bulk REE? These and other issues may be further elucidated through the fraction-specific REE data produced in this study.

In this section, the BIF- and PAAS-normalised REE results of the bulk and corresponding ferrous and non-ferrous fractions are compared and contrasted. In all diagrams, the normalised bulk REE fraction is shown in black, the ferrous fraction in red, and the non-ferrous matrix fraction in blue. The samples labelled "A" and "Q" are discussed separately in the next section, as these are collected from single drillcores and are statistically sufficient to provide insights into REE v ariations within a single ore intersection.

4.2.1 BIF-normalised REE data: bulk versus fraction-specific signals

The first point to mention in the BIF-normalised REE patterns of Figure 19 & 20 which applies across the whole dataset shown, is that the REE are generally more enriched relative to average Kuruman BIF (except for sample I2) and are controlled by the ferrous fraction. This is a fundamentally important observation which confirms that at least the bulk REE analyses are reflective of the iron component of the ores only, and are not disproportionately influenced by the non-ferrous matrix. Exception to this norm is the high Mn samples from Hotazel, where the matrix can have a considerable influence on the bulk REE signature quantitatively and qualitatively, such as with sample B1.

In terms of the non-ferrous matrix REE signatures, some of the samples have REE patterns that are spiky (e.g. sample W4 and I2) or show unexpected positive or negative anomalies in certain REE (e.g. Ho in sample I1, Tm in sample P3, or Pr in sample P2). These are possibly related to analytical errors or artifacts which would result from the very low REE abundances retrieved from the matrix samples in general. Despite these anomalies, it can be argued within reason that the overall broad geometry of the REE patterns of the non-ferrous matrix samples, conforms well for most samples with those of the bulk and ferrous matrix, with possible exceptions the Mn-rich samples from Hotazel (B1, B2), and Beeshoek (I1-P3).

With regard to variations in the geometry of the REE spidergrams for bulk and ferrous fraction samples, there is no systematic trend to be observed. Samples from Beeshoek ("I" and "P") show patterns that have negative slopes with negative Ce anomalies (P1 and P2), or generally flat but variably "wavy" patterns with inconsistent fluctuations in the relative BIF-normalised

abundances from light to middle and finally heavy REE (I1, I2, I3 and P3). The two samples from Heuninkranz are themselves dissimilar, with V1 having a flat wavy pattern similar to

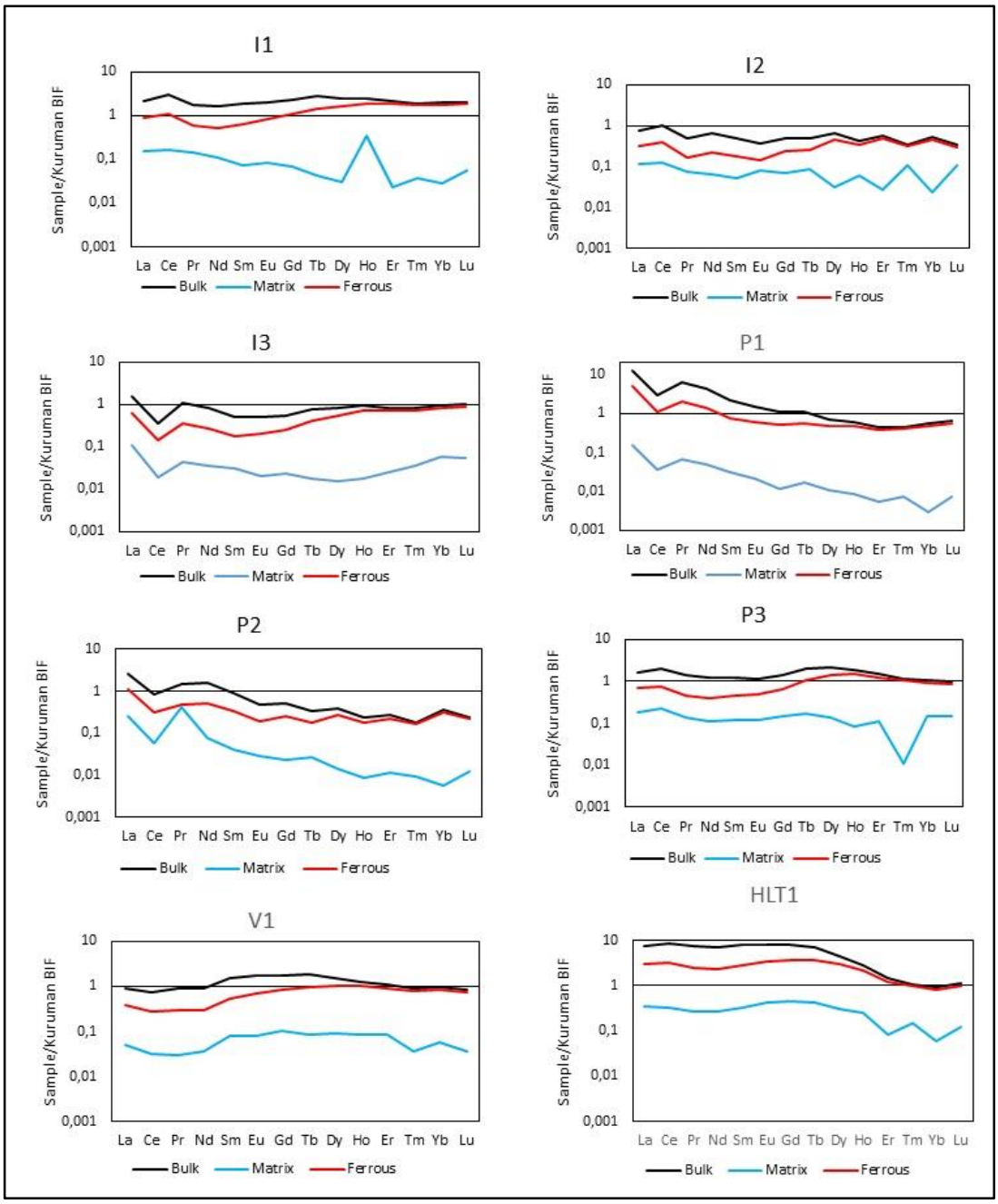

Figure 19: BIF-normalised REE data for bulk samples and corresponding ferrous/matrix fractions of all Mn-poor iron ore samples used in this study (average BIF data from Oonk 2017, unpublished).

sample P3 from Beeshoek, whereas sample HLT1 has strongly enriched, flat light and middle REE followed by a steep drop to relatively depleted HREE (Dy to Lu). Finally, all Mn-rich samples from King/Khumani ("W") and Hotazel (Fig. 20), show generally flat to very slightly

positive-sloping patterns and therefore more BIF-like ones, in most instances with a clear negative Ce anomaly (except for sample B1).

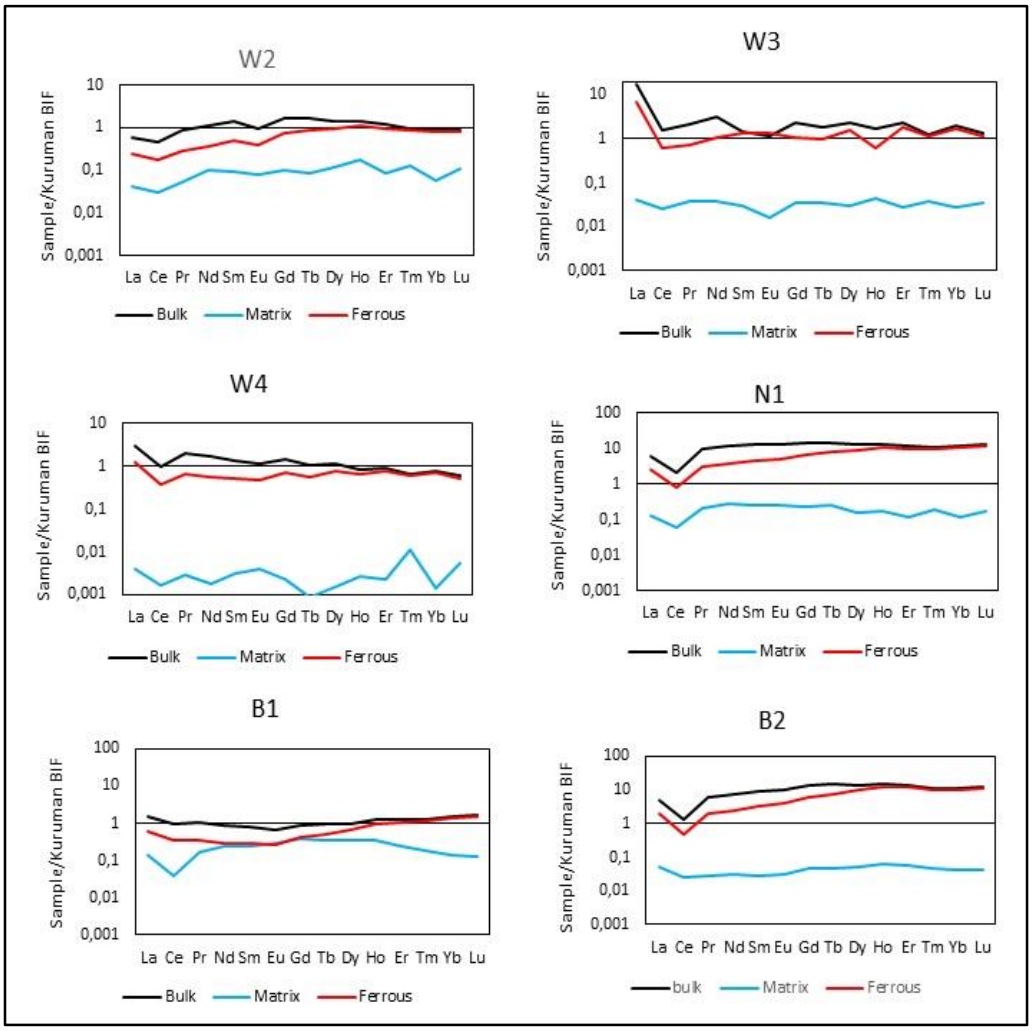

Figure 20: BIF-normalised REE data for bulk samples and corresponding ferrous/matrix fractions of all Mn-rich iron ore samples used in this study (average BIF data from Oonk 2017, unpublished)

4.2.2 PAAS-normalised REE data: bulk versus fraction-specific signals

The PAAS-normalised patterns of Figures 22 & 23 show relative depletion in absolute REE abundances than average shale. As expected from the average BIF-normalised REE, they also show that the ferrous fractions and the bulk samples have closely similar REE patterns, with only exceptions the Hotazel samples B1 and B2 where the ferrous fraction REE appear flatter than the bulk signal. Instead, the latter compares much closer with the non-ferrous fractions for those two samples especially in terms of respective negative Ce and Tm anomalies observed.

The non-ferrous matrix REE agrees with the bulk and ferrous oxide patterns well in all remaining samples, except for sample V1 from Heuninkranz and P2 from Beeshoek.

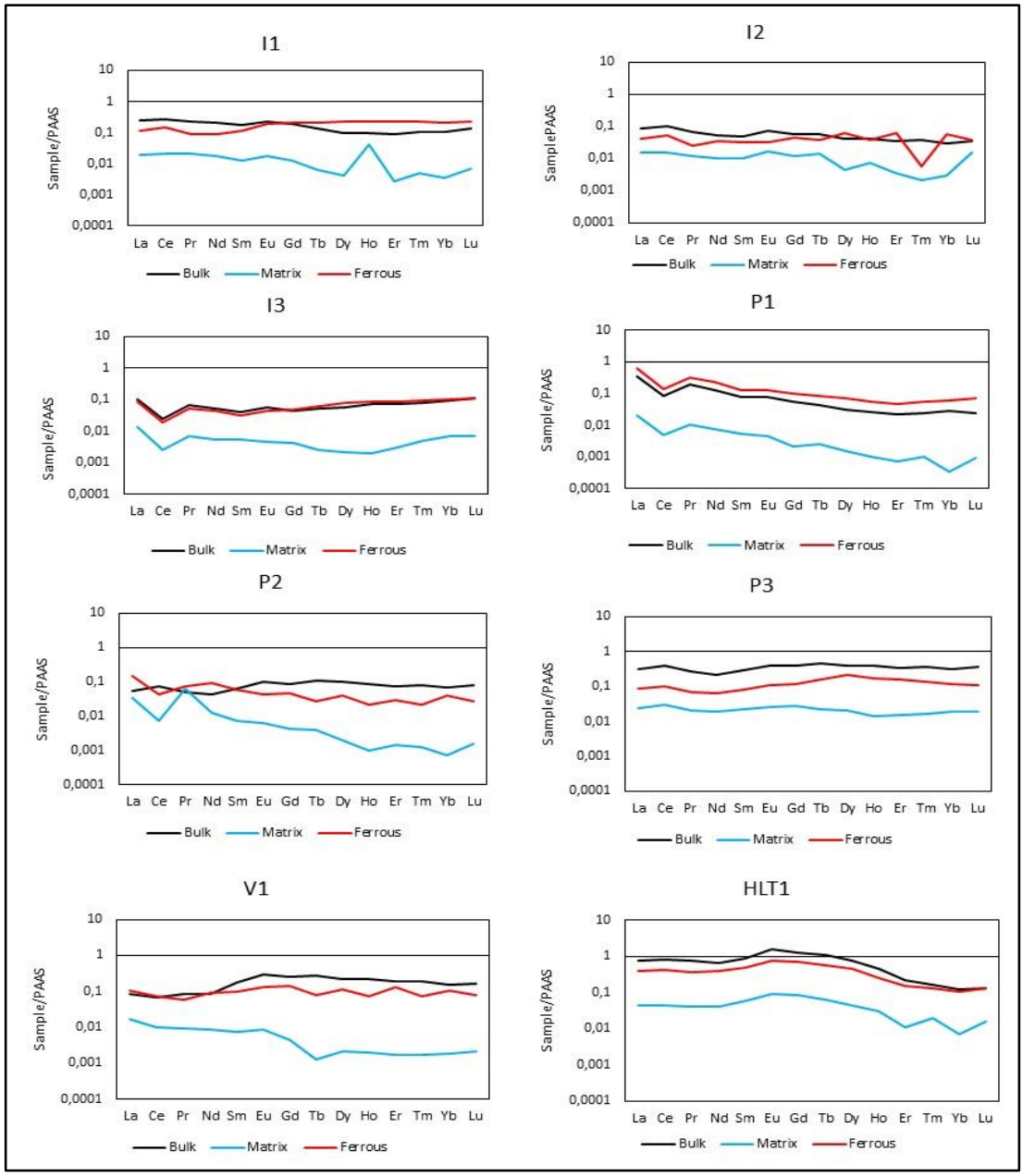

Figure 21: PAAS-normalised REE data for bulk samples and corresponding ferrous/matrix fractions of all Mn-poor iron ore samples used in this study (PAAS data from Taylor & McLennan, 1985).

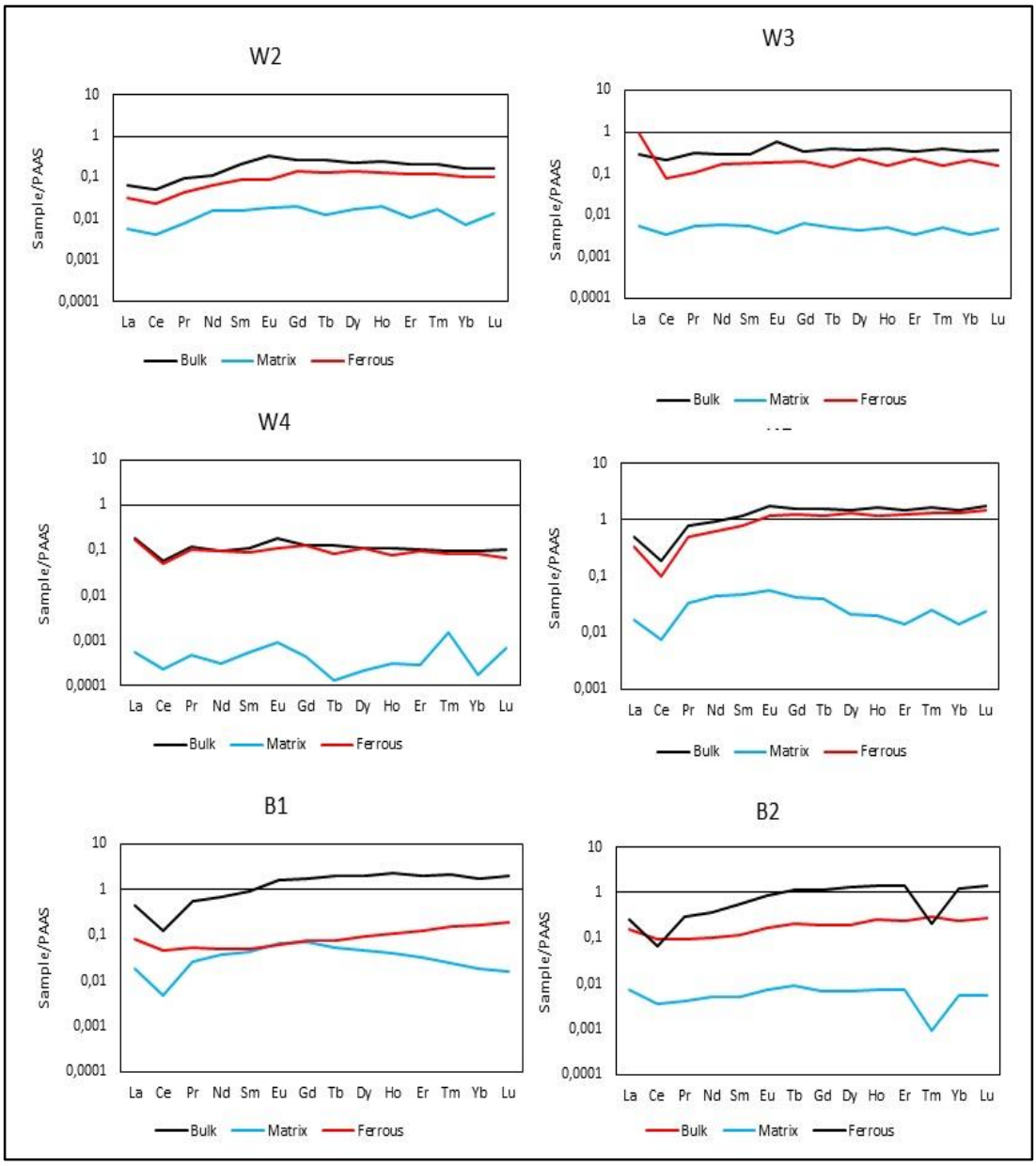

Figure 22: PAAS-normalised REE data for bulk samples and corresponding ferrous/matrix fractions of all Mn-rich iron ore samples used in this study (PAAS data from Taylor & McLennan, 1985).

In terms of REE geometry, the bulk and ferrous fraction REE patterns are essentially flat in the majority of instances and thus compare well with average shale. Exceptions to this are: Sample P1 from Beeshoek which has in fact a negative slope with a clear negative Ce anomaly; samples V1 and HLT1 from Heuninkranz which show relatively low LREE and HREE respectively and flat signal in the remaining REE; and Mn-rich samples W2 (Khumani) and all from Hotazel, which show relatively depleted LREE and flat to slightly positive-sloping REE at higher atomic weights.

4.2.3 Stratigraphic REE variations (A and Q samples, King/Khumani)

As indicated earlier, samples “Q” and “A” from the King/Khumani area provide sufficient stratigrahic resolution across their respective drill-cores that allow one to gain insights into possible stratigraphic variations in REE and their controls. All results here are normalised again against average BIF and PAAS, and are shown in Figures 24, 25, 26 and 27, respectively for drillcore QK first and for ALK afterwards.

Drillcore QK

Drillcore QK was sampled at relatively higher resolution than most other drillcores, as it contains texturally different types of iron ore stratigraphically, namely conglomeratic ore at the topmost part of the section immediately underlying the Olifantshoek shales, breccia-style ore over most part of the intersection lower, and ultimately more laminated-type ore at the basal part of the ore intersection. The collected samples straddle across all these three different ore types, and therefore the REE data obtained can shed light particularly with regard to variations in the texture of iron ore.

In terms of bulk versus fraction-specific REE signatures recorded in the BIF-normalised samples, similarly to data shown earlier. The non-ferrous matrix REE samples appear comparable in terms of overall geometry to the bulk and the ferrous fraction, except for the lowermost three which show some differences. The bulk and ferrous fractions show essentially smooth negative-sloping patterns for the top four samples across conglomeratic and breccia ore, and the non-ferrous matrix fractions seem to follow the same general pattern but with much lower absolute REE abundances. Lower in the stratigraphy of the ore intersection and as the ore transitions to a more laminated-type, the bulk and ferrous-fraction patterns become flatter, that is much more BIF-like, and ultimately the lowermost sample Q1 shows even a gently positive sloping pattern for both bulk and the ferrous fraction. For the same three samples, the non-ferrous matrix is initially positive-sloping and ultimately becomes flatter at sample Q1.

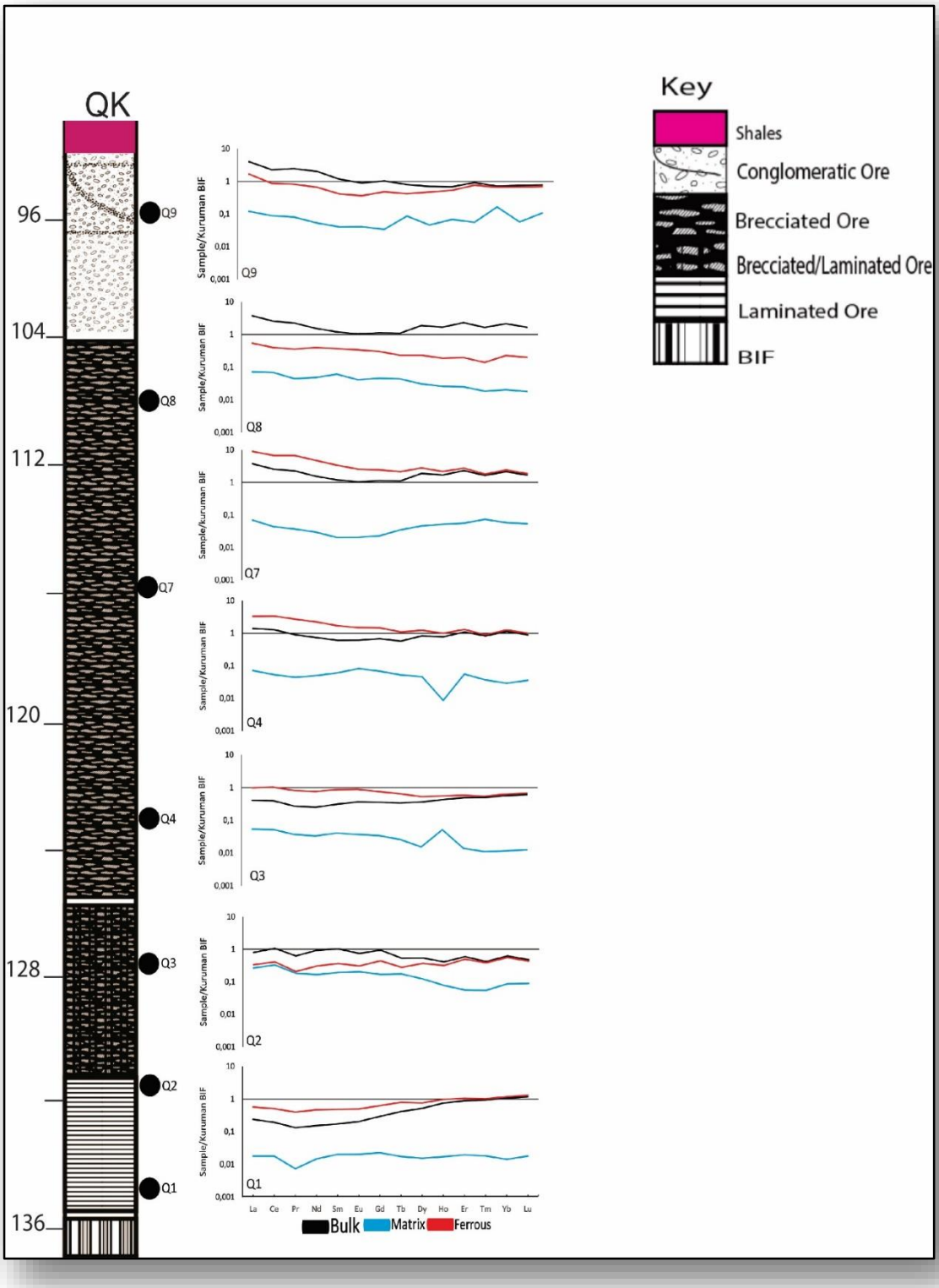

Figure 23: Stratigraphic REE variations in core QK (Q samples) normalised against average BIF.

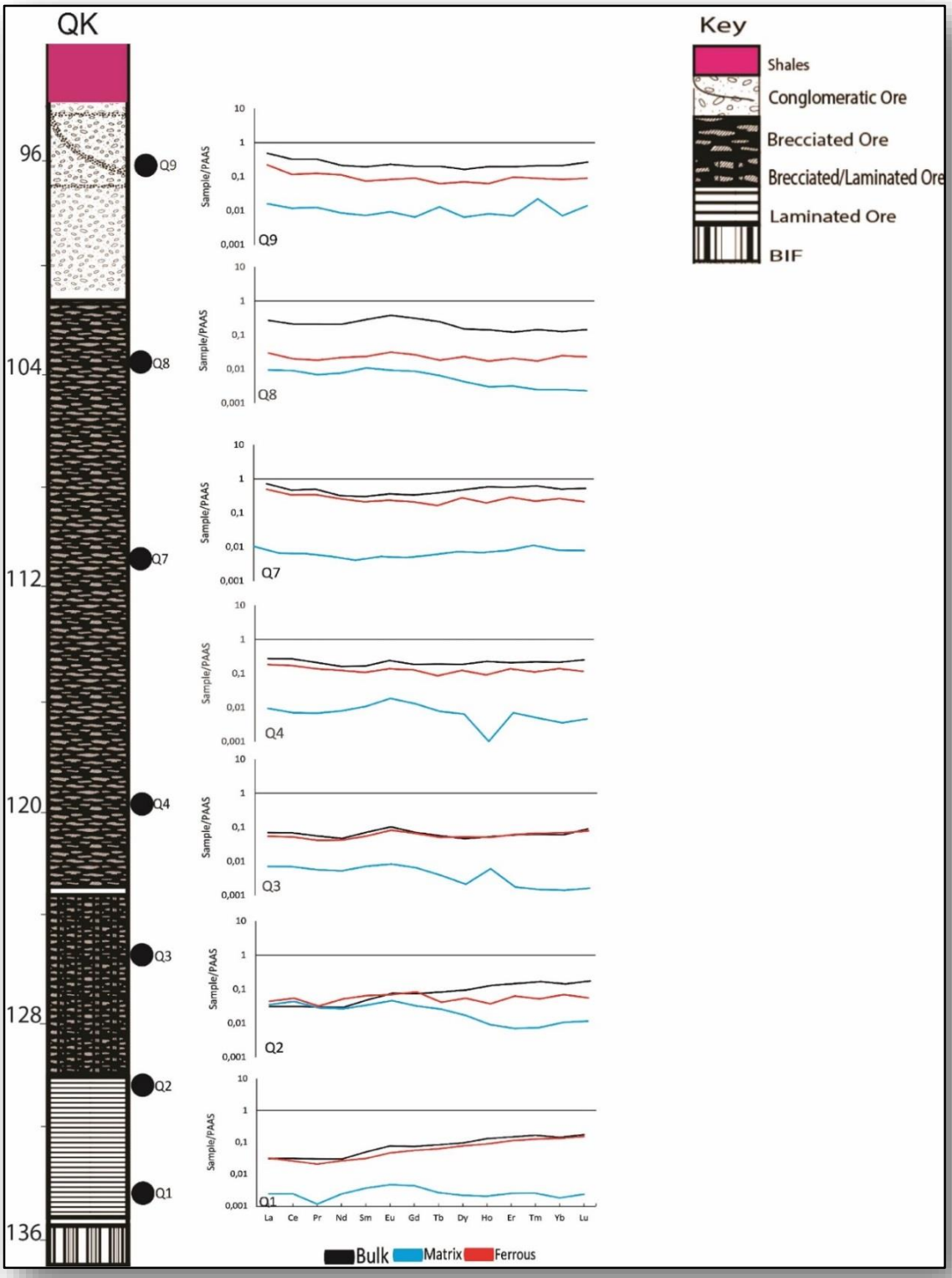

Figure 24: Stratigraphic REE variations in core QK (Q samples) normalised against PAAS.

The PAAS-normalised patterns for intersection QK allow for comparable observations to be made and conclusions drawn. In the upper parts of the intersection dominated by conglomeratic and the breccia ore, the bulk and ferrous fraction patterns appear generally flat and thus average shale-like, and this applies within reason to the matrix REE fractions too. The situation however changes as the more laminated-type ore is approached with depth where the REE patterns for bulk and ferrous fraction samples become positive sloping, especially for samples Q2 and Q1 that capture laminated-style ore. A first inference can therefore be made from Figures 24, and 25, that the REE signal of the iron ore in section QK transitions from generally shale-like to more BIF-like with depth, and as the textures of the ore grade from fragmentary to more laminated.

Drillcore ALK

In contrast to drillcore QK, drillcore ALK captures a relatively more monotonous succession of breccia-style iron ore typical of the ore-type that dominates the King/Khumani area. The added characteristic of the ALK drillcore is that it intersects also apparent gabbroic intrusives from the same area which are not seen in drillcore QK. Drillcore ALK therefore provides an opportunity to observe any variation in REE signature in a texturally more homogeneous ore intersection and also to assess the effect that these intrusions may have had on the REEs.

BIF-normalised REE patterns are shown in Figure 26 just like with all other samples discussed in the previous section for bulk samples and corresponding ferrous and non-ferrous matrix fractions. Again, the bulk patterns and ferrous fractions are in good agreement in terms of absolute REE abundance and pattern geometry, and show abundances similar to the average BIF. Non-ferrous matrix REE patterns also agree with the top five samples but depart from the bulk signal in the bottom three samples where they show characteristic negative slopes. The topmost sample A8 is the only one showing a slightly negative slope and strong positive Ce anomaly. Thereafter, patterns become very similar from sample A7 to and A3 and they show generally flatter patterns and a very small positive Ce anomaly which is followed by a small “sag” in the REE patterns through relatively lower BIF normalised Pr and Nd values, while the remaining pattern is effectively flat. This signal is exemplified best in sample A6 closest to the gabbroic intrusion and appears to peter out in samples further away. The bottom two samples show essentially flat REE patterns.

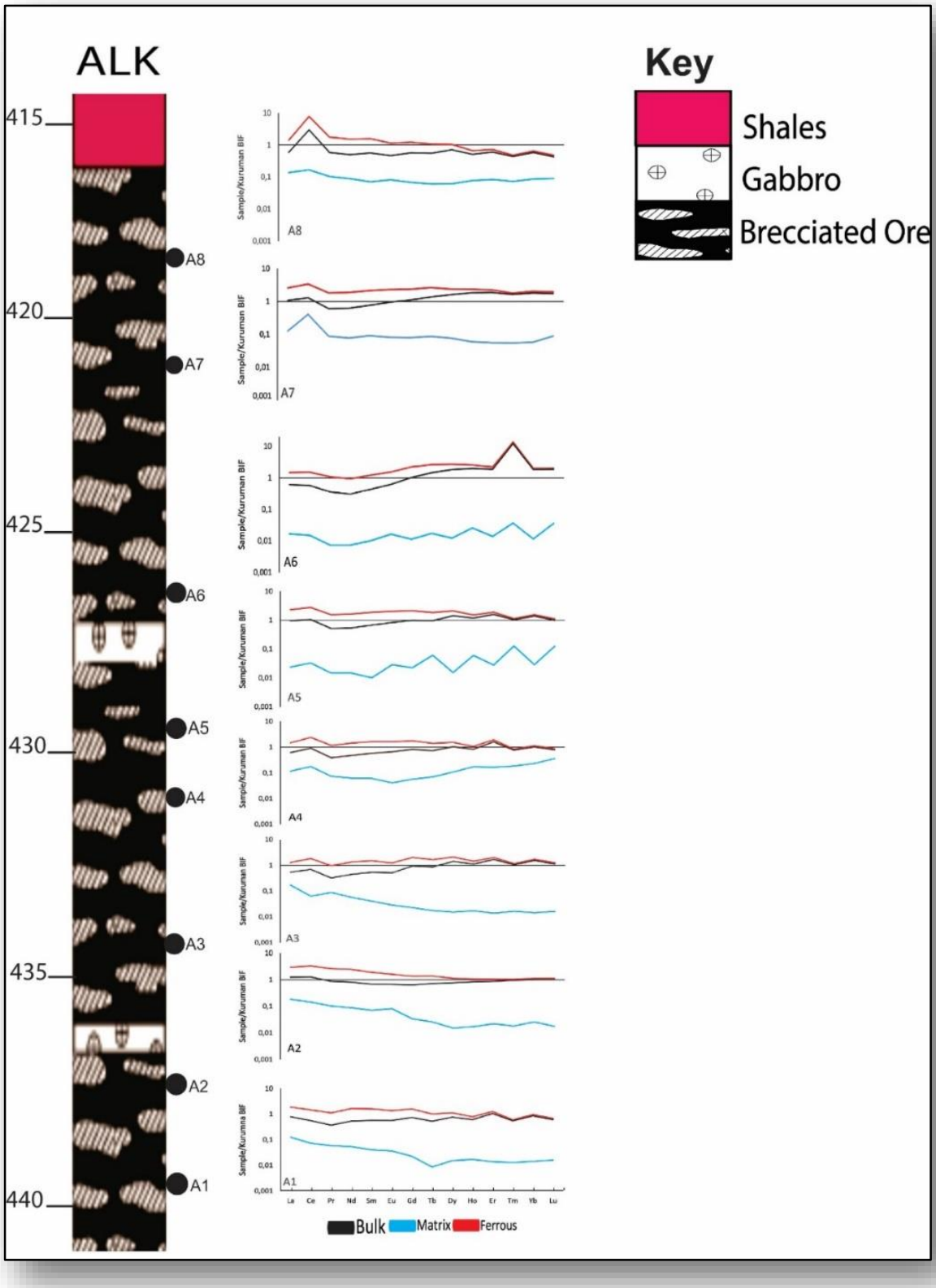

Figure 25: Stratigraphic REE variations across drillcore ALK drill core (A samples) normalised against average BIF.

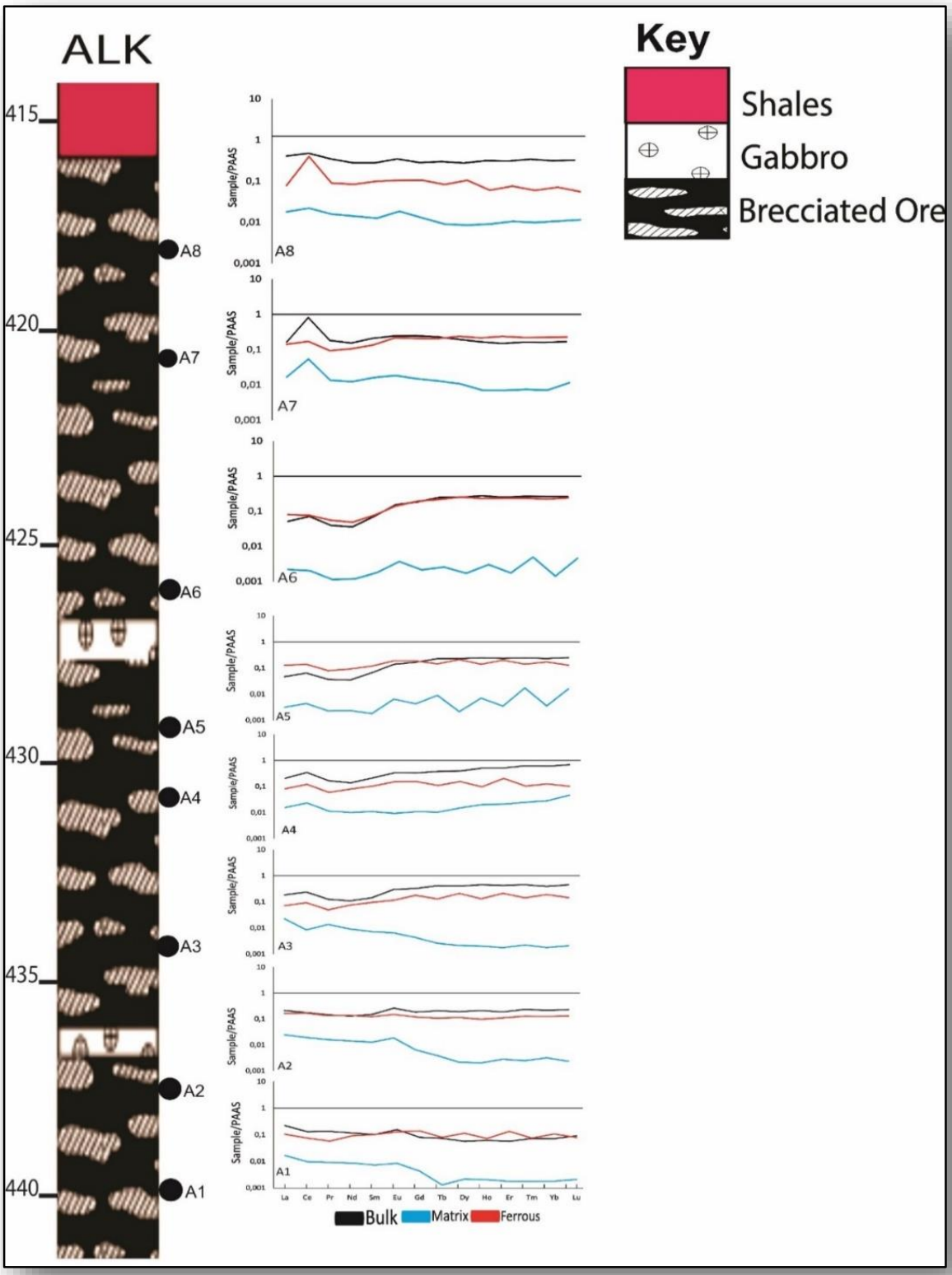

Figure 26: Stratigraphic REE variations across drillcore ALK (A samples) normalised against PAAS .

The PAAS-normalised REE data for drillcore ALK (Figure 26) illustrate more convincingly the change in REE pattern for bulk and ferrous fraction REE from the topmost samples and as the gabbroic intrusion is approached. Samples A8 and A7 at the top of the section show essentially flat, shale-like signals with a strong Ce anomaly at least in sample A8, and then the REE pattern changes strikingly in sample A6 to one of relatively depleted LREE followed by a steep positive slope across the MREE and thereafter flatter pattern for the HREE. The same signature, though more subdued, is seen also in samples A5 to A3, before the REE become flat and thus shale-like again in the bottom two samples A1 and A2. There is therefore an indication that the REE pattern seen in section ALK near the gabbroic dykes, may signify a potential metasomatic effect from the intrusive bodies themselves through preferential LREE depletion.

4.3 Summary of REE results

The key features observed in the examined iron ore samples of this study with respect to their bulk-rock and fraction-specific REE signals are summarised in the following points:

- BIF-normalised and PAAS-normalised bulk REE data reveal significant variations amongst different datasets. Nevertheless, data can be crudely grouped into 3-4 categories according to the overall REE geometry. The majority of samples display negative slopes when normalised against average BIF, and flat patterns when normalised against PAAS, resulting in a predominant shale-like (rather than BIF-like) REE signature.
- REE abundances are generally more enriched relative to average BIF and are controlled by the ferrous fraction. This is a fundamentally important observation which confirms that at least the bulk REE analyses are reflective of the iron component of the ores only, and are not disproportionately influenced by the non-ferrous matrix fraction. Exception to this norm is the high Mn samples from Hotazel, where the matrix can have a considerable influence on the bulk REE signature quantitatively and qualitatively, such as with sample B1.
- Stratigraphically-controlled REE data from drillcore QK show to some degree a general change in the bulk REE signal from relatively more shale-like in the upper, conglomeratic to breccia-style portions of the ores, to relatively more BIF-like in the transtition to more laminated samples lower in the ore intersection. This pattern is reproduced faithfully by the ferrous fraction REE pattern.
- Drillcore ALK captures a texturally more monotonous intersection of breccia-style iron

ore intruded by gabbroic bodies. REE data for bulk-rock and the corresponding ferrous fractions appear shale-like away from the intrusions but they display a pattern near the intrusions of relatively depleted LREE, followed by a steep positive slope across the MREE and then flatter and relatively more enriched HREE. Therefore, the possibility exists that the gabbroic dykes, may have had a localised metasomatic effect through preferential LREE depletion and/or HREE enrichment.

5 Discussion and Conclusions

The common geological factor that unifies the iron ore samples for this study is that they all originate from below the Transvaal-Olifantshoek unconformity (Beukes *et al.*, 2003; Fig. 28). The ore samples are largely of a fragmentary, "breccia" textural style and are therefore

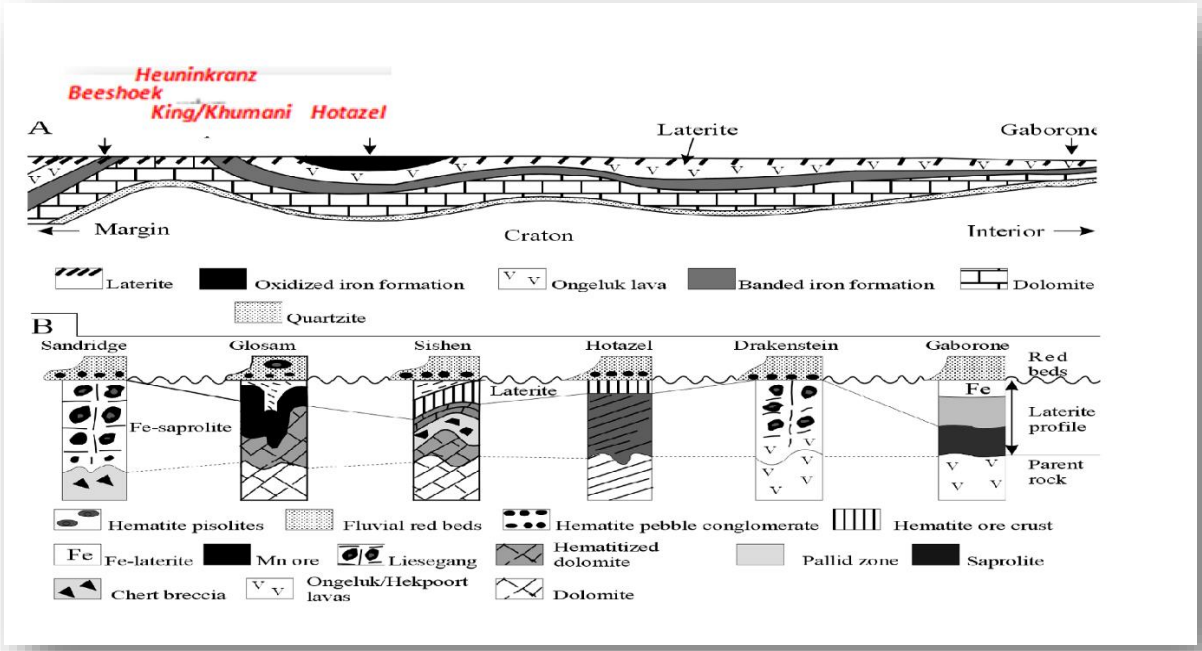

Figure 27: Above, illustration of a "truncation" model of folded Transvaal strata by the lateritised erosion surface on subcontinental scale below the Transvaal-Olifantshoek unconformity. Below, lateral variations along laterite profiles (sourced from Beukes, 2003).

expected to have been highly heterogeneous in their original character, possibly with a significant degree of physical re-working involved. It is for this reason that there is always an inherent factor of bias that is introduced when such samples are selected for analyses, and this must be born in mind for every interpretation and future investigation. For example, it is always uncertain if a thumb-nail sample of breccia-style ore containing a few mm-scale clasts, may have contained originally BIF fragments only, or perhaps particles of other rock material such as shale. This was arguably one of the biggest challenges of this study, namely to constrain the original source of the material that made up these iron ores before the ore-forming alteration event that evidently transformed that material almost completely into massive iron oxide.

5.1 Constraining the protolith/s

The key overarching point to be extracted from the data that were presented earlier in this thesis, is that whereas the ores are dominated by massive hematite apparently replacing fragmentary rock material, the original material itself appears to have had a very strong shale component. The average Kuruman BIF as used based on the unpublished data of Oonk (2017), like every other BIF pretty much (Klein, 2005) is characterised by very low major and trace element values compared to shale for most elements other than Fe and Si (Fig. 29). This shale-like signature of the iron-ores studied here becomes very apparent when one looks particularly at the trace element patterns of the collected ore samples normalised against PAAS and against Kuruman-BIF (Fig. 10 & 11). In these diagrams, it becomes evident that there are trace element abundances that are very atypical of a BIF protolith, as they show relative enrichments of sometimes many orders of magnitude higher as compared to an average BIF. Popular supergene models (Beukes *et al*., 2003) would imply that relatively immobile elements such as HFSEs would be at least residually enriched during supergene iron enrichment, but this cannot have been to the absolute levels that are reported in this thesis. At the same time, when the trace element abundances are normalised against average shale they generally display spidergrams that carry a more shale-like pattern around the constant iron line for PAAS. Although this cannot be used as entirely conclusive evidence that would completely rule out BIF such as the Kuruman iron formation being a key protolith for the iron ores, it makes a point that a shale component is very much evident in these breccia ores and is well-documented geochemically. Therefore, the author finds it difficult to explain the iron ore genesis without taking considerable account of a shale component – other than the postulated BIF – being implicated in the original pre-ore material.

The shale material that is most likely to have been involved as primary component for the iron ores of this study is thought here to have been derived from the Gamagara/Mapedi sequence of the basal Olifantshoek Supergroup overlying the Transvaal Supergroup rocks (Fig. 27). Recent studies that were undertaken by Land *at al.* (2017) have shown that the Mapedi shales are typical ferruginous shales which show localised enrichments in HFSE such as Ti, Nb, Zr and Y hosted in disseminated rutile grains. In Figure 28, an average major element analysis is also shown for the Mapedi shales, normalised relative to PAAS. The diagram shows that the Mapedi shales are strongly depleted in CaO and Na_2O and less so in MgO relative to PAAS, and they

are also enriched in total iron oxide and less so in K_2O relative to PAAS.By comparison with

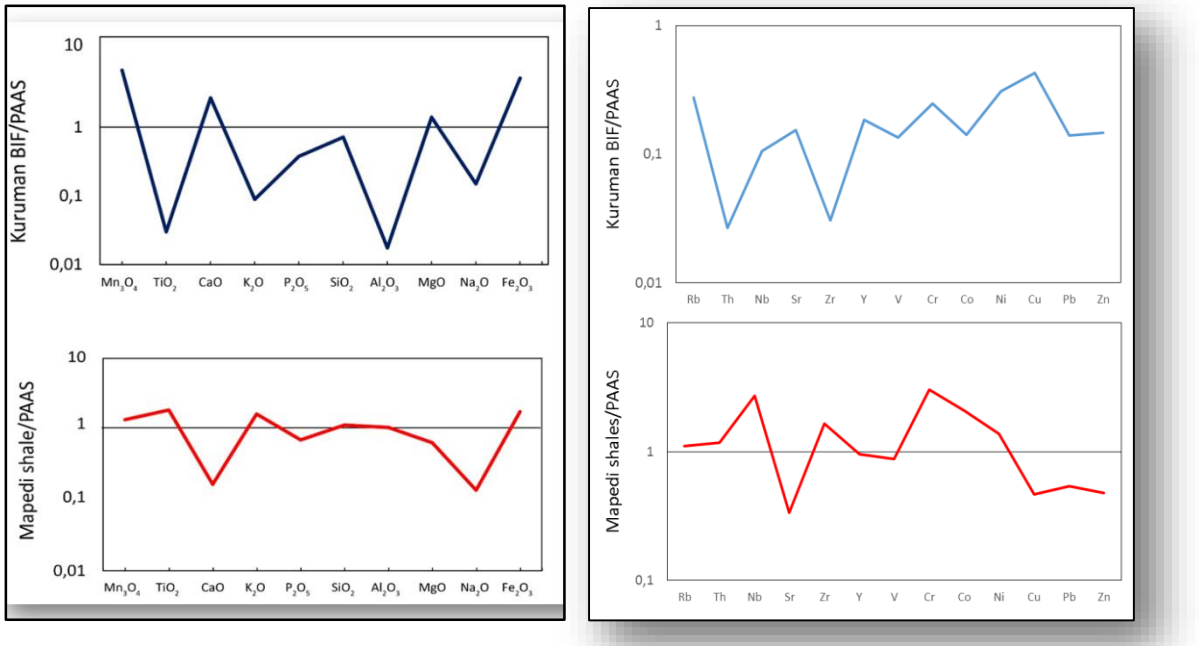

Figure 28: PAAS-normalised major and trace element data for average Kuruman BIF (top) and Mapedi shale (bottom). (Mapedi shale data sourced from Land *et al.*, 2017; Kuruman BIF from Oonk, 2017, unpublished).

the PAAS-normalised geochemistry of most iron ore samples from this study, (Fig. 11, Chapter 2) it becomes apparent that the similarity with the Mapedi shale PAAS-normalised diagram is strong, and this is further supported in terms of trace element abundances. This reaffirms that notion that the Mapedi shales is a probable component for most of the iron ore samples used in this thesis.

The suggestion that there is a strong shale-like bulk geochemical signature in the iron ores of this study is not in itself conclusive of the origin of the ores, and specifically whether: (i) The shale material is residue from a hydrothermal process that replaced BIF and/or shale into iron ore, or (ii) represents mechanically introduced particulate matter of the same provenance as the Mapedi shales into a weathered, fragmentary BIF substrate, that was subsequently converted into iron ore during largely supergene enrichment processes. In other words, one cannot constrain a supergene *versus* hydrothermal origin for the ores independent of the protolith composition. For that reason, the fraction-specific analyses that were employed in this thesis and the results and implications of that approach, are discussed further in the section that follows.

5.2 Evidence from bulk and fraction-specific REE data

The fraction-specific analytical approach employed in this thesis for the first time ever for the iron ores of the Northern Cape Province of South Africa, was undertaken in order to assess the relative geochemical effect of each fraction in the ores across space with emphasis on the behaviour of REE. As indicated in the corresponding Chapter 4 earlier, REE data have been variously used as evidence for an ancient supergene *versus* hydrothermal origin of iron ores worldwide (Fig. 29), therefore they may find important application in the South African ores which are fairly different in terms of their genesis from other BIF-hosted iron ores elsewhere (e.g. Australia) and thus remain quite contentious with regard to their exact origin. One of the key objectives of the fraction-specific application was to try and constrain from the REE whether the non-ferrous matrix of the rocks represented predominantly residual rock material that was not replaced by Fe oxide during the ore-forming process, exotic material introduced during the period of supergene weathering thought to have led to the ore formation, or potentially hydrothermally-derived material. The fact that the amounts of that matrix were always extremely low, very hard to be extracted and analysed, and geochemically very heterogeneous, meant that it was very difficult to obtain very robust and conclusive REE data. At the same time, it was possible to at least look at the matrix data against the bulk REE ones and also those of the extractable Fe-oxide, and draw conclusions in a more comparative manner with respect to how the individual fractions of the ore control REE distribution, and especially whether accessory minerals present in the ores (such as the phosphate phases apatite or monazite) may have had a disproportionate effect on the REE distribution by comparison with their modal abundance.

When the BIF-normalised REE data of the ores are assessed, the first feature that they reveal is that the bulk REE analyses are reflective of the iron component of the ores only, and are not disproportionately influenced by the non-ferrous matrix (see Figures 19 & 20 and 21 & 22, chapter 4). Possible exception to this general norm is the high Mn samples from the Hotazel area, where the matrix occasionally may have a considerable influence on the bulk REE signature, both quantitatively and qualitatively (sample B1). With regard to variations in the overall "geometry" of the REE spidergrams for bulk and ferrous fraction samples, the similarity is striking in the greatest majority of samples whether or not the data are normalised against average BIF or PAAS, This is arguably one of the key outcomes of the fraction-specific geochemical application of this thesis: it confirms that bulk iron ore analyses from at least the

ores from the Northern Cape of South Africa, reflect almost exclusively the iron-oxide fraction of the ores, both quantitatively and qualitatively. Therefore it can be assumed that the REE signal of the hematite (and thus the bulk ore) should reflect the effect of the ore-forming process on the REE of the original material. For example, if the ores have a common hydrothermal origin and the REE are controlled by the hydrothermal fluids, then this should be seen consistently in the ores across space; on the other hand, if the REE are conservatively controlled mainly by the original chemistry of the protolith assemblage that became replaced by Fe oxide, then variations in REE should signify variations in that protolith chemistry.

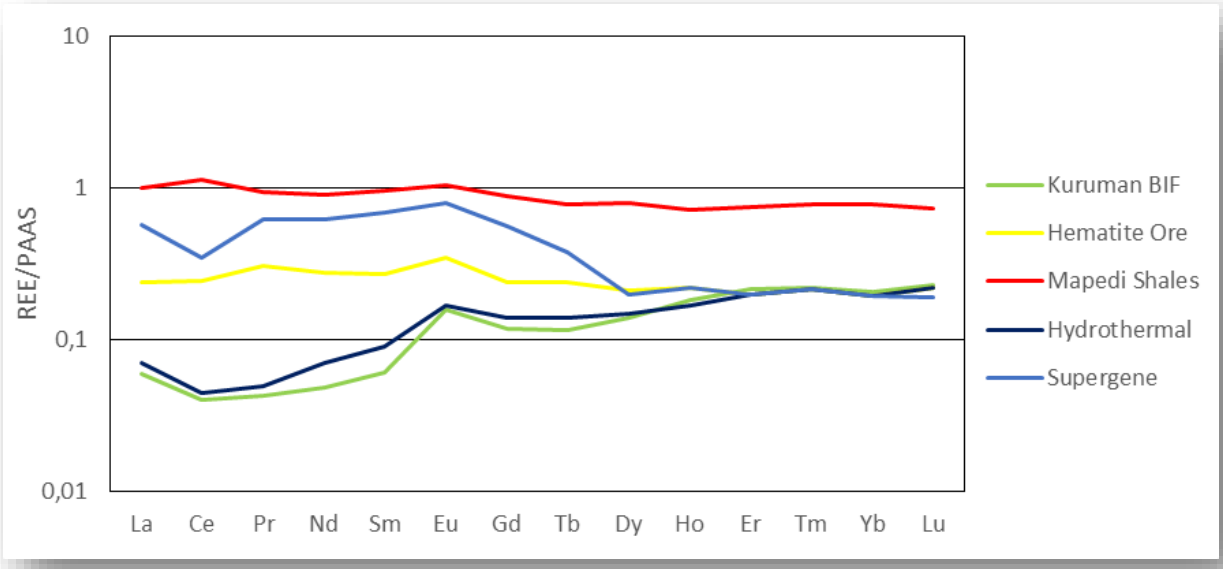

Figure 29: PAAS-normalised REE data for average Kuruman BIF, average hematite ore from this study (n=23, Mn-rich samples excluded), Mapedi shales, average hydrothermal iron ores and average supergene iron ores. Note the striking similarity between the Mapedi REE pattern and that of average Mn-poor iron ores from this study, and that between average hydrothermal ores and average BIF. Mapedi shale data sourced from Land et al., 2017; Kuruman BIF from Oonk, 2017; hydrothermal and supergene iron ore data sourced from Gutzmer *et al*., 2008).

It is clear from the REE results of Chapter 4 that there is no systematic trend to be observed across the different areas of sampling. This is even evident across specific drillcores. For example, drillcore QK (Figs 23a&24) contains textually different types of iron ore stratigraphically, namely conglomeratic ore at the topmost part of the section immediately underlying the Olifantshoek shales, breccia-style ore over most part of the intersection lower, and ultimately more laminated-type ore at the basal part of the ore intersection. Here the non-ferrous matrix REE data appear generally comparable in terms of overall geometry to the bulk

and the ferrous fraction. In the upper parts of the intersection dominated by conglomeratic and the breccia ore, the bulk and ferrous fraction patterns appear generally flat and thus average shale-like, and this applies within reason to the matrix REE fractions too. The situation however changes as the more laminated-type ore is approached with depth where the REE patterns for bulk and ferrous fraction samples become more BIF-like. The inference can therefore be made that the REE data conservatively record a broad transition with depth from a generally more shale-like ore higher in the stratigraphy to more BIF-like with depth, as the textures of the ore grades from fragmentary to more laminated. Considering that the top part of the ore section is located adjacent to the unconformity with the overlying Olifantshoek (Mapedi/Gamagara) shales, it is a reasonable assumption to make that the ore-forming process may have taken place mainly at the expense of shale near the unconformity contact through the action of hydrothermal fluids. This means that it would have post-dated the development of the unconformity itself and the deposition of the shales, and is therefore not consistent with an ancient supergene model preceding shale deposition. Similar conclusions can be drawn from the data of drillcore ALK as well (Figs 25 & 26), although in this instance the presence of gabbroic intrusions seem to have a localised effect on REE behaviour.

5.3 Geochemical evidence for fluid-related enrichments

The lack of any meaningful statistical correlation of a number of trace elements and elemental oxides with bulk Al-oxide provided a first-order evidence for the introduction of these elements into the ores, at least partly, via exotic sources (e.g. hydrothermal fluids). The elements that display such behaviour were recognised to include mainly alkalis/alkali-earths and transition metals such as Co, Ni, Cu, Zn and Pb, which are commonly attributed to metasomatic fluids (Somayajulu *et al.*, 1994). One of the elements of note is Ba: it is known that barite is present widely as veins in the iron ores (ASSMANG, pers. comm.), and it is also reported in massive manganese ores of the Postmasburg Manganese field in the same region. Moore *et al*. (2011) Fairey (2013) and Costin *et al.* (2015), in particular, have reported anomalously high Ba values in such manganese ores from the Kathu-Postmasburg area, and argue for a hydrothermal origin for the Ba and associated alkalis and transition metals. Ba along with other trace elements can be incorporated into Mn-bearing minerals by a series of mechanisms including absorption, adsorption and replacement through ion exchange and co-precipitation with Mn(IV) oxides (e.g. Chen *et al*., 2009b).

The Mn-rich samples (W samples of King/Khumani and Hotazel samples) show very high levels of Ba and conform to the observations of the above authors. However, Ba is also see to be relatively high compared to both average BIF and PAAS for many Mn-poor iron ore samples from this study, especially from King/Khumani ("A" samples) and Beeshoek ("P" & "I" samples). The author therefore believes that there are possibly grounds to explain the enrichments in Ba and associated trace elements in iron and in manganese ores of the Kathu-Postmasburg region, through hydrothermal processes. The high-Mn iron ore samples of Hotazel area, however, are perhaps somewhat different to the other samples from the Kathu-Postmasburg region, as they come from the manganiferous BIF sequence of the Hotazel Formation. These samples are also very Ba rich, signifying a hydrothermal introduction of the Ba into the rocks. Hydrothermal models have been proposed for the fluid alteration history of the manganiferous Hotazel Formation (Gutzmer and Beukes 1996), but these models do not explicitly explain the origin of the Ba. The author believes that there may be a possibility for a common hydrothermal origin of the Ba and other alkalis in the Hotazel ores and the other iron ores regionally as studied here, which should be explored further in the future.

5.4 Conclusions and future work

The results of this study have provided some important new information concerning the genesis of the iron ores in the Transvaal Supergroup. The focus was placed on the geochemical characteristics of the ores from different localities regionally in the Northern Cape Province. The first information obtained from the bulk geochemical analyses of the ores is that there is a strong signal that shale-derived material must have made up an important part of these ores prior to the ore-forming event, and it is the author's opinion that the ore is therefore in large part epigenetic in origin and post-dates the deposition of the Olifantshoek Supergroup. It was also suggested in this thesis that it was specifically the Mapedi shales that formed a strong primary detrital component of the original material that was "ferruginised" (i.e. replaced by Fe oxide) during the ore forming processes, and therefore imparts the shale-like geochemical signature through the geochemistry of the ore. This contention places into question the ancient supergene model as reported by Beukes *et al.*(2003) as the latter fails to provide reasonable explanation for the overwhelming evidence of a shale component in the ores as shown in this thesis.

Whereas the largest part of the data suggest that the Mapedi shale of the Olifantshoek Supergroup appears to be a significant protolith component for the ores, the samples from the

Hotazel area seem to be an exception to this. In general, the Hotazel samples and also selected samples from King/Khumani area are Mn-rich, and they also seem to be enriched in a suite of other alkali elements as well as transition metals, such as Ba, Sr, Rb, Mo, Co, Ni, Zn and Pb. Many of these elements appear to be relatively enriched in Mn-poor iron-ore samples too, suggesting a possible common origin for them in both the Mn-poor and Mn-rich portions of the ores by metasomatic fluids. The scale of this process resulting in these enrichments is difficult to constrain, but it could be regional if all selected ore materials across space (i.e. from Hotazel to Beeshoek) share a common fluid source.

The fraction-specific geochemical application employed in this thesis for the first time ever in the context of these iron ores, focused on the controls of rare earth element (REE) abundance and distribution and its implications. It was found that it was practically very difficult to separate, collect, and analyse the non-ferrous matrix fraction of the ores because of its very low concentrations. Therefore, even though both the dominant ferrous and the minor non-ferrous matrix fractions were measured, the data for the latter are not the most robust for safe interpretation. Nevertheless, the REE signatures have shown that the bulk and the ferrous fractions are consistently very similar qualitatively and quantitatively, and there is therefore no disproportional effect of the non-ferrous matrix fraction on the REE distribution and abundance, with possible exception the data from the Hotazel samples. In general, the REE data for the iron oxide fraction (and thus bulk sample) produce dominantly shale-like patterns of flat REE when normalised against PAAS, which contrast strongly with the expected REE patterns of shale-normalised BIF which are typically positive-sloping indicating a seawater origin (Fig. 28). This is a very important outcome because it supports the suggestion that much of the material replaced into iron ore carries a shale-like signature in the REE signal of the bulk hematite itself, and not of the non-ferrous matrix. However, variations in the REE patterns from one sample to the next can be significant, and suggest much more complex REE controls that may involve variable mixtures of ferruginised material (shale *versus* BIF) even within a single drillcore, or localised effects on REEs by gabbroic intrusions.

A thorough understanding of the origin of the high grade iron ores along the Transvaal-Olifantshoek unconformity in the Northern Cape Province of South Africa, is far from achieved and more work still needs to be done to explore and ultimately elucidate the genesis of these ores. The author believes that further work should now be focused on fine-scale micro-analytical studies on the iron-oxide and non-ferrous matrix components of these ores, to interrogate and explore further the fraction-specific results presented here from the different

areas. The author also believes that the application of combined oxygen and iron isotopes from the hematite fraction of the ores may provide additional important new information: the BIF of the Transvaal Supergroup and the Mapedi shales have been studied already using iron isotopes (Yamaguchi and Ohmoto, 2006; Tsikos *et al*., 2010; Oonk, 2017) and show contrasting distinctive signatures. If these isotopes behaved conservatively during the ore-forming process then they may provide additional evidence for or against the supergene and/or hydrothermal models. It is the hope of the author that the findings in this thesis will provide stimulation for further such detailed studies in future.

6 Reference List

Alchin, D., Lickfold, V., Mienie, P. J., Nel, D., & Strydom, M. (2008). An Integrated Exploration Approach to the Sishen South Iron Ore Deposit, Northern Cape Province, South Africa, and its Implication for Developing a Structural and/or Resource Model for These Deposits. *Reviews in Economic Geology 15*, 317-338.

Altermann W. and Siegfried H.P., (1997). Sedimentology and facies development of an Archaean shelf: carbonate platform transition in the Kaapvaal Craton, as deduced from a deep borehole at Kathu, South Africa. *Journal of African Earth Sciences* 24 (3), 391-410.

Angerer, T., Hagemann, S. G., & Danyushevsky, L. V. (2012). Geochemical evolution of the banded iron formation-hosted high-grade iron ore system in the Koolyanobbing Greenstone Belt, Western Australia. *Economic Geology 107*, 599 - 644.

Astrup, J., Hammerbeck, E. C., & van den Berg, H. (1998). Iron in The Mineral Resources of South Africa (M.G.C. Wilson and C.R. Anhaeusser, eds): Handbook. *Council for Geoscience 16*, 402-415.

Bau, M. (1993). Effects of syn-depositional and post-depositional processes on the rare-earth element distribution in Precambrian iron-formations. *European Journal of Mineralogy 5*, 257-267.

Bau, M., & Dulski, P. (1996). Distribution of yttrium and rare-earth elements in the Penge and Kuruman iron-formations, Transvaal Supergroup, South Africa. *Precambrian Research 79*, 37 - 55.

Bau, M., Romer, R. L., Luders, V., & Beukes, N. J. (1999). Pb, O, and C isotopes in silicified Mooidraai dolomite (Transvaal Supergroup, South Africa): implications for the composition of Paleoproterozoic seawater and 'dating' the increase of oxygen in the Precambrian atmosphere. *Earth and Planetary Science Letters 174*, 43-57.

Banwart, S., Davies, S., and Stumm, W., (1989). The role of oxalate in accelerating the reductive dissolution of hematite (α-Fe2O3) by ascorbate. Colloids and Surfaces 39:303 – 309.

Baranov. V., Tanner,S. (1999). A dynamic reaction cell for ICP-MS. Part 1: The rf-field energy contribution in thermodynamics of ion-molecule reactions". *J. Anal. At. Spectrom. 14 (8)* 1133–1142.

Barton, P. (2002). A Biographical Memoir: Harold Lloyd James. *Biographical Memoirs 81*, 19p.

Beckhoff, B., Kanngießer, B., Langhoff, N., Wedell, R., Wolff, H., (2006) *Handbook of Practical X-Ray Fluorescence Analysis Springer*,

Bekker, A., Slack, J. F., Planavsky, N., Krapez, B., Hofmann, A., Konhauser, K. O., & Rouxel, O. J. (2010). Iron Formation: The Sedimentary Product of a Complex Interplay among Mantle, Tectonic, Oceanic, and Biospheric Processes. *Economic Geology 105*, 467-508.

Belousova,E.A., Griffin,W.L.,O'Reiley,S.Y. and Fsher,N.I. (2002): Apatite as an indicator mineral for mineral exploration : trace-element compositions and relationship to host rock type. *Journal of geochemical exploration. 76*,45-69.

Beukes, N. J. (1980). Stratigrafie en litofasies van die Campbellrand-Subgroep van die Proterofitiese Ghaap-Groep, Noord-Kaapland. *Transactions of the Geological Society of South Africa 83*, 141-170.

Beukes, N. J. (1983). Palaeoenvironmental setting of iron-formations in depositional basin of the Transvaal Supergroup, South Africa, in: Iron-formations: Facts and Problems, eds., A.F. Trendall and R.C. Morris. *Developments in Precambrian Geology 6*, 131- 198.

Beukes, N. J. (1984). Sedimentology of the Kuruman and Griquatown Iron-Formations, Transvaal Supergroup, Griqualand West, South Africa. *Precambrian Research 24*, 47-84.

Beukes, N. J. (1986). The Transvaal Sequence in Griqualand West, in: Mineral Deposits of Southern Africa, eds., C.R. Anhaeusser and S. Maske. *Geological Society of South Africa 1*, 819-828.

Beukes, N. J. (1987). Facies relations, depositional environments and diagenesis in a major early proterozoic stromatolitic carbonate platform to basinal sequence, Campbellrand Subgroup, Transvaal Supergroup, Southern Africa. *Sedimentary Geology 54*, 1-46.

Beukes, N. J., & Gutzmer, J. (2008). Origin and Paleoenvironmental Significance of Major Iron Formations at the Archean-Paleoproterozoic Boundary. *Reviews in Economic Geology 15*, 5-47.

Beukes, N.J., and Klein, C., (1990). Geochemistry and sedimentology of a facies transition-from microbanded to granular iron-formation-in the Early Proterozoic Transvaal Supergroup, South Africa: *Prec. Res., 47,* 99-139.

Beukes, N. J., Gutzmer, J., & Mukhopadhyay, J. (2003). The geology and genesis of high-grade hematite iron ore deposits. *Transactions of the Institute of Mining and Metallurgy B - Applied Earth Sciences 112*, B18-B25.

Buhrke, V. E., Jenkins, R., Smith, D. K., (1998). A Practical Guide for the Preparation of Specimens for XRF and XRD Analysis, Wiley.

Button, A. (1976). Iron formations as an end member in carbonate sedimentary cycles in the Transvaal Supergroup, South Africa. *Economic Geology 17*, 193-201.

Calvert, S.E., Pedersen, T.F., (1993). Geochemistry of Recent oxic and anoxic marine sediments: *implications for the geological record.113*,67-88

Carney, M. D., & Mienie, P. J. (2003). A geological comparison of the Sishen and Sishen South (Welgevonden) iron ore deposits, Northern Cape Province, South Africa. *Transactions of the Institute of Mining and Metallurgy B - Applied Earth Sciences 112*, B81 - B88.

Chang, H.-C. and Matijevic, E., (1983). Interactions of metal oxides with chelating agents IV.Dissolution of hematite. *Journal of Colloid and Interface Science, 92*, 479 – 488.

Chen, Y., Pirajno, F., Li, N., Guo, D., Lai, Y., (2009b). Isotope systematics and fluid inclusion studies of the Qiyugou breccia pipe-hosted gold deposit, Qinling Orogen, Henan province, China: implications for ore genesis. *Ore Geology. 35*, 245–261.

Cornell, R.M., Schindler, P.W., (1987). Photochemical dissolution of goethite in acid/oxalate solution. *Clays Clay Miner. 35*, 347–352.

Cornell, R.M. and Schwertmann, U., (2003). The Iron Oxides. 2nd Ed. Weinheim: Wiley-VCH.

Costin, G., Fairey, B., Tsikos, H., Gucsik, A., (2015) Tokyoite, As-rich tokyoite and noelbensonite: new occurrences from the Postmasburg Manganese Field, Northern Cape Province, South Africa. *Canadian Mineralogist 43*, 981-990.

Dalstra, H., & Guedes, S. (2004). Giant hydrothermal hematite deposits with Mg-Fe metasomatism: A comparison of the Carajas, Hamersley, and other ores. *Economic Geology 99*, 1793-1800.

Dalstra, H., & Rosiere, C. A. (2008). Structural controls on the high-grade iron ores hosted by banded iron formations: A global perspective. *Reviews in Economic Geology 15*, 73 - 106.

Dorland, H. (1999). Paleoproterozoic laterite, red beds and ironstone of the Pretoria Group with reference to the history of atmospheric oxygen. MSc Thesis (unpublished), Rand Afrikaans University, Johannesburg.

De Kock, M. O., Evans, D. A., Gutzmer, J., Beukes, N. J., & Dorland, H. C. (2008). Origin and Timing of Banded Iron Formation-Hosted High-Grade Hard Hematite Deposits - A Paleomagnetic Approach. *Reviews in Economic Geology 15*, 49-71.

Deer, W.A., Howie, R.A., and Zussman, J., (1992). An Introduction to the Rock forming minerals. 2nd ed. Longman,Harlow.

Elderfield, H., (1988). The oceanic chemistry of the rare-earth elements. *Philos. Trans. R. Soc.London, A325*, 105-126.

Eriksson, P. G., & Altermann, W. (1998). An overview of the geology of the Transvaal Supergroup dolomites (South Africa). *Environmental Geology 36*, 179-188.

Evans, D. A., Gutzmer, J., Beukes, N. J., & Kirschvink, J. L. (2001). Paleomagnetic constraints on ages of mineralization in the Kalahari Manganese Field, South Africa. *Economic Geology 96*, 621 - 631.

Figueiredo de Silva, R. C., Lobato, L. M., Rosiere, C. A., Zucchetti, M., Hagemann, S., Baars,F. J., Morais, R., & Andrade, I. (2008). Hydrothermal origin for the jaspilite-hosted, giant Serra Norte iron ore deposits in the Carajas mineral province, Para State, Brazil. *Reviews in Economic Geology 15*, 255-290.

Figueiredo de Silva, R. C., Hagemann, S., Lobato, L. M., Rosiere, C. A., Banks, D. A., Davidson, G. J., Vennemann, T., & Hergt, J. (2013). Hydrothermal Fluid Processes and Evolution of the Giant Serra Norte Jaspilite-hosted Iron Ore Deposits, Carajas Mineral Province, Brazil. *Economic Geology 108*, 739 – 779.

Gole, M. J., & Klein, C. (1981). Banded Iron-Formation through much of Precambrian Time.*Journal of Geology* 81, 169-183.

Gorichev, I.G. and Kipriyanov, N.A., (1984). Regular kinetic features of the dissolution of metal oxides in acidic media. *Russian Chemical Reviews*, 53, 1039 – 1061.

Gross, G. A. (1980). A classification of iron formations based on depositional environments. *Canadian Mineralogist 18*, 215-222.

Grobbelaar, W. S., Burger, M. A., Pretorius, A. I., Marais, W., & van Niekerk, I. J. (1995). Stratigraphic and structural setting of the Griqualand West and the Olifantshoek Sequences at Black Rock, Beeshoek and Rooinekke Mines, Griqualand West, South Africa. *Mineralium Deposita 30*, 152-161.

Gruner, J. W. (1922). The Origin of Sedimentary Iron Formations: The Biwabik Formation of the Mesabi Range. *Economic Geology 17*, 418p.

Gruner, J. W. (1924). Contributions to the geology of the Mesabi range with special reference to the magnetites of the iron-bearing formation west of Mesaba. *Minnesota Geological Survey Bulletin 19*, 71p.

Gruner, J. W. (1925). Discovery of Life in the Archean. *Journal of Geology 33*, 151-152.

Gruner, J. W. (1926). The Soudan Formation and a new suggestion as to the origin of the Vermilion ores. *Economic Geology 21*, 629-644.

Greenfield, S. (1994). Inductively coupled plasmas in atomic fluorescence spectrometry. A review. *Journal of Analytical Atomic Spectrometry 9 (5):* 565.

Gruner, J. W. (1930). Hydrothermal oxidation and leaching experiments, their bearing on the origin of Lake Superior hematite-limonite ores. *Economic Geology 25*, 697-719.

Gruner, J. W. (1936). The structure and composition of greenalite. *American Mineralogist 20*, 475-483.

Gruner, J. W. (1937). Composition and structure of stilpnomelane. *American Mineralogist 22*, 885-860.

Gumsley, A.P., Chamberlain, K.R., Bleeker W., Söderlund, U., de Kock, M.O., Larsson E.R. and Bekker, A. (2017). Timing and tempo of the Great Oxidation Event. *PNAS*, doi: 10.1073/pnas.1608824114

Gutzmer, J. (1996). Genesis and alteration of the Kalahari and Postmasburg manganese deposits, Griqualand West, South Africa. Phd thesis (unpublished), University of Johannesburg, Johannesburg.

Gutzmer J. and Beukes N.J., (1996a). Karst-Hosted Fresh-Water Paleoproterozoic Manganese Deposits, Postmasburg, South Africa. *Economic Geology 91*, 1435-1454.

Gutzmer, J., Chisonga, B. C., Beukes, N. J., & Mukhopadhyay, J. (2008). The Geochemistry of Banded Iron Formation-Hosted High-Grade Hematite-Martite Iron Ores. *Reviews in Economic Geology 15*, 157-183.

Hagemann, S., Dalstra, H. I., Hodkiewicz, P., Flis, M., Thorne, W., & McCuaig, C. (2007). Recent Advances in BIF-related Iron Ore Models and Exploration Strategies. *In "Proceedings of Exploration 07: Fifth Decennial International Conference on Mineral Exploration"*, 811-821.

Hagemann, S., Rosiere, C., Gutzmer, J., & Beukes, N. J. (2008). Introduction: Banded Iron Formation-Related High-Grade Iron Ore. *Reviews in Economic Geology 15*, 1-4.

Halbich, I. W., & Altermann, W. (1992). The genesis of BIF in the Transvaal Supergroup, South Africa, in: Source, Transport and Deposition of Metals, eds., M. Pagel and J.L Leroy. Rotterdam. 841p.

Halbich, I. W., Scheepers, R., Lamprecht, D., van Deventer, J. L., & De Kock, N. J. (1993). The Transvaal-Griqualand West banded iron formation: geology, genesis, iron exploitation. *Journal of African Earth Sciences 16*, 63-120.

Horstmann, U. E., & Halbich, I. W. (1995). Chemical composition of banded iron-formations of the Griqualand West Sequence, Northern Cape Province, South Africa, in comparison with other Precambrian iron formations. *Precambrian Research 72*, 109- 145.

Hieftje, G., (1982). Design and Construction of a Low-Flow,Low-Power Torch for Inductively Coupled Plasma Spectrometry.*Applied Spectroscopy 36 (6):* 627–631.

James, H. L. (1954). Sedimentary facies of iron-formation. *Economic Geology 49*, 235-293.

James, H. L. (1955). Zones of regional metamorphism in the Precambrian of northern Michigan. *Geological Survey of America Bulletin 66*, 1455-1488

James, H. L. (1958). Stratigraphy of pre-Keewenawan rocks in parts of northern Michigan.United States Geological Survey Professional Paper 314-C, 27-44.

Jenkins, R., De Vries, J. L., (1975). Practical X-ray Spectrometry,MacMillan, London.

Kesler, S.E., and Ohmoto, H., (2006). Evolution of Early Earth's Atmosphere, Hydrosphere, and Biosphere - Constraints from Ore Deposits. *Geological Society of America Memoir 198*, 257-268.

Klein, C. (2005). Some Precambrian banded iron-formations (BIFs) from around the world: Their age, geologic setting, mineralogy, metamorphism, geochemistry, and origin. *American Mineralogist 90*, 1473-1499.

Lobato, L. M., Figueiredo e Silva, R. C., Hagemann, S., & Thorne, W. (2007). Mineralizing fluid evolution and REE patterns for the hydrothermal Carajas iron ores, Brazil, and for selected Hamersley iron deposits, Australia. *In: 9th Biennial Society for Geology Applied to Mineral Deposits, SGA meeting, Dublin, Ireland*, 1227 - 1230.

Lobato, L. M., Figueiredo e Silva, R. C., Hagemann, S., Thorne, W., & Zuchetti, M. (2008). Hypogene alteration associated with high-grade banded iron formation-related iron ore. *Reviews of Economic Geology 15*, 107-128.

La Berge, G.L. (1966). Altered pyroclastic rocks in South African iron-formations. *Economic Geology* 61, 572-581.

Lascelles, D. F. (2006a). The Genesis of the Hope Downs Iron Ore Deposit, Hamersley Province, Western Australia. *Economic Geology 101*, 1359-1376.

Lascelles, D. F. (2006b). The Mount Gibson Iron Formation-Hosted Magnetite Deposit: Two Distinct Processes for the Origin of High-Grade Iron Ore. *Economic Geology 101*, 651-666.

Lamprecht, D. F., & Halbich, I. W. (1988). A vertical transition from carbonates to banded iron-formation in the Griqualand West Sequence of the Transvaal Supergroup, at Finsch diamond mine, Northern Cape Province. *Abstracts, Geocongress 1988, Geological Society of South Africa*, 783-786.

Land,J.S., Tsikos, H.,Cousin,D.,Luvizotto,G.,and Zack.,T.(2017) Origin of red beds and paleosols in the Palaeoproterozoic Transvaal and Olifansthoek Supergroups of South Africa: provenance versus metasomatic controls. *Geological Journal*, DOI: 10.1002/gj.2885

Lee, S.O., Tran, T., Park, Y.Y., Kim, S.J., Kim, M.J. (2006). Study on the kinetics of iron oxide leaching by oxalic acid. *Int. J. Miner. Process*. *80*, 144–152.

Lee, S.O., Tran, T., Jung, B.H., Kim, S.J., and Kim, M.J. (2007) Dissolution of iron oxide using oxalic acid. *Hydrometallurgy*, *87*, 91-99.

Mehra O. P., & Jackson, M.L. (1960). Iron oxide removal from soils and clays by a Dithionite-citrate system buffered with Sodium bicarbonate. *Clay and minerals 7*,317-327.

Mermet, J. M. (2005). "Is it still possible, necessary and beneficial to perform research in ICP atomic emission spectrometry?". *J. Anal. At. Spectrom. 20: 11–16. Retrieved 2015-08-31*.

Moore, J. M., Tsikos, H., & Polteau, S. (2001). Deconstructing the Transvaal Supergroup, South Africa: Implication for Palaeoproterozoic palaeoclimate models. *Journal of African Earth Sciences 33*, 437-444.

Moore, J. M., Kuhn, B. K., Mark, D. F., & Tsikos, H. (2011). A sugilite-bearing assemblage from the Wolhaarkop breccia, Bruce iron-ore mine, South Africa: Evidence for alkali metasomatism and 40Ar-39Ar dating. *European Journal of Mineralogy 23*, 661-673.

Morey, G. B. (1983). Animikie Basin, Lake Superior Region, U.S.A, in: Iron-formations: Facts and Problems, eds., A.F. Trendall and R.C. Morris. *Developments in Precambrian Geology 6*, 13-67.

Morris, R. C. (2003). Iron ore genesis and post-ore metasomatism at Mount Tom Price. *Transactions of the Institute of Mining and Metallurgy B - Applied Earth Sciences 112*, B56 - B67.

Nagasawa, H., (1970) Rare earth concentrations in zircons apatites and their host dacites and granites: *Earth and Planetary Science Letters, 9*,359-364

Nelson, B. J., Wood, S. A., & Osiensky, J. L. (2003). Partitioning of REE between solution and particulate matter in natural waters: A filtration experiment. *Journal of Solid State Chemistry 171*, 51-56.

Oonk, P.B.H. (2017) Fraction-specific trace element and stable isotope geochemistry across the BIF stratigraphy of the Transvaal Supergroup in Griqualand West, South Africa and

implications for the history of atmospheric oxygen. Unpublished PhD Thesis, Rhodes University, Grahamstown, South Africa.

Panias, D., Taxiarchou, M., Paspaliaris, I., Kontopoulos, A., (1996). Mechanisms of dissolution of iron oxides in aqueous oxalic acid solutions. *Hydrometallurgy 42*, 257 – 265.

Polteau, S., Moore, J. M., & Tsikos, H. (2006). The geology and geochemistry of the Paleoproterozoic Makganyene diamictite. *Precambrian Research 148*, 257-274.

Powell, C. M., Oliver, N. H., Li, Z. X., Martin, D. M., & Ronaszeki, J. (1999). Synorogenic hydrothermal origin for giant Hamersley iron oxide ore bodies. *Geology 27*, 175-179.

Ramanaidou, E. R., & Morris, R. C. (2010). Comparison of supergene mimetic and supergene lateritic iron ore deposits. *Transactions of the Institute of Mining and Metallurgy B - Applied Earth Sciences 119*, B35-B39.

Roy, S., & Venkatesh, A. S. (2009). Mineralogy and geochemistry of banded iron formation and iron ores from eastern India with implications on their genesis. *Journal Earth System Science 118*, 619-641.

Sidhu, P.S., Gilkes, R.J., Cornell, R.M., Posner, A.M., Quirk, J.P., (1981). Dissolution of iron oxides and oxyhydroxides in hydrochloric and perchloric acids. *Clays Clay Miner*.29, 269–276.

Somayajulu , B.L.K., Yadav, D.N., Sarin, M.M ., (1994). Recent sedimentary records from Arabian Sea: *Proceedings of the Indian Academy of Sciences*, *103*(*2*),315-327.

Stumm, W., and Furrer, G., (1987). The dissolution of oxides and aluminium silicates; examples of Surface-coordination-controlled kinetics. In: Stumm, W. (ed.) *Aquatic Surface Chemistry.* New York:John Wiley & Sons. 197 – 219.

Taylor, D. J., Dalstra, H. J., Harding, A. E., Broadbent, G. C., & Barley, M. E. (2001). Genesis of high-grade hematite orebodies of the Hamersley Province, Western Australia. *Economic Geology 96*, 837 – 873

Taylor, S. R., & McLennan, S. M. (1985). The continental crust: Its composition and evolution. Oxford: Blackwell.

Taxiarchou, M., Panias, D., Douni, I., Paspaliaris, I., and Kontopoulos, A., (1997a). Dissolution of hematite in acidic oxalate solutions. *Hydrometallurgy*, *44*, 287 – 299.

Taxiarchou, M., Panias, D., Douni, I., Paspaliaris, I., and Kontopoulos, A., (1997b). Removal of iron from silica sand by leaching with oxalic acid. *Hydrometallurgy*, *46*, 215 – 227.

Thorne, W. S., Hagemann, S., & Barley, M. E. (2004). Petrographic and geochemical evidence for hydrothermal evolution of the North deposit, Mount Tom Price, Western Australia. *Mineralium Deposita 39*, 766-783.

Thorne, W.S., Hagemann, S., Vennemann, T., & Oliver, N. (2009). Oxygen isotope compositions of iron oxides from high-grade BIF-hosted iron ore deposits of the Central Hamersley Province, Western Australia: Constraints on the evolution of hydrothermal fluids. *Economic Geology 104*, 1019 - 1035.

Tsikos, H. (1994). The mineralogy and geochemistry of the Voelwater banded iron-formation, Northern Cape Province: MSc thesis (unpublished), Rhodes University, Grahamstown.

Tsikos, H., & Moore, J. M. (1997). Petrography and Geochemistry of the Paleoproterozoic Hotazel Iron-Formation, Kalahari Manganese Field, South Africa: Implications for Precambrian Manganese Metallogenesis. *Economic Geology 92*, 87-97.

Tsikos, H., Moore, J. M., & Harris, C. (2001). Geochemistry of the Palaeoproterozoic Mooidraai Formation: Fe-rich limestone as end member of iron formation deposition, Kalahari Manganese Field, Transvaal Supergroup, South Africa. *Journal of African Earth Sciences 32*, 19-27.

Tsikos, H., Beukes, N. J., Moore, J. M., & Harris, C. (2003). Deposition, Diagenesis, and Secondary Enrichment of Metals in the Paleoproterozoic Hotazel Iron Formation, Kalahari Manganese Field, South Africa. *Economic Geology 98*, 1449-1462.

Tsikos, H., & Moore, J. M. (2005). Sodic metasomatism in the Palaeoproterozoic Hotazel iron-formation, Transvaal Supergroup, South Africa: implications for fluid-rock interaction in the Kalahari manganese field. *Geofluids 5*, 264-271

Tsikos, H., Matthews, A., Erel, Y., & Moore, J. M. (2010). Iron isotopes constrain biogeochemical redox cycling of iron and manganese in a Palaeoproterozoic stratified basin. *Earth and Planetary Science Letters 298*, 125-134.

Tsolakidou, A., Garrigós J.B., Kilikoglou V. (2002). An assessment of dissolution techniques for the analysis of ceramic samples by plasma spectrometry. *Analytica Chimica Acta*, *474*, 177-188.

UNESCO, (1973). Genesis of Precambrian Iron and Manganese Deposits. Paris: UNESCO

von Plehwe-Leisen, E., & Klemm, D. D. (1995). Geology and ore genesis of the manganese ore deposits of the Postmasburg manganese-field, South Africa. *Mineralium Deposita 30*, 257-267.

Wells, M.A., Gilkes, R.J., and Fitzpatrick, R.W., (2001). Properties and acid dissolution of metalsubstituted hematites. *Clays and Clay Minerals, 49*, 60 – 72.

Yamaguchi, K.E., Ohmoto, H. (2006) Geochemical and isotopic constraints on the origin of Palaeoproterozoic red shales of the Gamagara/Mapedi Formation, Postmasburg Group, South Africa. *South African Journal of Geology 109*, 123-138.

Yip, Y and Sham, W, (2007). "Applications of collision/reaction-cell technology in isotope dilution mass spectrometry". *TrAC Trends in Analytical Chemistry 26 (7):* 727-743.

7 Appendices

7.1 Appendix A

A1. Core logging and sample collection

Samples from King Farm (ALK, QK and WK), Beeshoek (LOI and POI), Hotazel (B1, B2 and N1) and two samples from prospect of Kumba Iron Ore (V1 and HLT1), were used in the study of the iron ore. Only two drill cores were logged in detail (i.e. borehole logs, ALK and QK) as illustrated in Appendix B1. The depth of the drill cores, ALK and QK, are 25.68m and 42.85m respectively. The logging of the core was carried out by visual observation of rock units present, change in colour, textures. These were the main features recorded. A measuring tape was used in order to correctly determine the depth at which recordable features were found and samples were taken. The samples were selected carefully to avoid secondary phases.

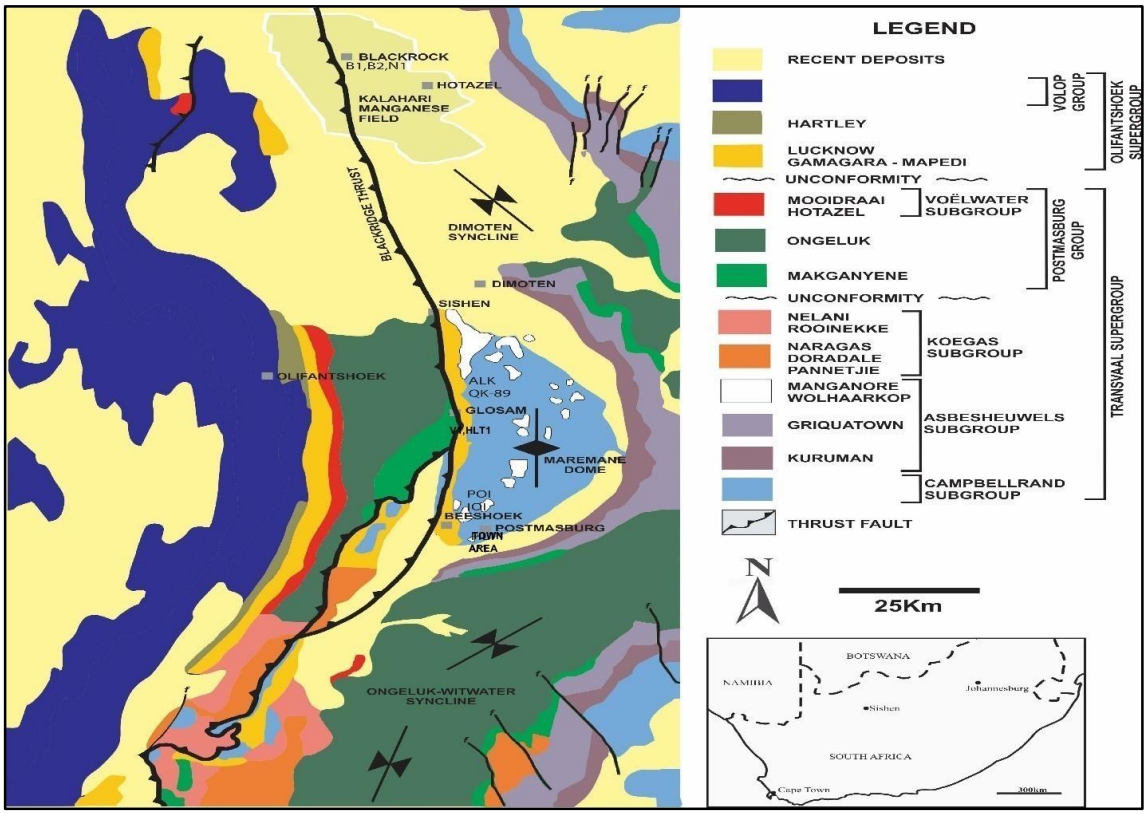

Figure A. Regional geological map of exposures of the Transvaal Supergroup and adjacent basement. These include the Transvaal, Griqualand west and Kanye Basins with the former two separated by the Vryburg Arch. Adapted from (modified courtesy of Assmang, 2005). Location of samples is also shown.

7.2 Appendix B: Results

This appendix contains photographs of representative core samples, schematic illustrations of the logged boreholes used in this study (Figure B1 and B2), as well as tabulated whole-rock geochemical data and fraction-specific data obtained for all samples analysed during this study. Additionally, a table is shown with sample numbers and corresponding stratigraphic depths for all samples analysed for geochemical purposes (Table B1).

Table B1. Sample numbers and the corresponding stratigraphic sample depths (in metres) for all samples selected for geochemical analysis during this study.

A1	439.5	Q1	135.25	I1	307.4	B1	176.02
A2	437.25	Q2	130.2	I2	303	B2	189
A3	434.5	Q3	125	I3	298	N1	90.2
A4	431	Q4	119.65	P1	359	W2	124.5
A5	429.5	Q7	111.25	P2	354.3	W3	120.8
A6	426	Q8	103.85	P3	349.63	W4	113.4
A7	421.25	Q9	96				
A8	417						

B1.B: Representative photographs

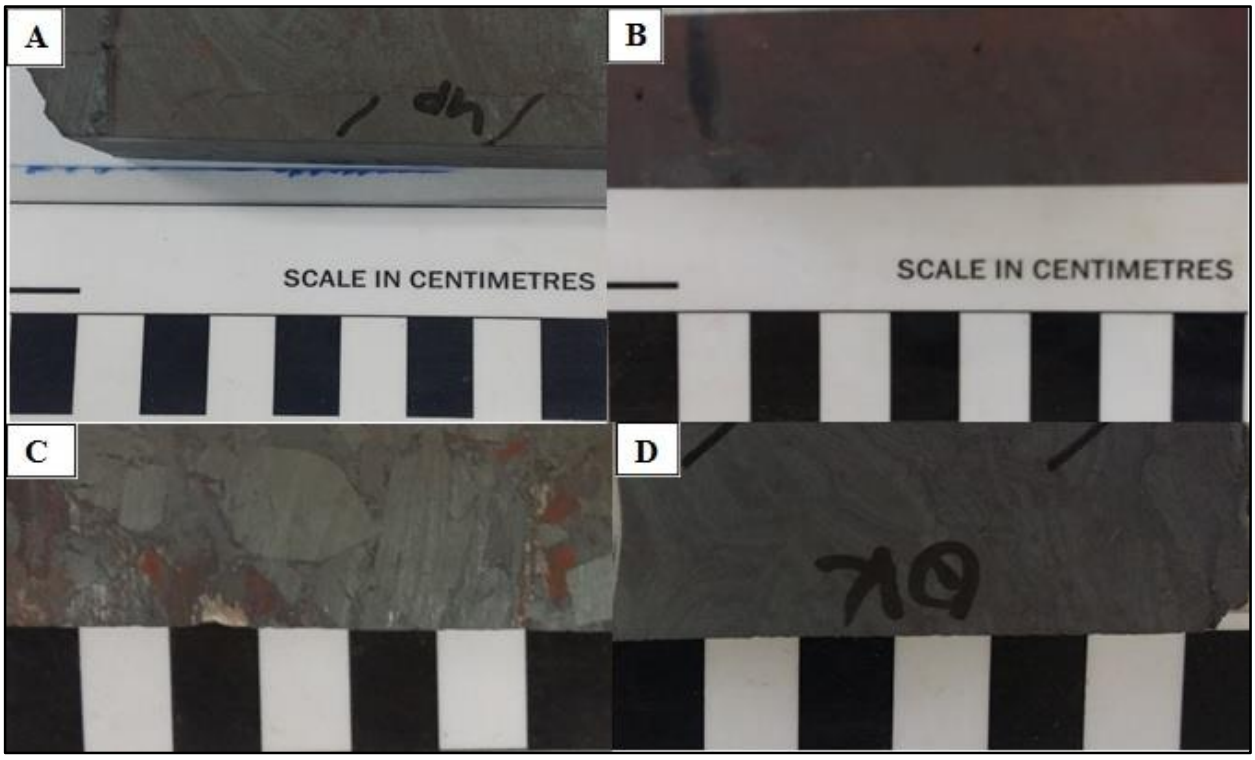

Figure B1.B. Representative core samples of major textural high-grade iron-ore types investigated during this study. A. Brecciated iron ore (hematite clasts in an iron-rich silicate matrix). B. Massive iron ore. C. Conglomeratic iron ore. D. Laminated iron ore.

B2: logged boreholes

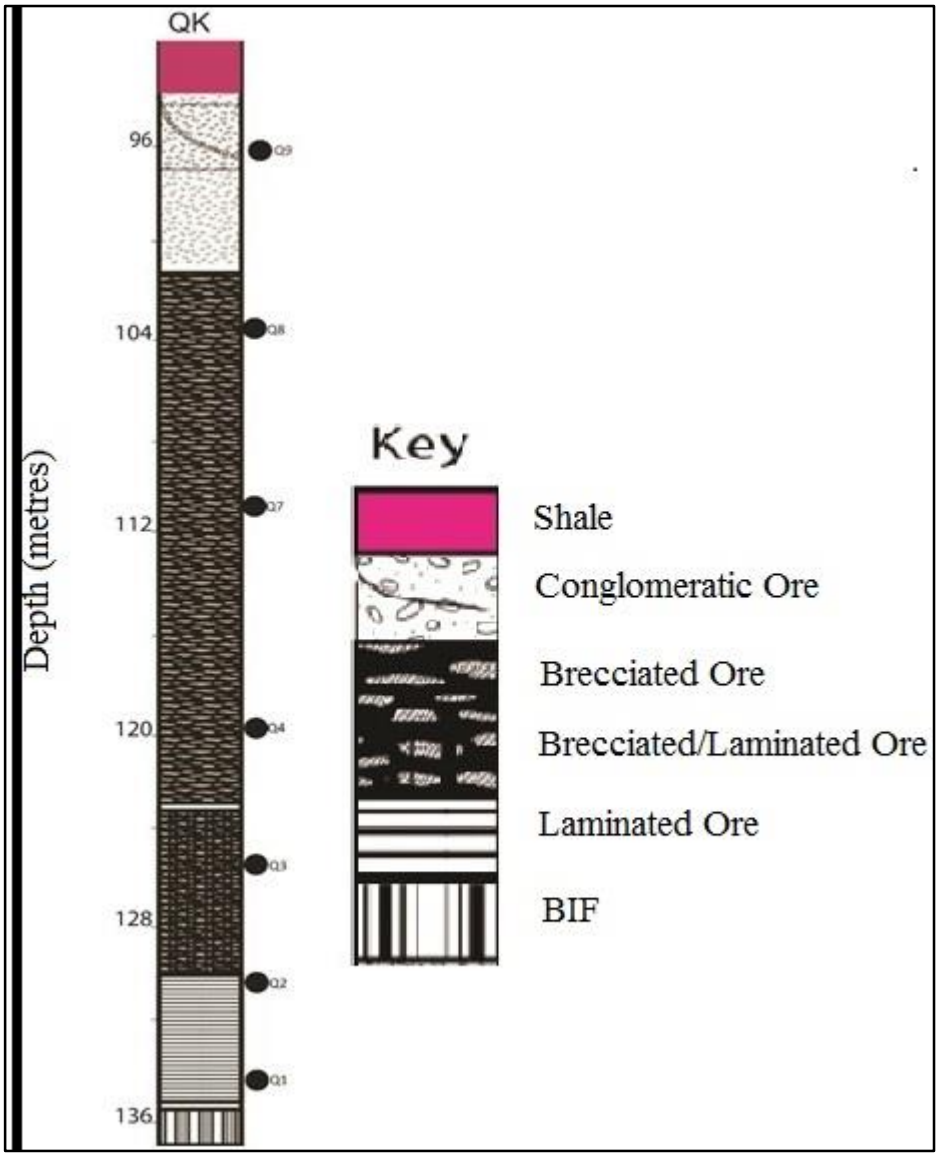

Figure B2.A: Stratigraphic location for samples selected for this study from drillcore QK4_89 (quoted as "QK" in this thesis for simplicity).

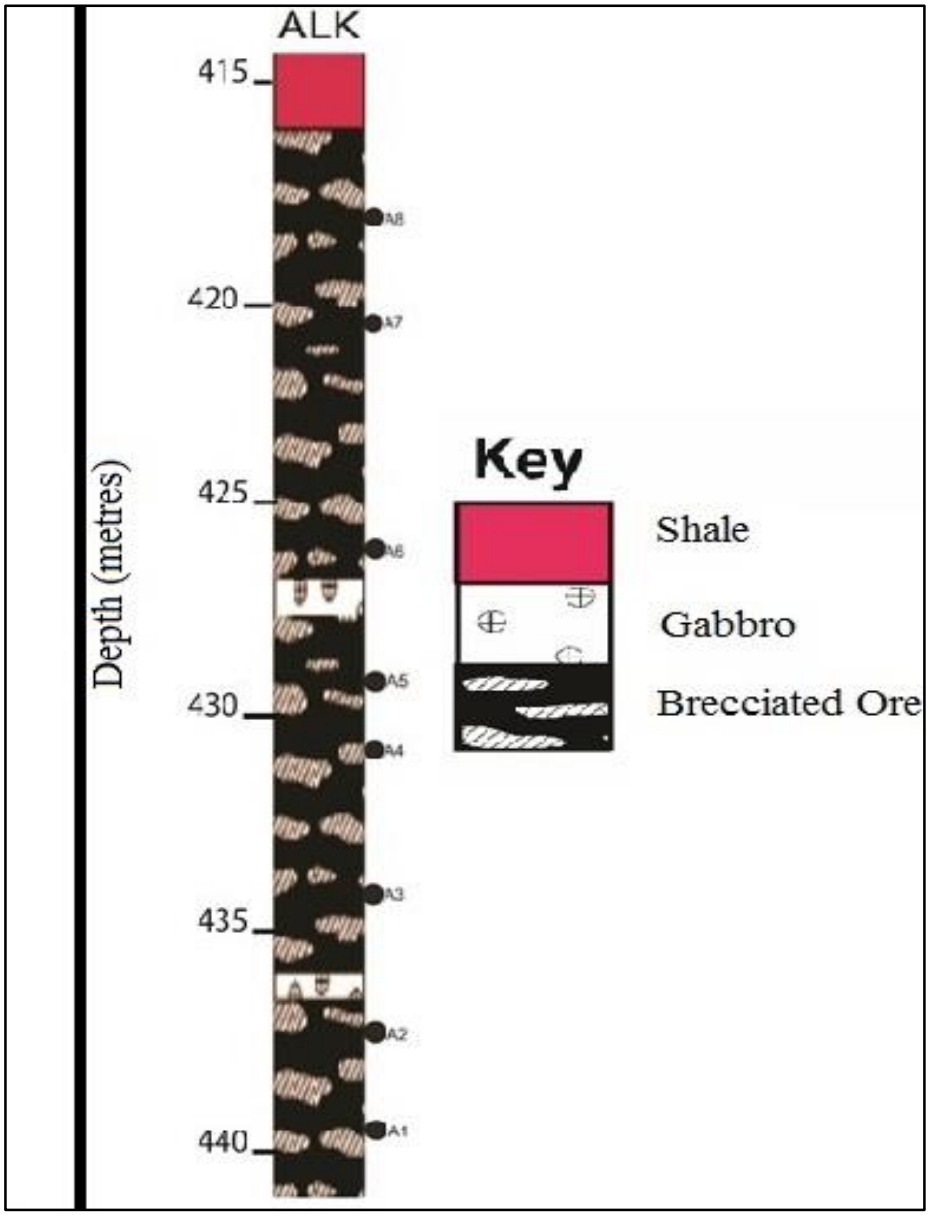

Figure B2.B: Stratigraphic locations for samples selected for this study from drillcore ALK22 (quoted as “ALK” in the thesis for simplicity).

B3: Bulk Major, trace (and rare earth elements) element geochemical data

Appendix B3 contains raw tabulated whole-rock geochemical data for all samples analysed in this study. Major element data are expressed as vlues in weight percent (wt.%) whereas the trace element data are presented in parts per million (ppm). The analytical totals have been calculated by adding up the major element concentrations.

B3.A Major Oxides

Sample	Fe_2O_3	Mn_3O_4	TiO_2	CaO	K_2O	P_2O_5	SiO_2	Al_2O_3	MgO	Na_2O	LOI	Total
Q1	98,82	0,03	0,01	bd	0,13	0,01	1,10	0,60	0,03	bd	0,24	100,97
Q2	98,94	0,05	0,03	bd	0,12	0,04	0,89	0,69	bd	0,01	0,20	100,97
Q3	99,53	0,05	0,01	bd	0,05	0,02	0,71	0,32	bd	0,01	0,18	100,88
Q4	96,26	0,03	0,08	0,01	0,20	0,04	2,05	1,34	bd	bd	0,43	100,45
Q7	93,81	0,02	0,25	0,01	0,38	0,08	3,18	2,20	bd	0,02	0,65	100,59
Q8	95,69	0,03	0,06	bd	0,13	0,05	2,33	1,90	bd	0,01	0,68	100,88
Q9	95,06	0,02	0,18	bd	0,30	0,05	2,75	1,78	0,01	bd	0,53	100,68
A1	98,53	0,03	0,03	0,08	0,04	0,08	0,86	0,95	bd	bd	0,11	100,71
A2	98,28	0,03	0,05	0,10	0,06	0,10	0,79	1,04	bd	bd	0,13	100,58
A3	98,31	0,04	0,04	0,14	0,05	0,12	0,77	0,95	bd	bd	0,15	100,57
A4	88,93	0,04	0,26	0,17	0,91	0,14	5,12	4,11	bd	0,05	0,56	100,29
A5	98,44	0,05	0,04	0,13	0,09	0,11	0,74	1,04	bd	0,02	0,26	100,92
A6	98,48	0,05	0,03	0,13	0,09	0,11	0,77	1,02	bd	0,01	0,19	100,88
A7	81,88	0,04	0,13	0,01	1,60	0,07	7,83	7,06	bd	0,07	1,09	99,78
A8	84,06	0,04	0,27	0,14	1,25	0,15	7,34	5,95	bd	0,16	0,92	100,28
W2	85,29	6,67	0,04	1,80	0,04	0,22	3,08	0,87	0,07	0,02	0,88	98,99
W3	84,33	4,42	0,13	0,83	0,72	0,13	5,22	2,81	0,15	0,04	1,06	99,84
W4	92,89	3,06	0,07	0,19	0,19	0,09	1,66	1,05	0,03	0,03	0,65	99,91
P1	98,69	0,03	0,06	0,01	bd	0,09	0,88	0,67	bd	bd	0,25	100,68
P2	95,49	0,03	0,09	0,04	bd	0,15	2,82	1,52	bd	0,01	0,46	100,61
P3	85,20	0,02	0,30	0,10	0,01	0,26	7,27	5,59	bd	0,02	1,42	100,18
I1	98,04	0,03	0,04	0,05	bd	0,12	1,31	0,87	bd	bd	0,45	100,91
I2	98,91	0,03	0,02	0,03	bd	0,09	0,79	0,43	bd	bd	0,30	100,60
I3	98,94	0,02	0,04	0,01	bd	0,05	0,84	0,56	bd	bd	0,35	100,81
B1	72,77	15,58	0,01	1,49	bd	0,06	4,27	0,27	0,12	0,01	2,75	97,34
B2	26,45	44,01	0,02	11,08	bd	0,04	2,71	0,23	0,06	0,23	4,09	88,92
N1	76,48	13,98	0,01	0,34	bd	0,11	4,72	0,26	0,06	0,01	1,13	97,09
HLT1	96,88	0,05	0,10	0,01	0,12	0,05	1,65	1,56	bd	0,01	0,59	101,02
V1	96,85	0,02	0,06	0,30	0,14	0,21	1,43	1,25	bd	0,01	0,55	100,83

B3.B Trace elements

Sample	Sc	V	Cr	Co	Ni	Cu	Zn	Rb	Sr	Y	Zr	Nb	Mo	Ba	Sm	Ho	Hf	Pb	Ta	Th	U
Q1	0,59	17,71	12,93	1,35	9,05	6,51	23,05	1,78	9,69	5,12	2,15	0,16	2,74	10,98	0,27	0,13	0,02	0,87	0,01	0,08	0,21
Q2	1,01	26,90	16,93	2,69	11,88	7,56	24,85	1,42	44,74	2,72	6,19	0,57	4,84	13,89	0,77	0,08	0,13	1,94	0,03	0,48	0,53
Q3	0,62	15,74	14,40	1,34	9,25	11,81	1,94	0,84	24,02	1,86	3,01	0,61	2,80	10,60	0,40	0,05	0,08	1,68	0,02	0,50	0,31
Q4	3,23	36,84	33,61	3,61	15,93	81,33	32,40	3,39	87,63	6,82	16,72	1,14	6,17	24,67	0,91	0,22	0,43	4,80	0,10	1,55	0,89
Q7	8,10	55,25	60,16	4,23	14,34	6,28	4,97	6,46	215,61	17,54	48,71	3,40	4,46	44,60	1,68	0,58	1,31	11,51	0,32	5,72	1,22
Q8	3,24	45,92	35,28	2,77	13,78	56,14	24,31	2,19	89,01	3,73	16,68	0,94	4,98	23,56	1,59	0,14	0,43	4,36	0,08	1,49	0,73
Q9	5,56	48,75	54,14	3,87	19,86	18,03	5,10	5,07	173,35	5,23	31,48	2,62	3,95	36,95	1,08	0,20	0,78	8,69	0,21	3,93	1,10
A1	1,26	18,50	14,16	0,94	6,95	53,28	29,70	0,83	5,96	1,82	6,85	0,55	1,52	64,68	0,56	0,06	0,16	0,65	0,04	0,53	0,16
A2	2,68	21,97	15,92	1,18	7,54	64,45	33,80	0,91	10,03	6,57	7,91	0,71	1,89	5,12	0,82	0,21	0,20	1,22	0,06	0,64	0,20
A3	3,14	27,08	18,13	0,57	10,14	8,18	4,04	0,76	13,79	15,38	8,45	0,57	1,60	138,45	0,80	0,44	0,20	2,55	0,04	0,76	0,32
A4	9,99	78,96	73,51	1,51	20,96	14,77	9,42	11,15	44,77	14,88	252,52	3,77	2,60	71,71	1,17	0,50	6,21	3,57	0,34	4,90	1,46
A5	3,78	27,02	15,25	0,66	10,73	13,03	8,39	0,93	9,09	8,27	8,09	0,53	1,53	225,40	0,37	0,24	0,18	3,02	0,04	0,58	0,32
A6	4,24	29,96	17,46	0,58	11,34	4,28	5,89	1,03	10,20	9,05	9,13	0,59	1,73	253,09	0,40	0,27	0,21	3,23	0,04	0,65	0,35
A7	18,46	502,45	46,46	2,34	20,58	27,32	19,85	30,33	334,71	4,21	79,22	1,83	3,75	45,52	1,17	0,17	1,77	36,43	0,18	3,15	2,82
A8	12,19	179,04	48,98	1,88	18,29	15,74	19,07	23,15	364,30	8,60	78,40	4,36	2,71	62,91	1,54	0,31	2,06	14,47	0,41	5,46	1,38
W2	1,21	104,58	46,04	41,38	81,87	37,11	22,51	1,71	89,07	8,63	5,10	0,42	4,16	1910,95	1,19	0,24	0,14	157,85	0,05	0,66	0,81
W3	3,01	35,49	85,50	51,25	111,84	41,43	23,72	17,22	107,46	12,89	22,27	1,75	3,08	4694,31	1,63	0,38	0,66	167,96	0,20	2,98	0,81
W4	1,39	28,04	93,57	41,11	89,66	6,67	12,65	4,89	59,49	3,83	7,97	0,84	2,15	543,44	0,62	0,11	0,23	93,07	0,07	0,96	0,23
P1	0,53	20,61	15,83	0,62	10,55	4,02	1,60	0,16	153,31	0,58	3,44	0,27	1,51	12,36	0,42	0,03	0,09	3,24	0,02	0,20	0,11
P2	2,47	41,69	36,55	1,97	23,91	64,01	26,61	0,31	352,74	1,87	13,61	1,00	2,35	67,09	0,34	0,09	0,34	4,04	0,09	1,31	0,32
P3	12,07	111,91	95,04	3,74	69,78	26,07	7,18	0,43	658,63	8,85	74,29	4,19	3,41	124,07	1,62	0,40	1,98	12,32	0,38	6,29	1,72
I1	3,19	45,36	20,67	2,70	17,43	17,32	3,98	0,23	297,43	2,50	10,08	0,75	3,53	30,03	0,99	0,10	0,16	4,61	0,05	0,67	0,26
I2	2,34	30,16	10,50	2,09	16,80	11,66	24,23	0,18	80,01	1,01	3,56	0,23	1,23	17,73	0,28	0,04	0,06	3,67	0,02	0,16	0,12
I3	2,94	42,74	25,13	3,47	19,34	19,74	4,26	0,13	60,34	1,96	6,67	0,71	1,23	15,91	0,22	0,07	0,17	1,54	0,06	0,88	0,19
B1	2,56	33,96	34,71	66,72	31,33	17,76	27,33	0,44	351,79	58,88	8,50	0,58	5,77	383,54	5,10	2,25	0,12	27,51	0,04	0,55	0,82
B2	0,94	34,33	17,85	134,19	25,45	1421,10	37,27	0,06	260,75	11,20	7,19	0,78	10,82	170,25	0,65	0,25	0,10	262,72	0,07	0,82	0,42
N1	3,295	39,57	49,47	71,53	40,32	59,065	79,38	0,483	365,675	34,94	8,995	0,50	5,51	1677,6	30,975	6,59	0,0875	0,0238	15,81	0,341	1,68
HLT1	6,83	224,24	37,84	2,56	18,14	16,98	5,09	3,24	83,98	9,29	15,91	1,39	4,84	61,28	5,07	0,46	0,42	21,58	0,08	1,59	1,99
V1	3,76	73,36	25,82	2,35	19,24	54,67	12,71	3,90	10,81	5,12	10,92	0,86	3,70	14,71	0,95	0,22	0,29	6,72	0,07	1,09	0,51

B3.C Rare earth elements

Sample No.(ppm)	La	Ce	Pr	Nd	Eu	Gd	Tb	Dy	Ho	Er	Tm	Yb	Lu
Q1	1,18	2,48	0,26	1	0,08	0,35	0,06	0,44	0,13	0,42	0,07	0,4	0,07
Q2	6,11	15,09	1,1	3,69	0,22	0,71	0,09	0,39	0,08	0,23	0,04	0,26	0,05
Q3	2,68	5,47	0,49	1,6	0,11	0,33	0,04	0,22	0,05	0,17	0,03	0,17	0,04
Q4	10,51	21,28	1,86	5,49	0,26	0,86	0,15	0,87	0,22	0,59	0,09	0,6	0,11
Q7	27,48	37,47	4,38	10,93	0,39	1,56	0,3	2,23	0,58	1,62	0,25	1,41	0,23
Q8	10,34	16,71	1,86	7,06	0,41	1,44	0,19	0,7	0,14	0,35	0,06	0,36	0,06
Q9	18,52	25,92	2,89	7,25	0,25	0,94	0,15	0,76	0,2	0,56	0,09	0,6	0,11
A1	8,37	10,38	1,18	3,95	0,17	0,37	0,06	0,26	0,06	0,16	0,03	0,2	0,04
A2	8,15	13,83	1,27	4,4	0,28	0,86	0,16	0,9	0,21	0,53	0,09	0,61	0,1
A3	7,01	18,91	1,12	3,71	0,32	1,51	0,32	1,89	0,44	1,21	0,18	1,11	0,19
A4	7,85	27,33	1,45	4,65	0,36	1,54	0,29	1,84	0,5	1,45	0,25	1,7	0,29
A5	1,78	5,09	0,32	1,17	0,15	0,78	0,18	1,07	0,24	0,66	0,1	0,65	0,11
A6	1,97	5,67	0,35	1,22	0,17	0,86	0,19	1,17	0,27	0,72	0,11	0,74	0,11
A7	6,28	64,4	1,61	5,26	0,26	1,15	0,18	0,92	0,17	0,43	0,07	0,46	0,07
A8	15,52	38,03	3,06	9,44	0,37	1,32	0,23	1,29	0,31	0,87	0,14	0,88	0,14
W2	2,47	3,93	0,85	3,87	0,37	1,24	0,2	1,04	0,24	0,6	0,09	0,47	0,07
W3	11,29	16,22	2,78	9,47	0,61	1,63	0,29	1,66	0,38	1	0,16	0,94	0,16
W4	6,87	4,72	1,02	3,26	0,2	0,6	0,1	0,52	0,11	0,29	0,04	0,27	0,04
P1	13,91	7,02	1,77	4,44	0,09	0,25	0,03	0,15	0,03	0,06	0,01	0,08	0,01
P2	2,14	5,87	0,43	1,43	0,1	0,39	0,08	0,45	0,09	0,21	0,03	0,2	0,04
P3	12,23	31,43	2,35	7,47	0,45	1,92	0,35	1,86	0,4	0,97	0,15	0,92	0,16
I1	9,53	21,37	2,02	6,95	0,26	0,86	0,1	0,46	0,1	0,26	0,04	0,31	0,06
I2	3,23	8,39	0,6	1,87	0,08	0,27	0,04	0,19	0,04	0,1	0,02	0,08	0,02
I3	3,91	1,97	0,62	1,8	0,06	0,21	0,04	0,27	0,07	0,21	0,03	0,26	0,05
B1	17,16	9,75	4,8	22,92	1,69	8,03	1,5	9,24	2,25	5,76	0,87	4,75	0,85
B2	6,16	7,41	0,86	3,48	0,18	0,97	0,15	0,89	0,25	0,7	0,12	0,68	0,12
N1	18,88	15,33	7,06	30,98	1,96	7,33	1,22	6,87	1,63	4,2	0,66	4,3	0,76
HLT1	29,53	63,23	6,5	22,72	1,67	6,13	0,85	3,57	0,46	0,64	0,06	0,34	0,06
V1	3,29	5,37	0,74	2,92	0,32	1,23	0,21	1,05	0,22	0,53	0,08	0,43	0,07

B4: Fraction-specific results

Appendix B4 contains raw tabulated fraction-specific geochemical data for all samples analysed in this study. Major element data are expressed as parts per billion (ppb) whereas the rare earth element data are presented in parts per million (ppm). This section also includes the raw data as normalised to 100%. The value of "100" ppb is the detection limit of the technique and not the measured concentration.

B4.A Ferrous fraction analyses - major elements

Sample	Ca	K	Mg	Mn	Na	Al	Fe	P	Ti
Q1	740512	959371	100	100	1415568	2661307	696586131	100	100
Q2	879868	658186	100	100	1016623	2333795	720097529	100	100
Q3	100	525843	100	100	1232360	1207641	651672812	100	100
Q4	100	1219167	100	100	956049	4573139	805674321	100	100
Q7	703888	1441049	100	100	1202327	5897888	717557016	100	1072794
Q8	617653	100	100	100	717001	1342007	386908392	100	100
Q9	700690	534257	100	100	1022654	2232826	839477862	100	792659
A1	4038898	606995	100	100	1662135	5049632	834266263	100	100
A2	861039	100	100	100	1008023	3844349	840153390	100	100
A3	1206427	100	100	100	1649979	4263580	639840730	100	100
A4	1474535	784207	100	100	1135734	4529452	709492927	100	100
A5	0	1081683	100	100	1639629	5365412	694321315	100	1298671
A6	1121495	1194157	100	100	1786675	4771467	666618752	100	100
A7	1925758	2000490	100	100	1597571	7308568	633677432	100	1248474
A8	583706	6619535	100	100	2082720	18050504	654060634	100	695974
W2	5368127	100	100	35983755	647536	3077196	418399546	100	100
W3	5397025	4048569	819206	6390214	3550825	10818055	617934385	100	100
W4	1694173	1281432	100	7164076	1676969	4494939	820795435	100	100
P1	100	100	100	100	939616	2905283	847491197	100	100
P2	547422	100	100	100	1124815	2242013	737859209	100	100
P3	782125	100	100	100	768673	4466865	662160929	100	1075422
B1	13221878	100	574766	164278040	574766	3727475	274964350	100	100
B2	4898984	100	918218	33157667	2044191	3466148	546159360	100	100
N1	2189595	100	100	43863258	2428672	2516190	581776855	100	100
V1	1261783	643822	100	100	909801	4775892	963981033	100	100
HLT1	885068	917341	100	100	1281832	7042690	734354147	100	100

Ferrous-fraction major element analyses normalised to 100% (excluding SiO_2)

Sample	CaO	K_2O	MgO	MnO	Na_2O	Al_2O_3	Fe_2O_3	P_2O_5	TiO_2	Total
Q1	0,10	0,12	bd	bd	0,19	0,50	99,09	bd	bd	100
Q2	0,12	0,08	bd	bd	0,13	0,43	99,24	bd	bd	100
Q3	bd	0,07	bd	bd	0,18	0,24	99,51	bd	bd	100
Q4	bd	0,14	bd	bd	0,11	0,74	99,01	bd	bd	100
Q7	0,09	0,18	bd	bd	0,16	1,07	98,33	bd	0,17	100
Q8	0,16	bd	bd	bd	0,17	0,45	99,22	bd	bd	100
Q9	0,08	0,06	bd	bd	0,11	0,35	99,29	bd	0,11	100
A1	0,47	0,06	bd	bd	0,19	0,79	98,49	bd	bd	100
A2	0,10	bd	bd	bd	0,11	0,60	99,19	bd	bd	100
A3	0,18	bd	bd	bd	0,24	0,87	98,71	bd	bd	100
A4	0,20	0,10	bd	bd	0,15	0,83	98,72	bd	bd	100
A5	bd	0,14	bd	bd	0,22	1,01	98,42	bd	0,21	100
A6	0,16	0,16	bd	bd	0,25	0,93	98,50	bd	bd	100
A7	0,29	0,28	bd	bd	0,23	1,49	97,49	bd	0,22	100
A8	0,08	0,87	bd	bd	0,29	3,47	95,17	bd	0,12	100
W2	1,14	bd	bd	7,05	0,13	0,88	90,79	bd	bd	100
W3	0,81	0,56	0,15	0,89	0,51	2,20	94,88	bd	bd	100
W4	0,20	0,14	bd	0,77	0,19	0,71	98,00	bd	bd	100
P1	bd	bd	bd	bd	0,10	0,45	99,45	bd	bd	100
P2	0,07	bd	bd	bd	0,14	0,40	99,39	bd	bd	100
P3	0,11	bd	bd	bd	0,11	0,88	98,71	bd	0,19	100
B1	2,92	bd	0,15	33,54	0,12	1,11	62,15	bd	bd	100
B2	0,81	bd	0,18	5,09	0,33	0,78	92,81	bd	bd	100
HLT1	0,12	0,11	bd	0,00	0,16	1,25	98,36	bd	bd	100
N1	0,34	0,00	bd	6,30	0,36	0,53	92,47	bd	bd	100
V1	0,13	0,06	bd	bd	0,09	0,65	99,07	bd	bd	100
I1	0,14	bd	bd	bd	0,22	0,71	98,93	bd	bd	100
I2	0,06	bd	bd	bd	0,10	0,29	99,55	bd	bd	100
I3	bd	bd	bd	bd	0,09	0,40	99,51	bd	bd	100

B4.B Non-ferrous fraction analyses - major elements

Sample	Ca	K	Mg	Mn	Na	Al	Fe	P	Ti
Q1	11481	45092	100	100	11315	158470	135496	100	100
Q2	7009	117918	100	100	12661	1361017	368165	7604	100
Q3	6359	34259	5103	100	11319	473440	347584	100	100
Q4	7499	174717	18203	100	20439	1557928	744388	100	100
Q7	5272	107578	100	100	17220	670667	415184	100	7472
Q8	5509	73079	100	100	41913	448596	178207	5117	100
Q9	15643	225939	8522	100	64930	549697	473648	9577	13639
A1	30087	33411	100	100	9875	441346	300952	100	100
A2	24705	42681	100	100	12683	749521	143936	5969	100
A3	14324	26868	100	100	8850	100	100	5855	100
A4	28825	1243134	33862	100	81708	478629	2709543	100	7761
A5	93556	122364	100	100	99947	152042	2732664	100	100
A6	44343	23624	100	5062	26014	100	2828463	100	100
A7	21816	1092142	5781	100	90140	2732664	1919535	21084	100
A8	40440	751827	7246	100	129845	1987770	245699	14535	100
W2	1165426	24130	100	49993	18241	303838	100	10377	100
W3	3063225	160815	18062	47776	31659	492879	287448	100	100
W4	17797	14610	100	100	12437	100	100	100	100
P1	13879	8858	100	100	46545	221401	100	11597	100
P2	22062	5765	100	100	14524	91246	85970	12051	100
P3	74598	38644	100	100	125352	1788342	82378	100	23277
B1	1270522	34565	100	97239	127474	1478317	291654	100	100
B2	419863	8940	100	419863	59641	111947	100	100	100
N1	353220	100	100	90716	14940	173732	1818029	13467	100
V1	208623	47554	100	100	12466	107748	108573	30431	100
HLT1	14686	21949	100	100	15552	772728	271169	6008	100

Non-ferrous fraction analyses normalised to 100%

Sample	CaO	K_2O	MgO	MnO	Na_2O	Al_2O_3	Fe_2O_3	P_2O_5	TiO_2	TOTAL
Q1	2,80	10,16	0,03	0,02	2,66	44,70	39,55	0,04	0,03	100
Q2	0,35	5,36	0,01	bd	0,60	68,55	24,51	0,61	0,01	100
Q3	0,63	3,13	0,60	0,01	1,08	46,55	47,97	0,02	0,01	100
Q4	0,27	5,74	0,77	bd	0,70	56,70	35,81	0,01	bd	100
Q7	0,36	6,80	0,01	0,01	1,14	62,02	29,05	0,01	0,61	100
Q8	0,67	8,21	0,01	0,01	4,92	55,83	29,31	1,02	0,01	100
Q9	1,02	13,63	0,66	0,01	4,09	41,80	36,71	1,03	1,06	100
A1	3,24	3,32	0,01	0,01	1,02	48,58	43,78	0,02	0,01	100
A2	2,36	3,76	0,01	0,01	1,17	73,17	18,57	0,93	0,01	100
A3	24,78	42,90	0,21	0,16	14,75	0,23	0,18	16,59	0,21	100
A4	0,53	21,04	0,74	bd	1,44	67,11	8,97	bd	0,17	100
A5	2,25	2,72	bd	bd	2,32	88,95	3,74	bd	bd	100
A6	1,48	0,73	bd	0,16	0,84	96,77	bd	0,01	bd	100
A7	0,32	14,80	0,10	bd	1,28	54,19	28,80	0,51	bd	100
A8	1,06	18,13	0,22	bd	3,27	70,14	6,56	0,62	bd	100
W2	73,80	1,41	0,01	2,92	1,11	0,01	19,66	1,08	0,01	100
W3	72,94	3,53	0,51	1,05	0,73	9,24	11,99	bd	bd	100
W4	40,46	30,65	0,27	0,21	27,24	0,31	0,23	0,37	0,27	100
P1	4,44	2,62	0,04	0,03	14,35	72,37	bd	6,08	0,04	100
P2	8,10	1,95	0,04	0,03	5,13	45,22	32,24	7,24	0,04	100
P3	2,70	1,29	bd	bd	4,38	87,55	3,05	0,01	1,01	100
B1	37,15	0,93	bd	2,62	3,59	44,17	11,52	bd	bd	100
B2	42,50	0,84	0,01	39,22	5,82	11,58	0,01	0,02	0,01	100
HLT1	1,21	1,67	0,01	0,01	1,23	64,94	30,12	0,81	0,01	100
N1	13,77	bd	bd	3,26	0,56	72,40	9,14	0,86	bd	100
V1	36,53	7,68	0,02	0,02	2,10	25,48	19,42	8,73	0,02	100
I1	1,05	0,71	0,01	bd	2,42	65,43	28,53	1,84	0,01	100
I2	1,01	0,01	0,01	0,01	0,47	75,02	21,56	1,92	0,01	100
I3	1,31	0,45	0,01	0,01	1,06	60,89	34,82	1,43	0,01	100

B4.C Ferrous fraction REE

Sample	La	Ce	Pr	Nd	Sm	Eu	Tb	Gd	Dy	Ho	Er	Tm	Yb	Lu
Q1	1,21	2,05	0,18	0,84	0,17	0,05	0,05	0,26	0,34	0,09	0,32	0,05	0,37	0,07
Q2	1,68	4,34	0,28	1,66	0,36	0,08	0,03	0,39	0,24	0,04	0,18	0,02	0,20	0,02
Q3	2,08	4,17	0,37	1,35	0,31	0,09	0,04	0,31	0,23	0,05	0,18	0,03	0,20	0,03
Q4	7,01	13,60	1,22	3,96	0,60	0,15	0,07	0,60	0,54	0,09	0,39	0,05	0,39	0,05
Q7	18,85	26,93	3,04	8,35	1,18	0,26	0,13	1,00	1,22	0,20	0,83	0,09	0,74	0,09
Q8	1,14	1,60	0,16	0,71	0,13	0,03	0,01	0,12	0,10	0,02	0,06	0,01	0,07	0,01
Q9	8,44	9,22	1,11	3,61	0,41	0,09	0,05	0,43	0,31	0,06	0,28	0,04	0,23	0,04
A1	3,97	5,89	0,51	2,92	0,56	0,14	0,06	0,66	0,50	0,07	0,38	0,03	0,30	0,03
A2	6,27	13,42	1,18	4,39	0,67	0,16	0,08	0,56	0,50	0,10	0,31	0,05	0,35	0,06
A3	2,73	7,37	0,44	2,41	0,53	0,13	0,10	0,83	0,93	0,13	0,60	0,06	0,54	0,06
A4	3,10	9,58	0,52	2,56	0,57	0,16	0,08	0,72	0,68	0,10	0,58	0,04	0,35	0,04
A5	4,88	11,12	0,70	2,92	0,66	0,20	0,11	0,88	0,93	0,14	0,57	0,06	0,48	0,06
A7	5,42	13,68	0,83	3,38	0,75	0,23	0,16	0,98	1,05	0,21	0,68	0,09	0,63	0,10
A8	2,98	31,57	0,79	2,70	0,56	0,11	0,06	0,50	0,46	0,06	0,22	0,02	0,20	0,02
W2	1,25	1,89	0,40	2,04	0,50	0,09	0,10	0,66	0,63	0,13	0,35	0,05	0,29	0,04
W3	34,97	6,36	0,94	5,56	0,00	0,00	0,11	0,94	1,03	0,09	0,66	0,06	0,59	0,07
W4	6,38	4,07	0,88	2,99	0,49	0,12	0,07	0,61	0,51	0,07	0,28	0,03	0,24	0,03
P1	24,85	11,45	2,77	7,46	0,73	0,14	0,06	0,46	0,31	0,06	0,13	0,02	0,17	0,03
P2	5,53	3,32	0,67	2,89	0,33	0,05	0,02	0,22	0,18	0,02	0,08	0,01	0,11	0,01
P3	3,41	7,86	0,62	2,13	0,44	0,12	0,12	0,56	0,94	0,17	0,45	0,06	0,33	0,05
I1	4,50	11,66	0,80	2,78	0,64	0,20	0,17	0,95	1,04	0,22	0,64	0,09	0,61	0,10
I2	1,55	4,14	0,22	1,18	0,18	0,04	0,03	0,21	0,29	0,04	0,17	0,02	0,16	0,02
I3	3,21	1,48	0,48	1,46	0,17	0,05	0,05	0,23	0,36	0,09	0,26	0,04	0,29	0,05
B1	3,15	3,73	0,47	1,56	0,28	0,07	0,06	0,36	0,42	0,11	0,37	0,06	0,46	0,08
B2	10,05	5,20	2,59	12,78	3,10	0,97	0,87	5,42	6,21	1,40	4,20	0,57	3,60	0,60
N1	12,64	8,10	4,33	20,29	4,54	1,27	0,89	6,01	5,80	1,20	3,61	0,54	3,75	0,64
HLT1	15,25	34,76	3,33	12,58	2,78	0,82	0,43	3,30	1,99	0,26	0,43	0,05	0,29	0,06
V1	1,90	2,97	0,39	1,64	0,53	0,17	0,11	0,72	0,66	0,12	0,33	0,04	0,29	0,04

B4.D Non-ferrous fraction REE

Sample	La	Ce	Pr	Nd	Sm	Eu	Tb	Gd	Dy	Ho	Er	Tm	Yb	Lu
Q1	0,091	0,187	0,019	0,078	0,019	0,005	0,005	0,021	0,011	0,001	0,007	0,002	0,005	0,001
Q2	1,369	3,479	0,246	0,904	0,186	0,048	0,017	0,154	0,067	0,004	0,025	0,006	0,029	0,005
Q3	0,275	0,547	0,052	0,179	0,036	0,009	0,003	0,028	0,013	0,003	0,005	0,002	0,004	0,001
Q4	0,235	0,564	0,060	0,271	0,064	0,016	0,006	0,060	0,032	0,004	0,017	0,003	0,012	0,002
Q7	0,348	0,462	0,055	0,160	0,024	0,006	0,004	0,022	0,027	0,001	0,019	0,005	0,022	0,004
Q8	0,358	0,723	0,062	0,258	0,056	0,012	0,005	0,044	0,021	0,004	0,009	0,001	0,008	0,001
Q9	0,609	0,943	0,111	0,293	0,043	0,013	0,011	0,031	0,026	0,005	0,017	0,000	0,022	0,007
A1	0,631	0,772	0,085	0,289	0,040	0,009	0,002	0,022	0,010	0,002	0,005	0,001	0,006	0,001
A2	0,937	1,542	0,137	0,485	0,076	0,017	0,003	0,033	0,014	0,010	0,008	0,001	0,009	0,001
A3	0,861	0,667	0,116	0,313	0,039	0,008	0,003	0,024	0,013	0,010	0,005	0,000	0,005	0,001
A4	0,591	1,857	0,100	0,343	0,056	0,013	0,008	0,052	0,069	0,017	0,061	0,011	0,085	0,015
A5	0,121	0,354	0,024	0,077	0,015	0,008	0,007	0,018	0,014	0,007	0,011	0,007	0,014	0,008
A6	0,084	0,161	0,014	0,048	0,011	0,004	0,003	0,014	0,009	0,007	0,005	0,001	0,005	0,002
A7	0,639	4,329	0,119	0,424	0,086	0,019	0,013	0,074	0,053	0,007	0,019	0,005	0,021	0,005
A8	0,691	1,758	0,143	0,477	0,073	0,016	0,008	0,059	0,044	0,009	0,028	0,002	0,030	0,005
W2	0,223	0,317	0,073	0,353	0,087	0,022	0,015	0,093	0,068	0,016	0,032	0,000	0,023	0,006
W3	0,210	0,271	0,054	0,208	0,031	0,005	0,005	0,029	0,023	0,005	0,012	0,003	0,012	0,003
W4	0,020	0,018	0,004	0,012	0,003	0,001	0,000	0,003	0,001	0,005	0,002	0,001	0,001	0,000
P1	0,778	0,382	0,096	0,256	0,026	0,005	0,002	0,013	0,007	0,005	0,003	0,000	0,002	0,000
P2	1,262	0,604	0,157	0,417	0,038	0,008	0,003	0,022	0,010	0,005	0,001	0,001	0,003	0,001
P3	0,934	2,365	0,179	0,625	0,121	0,030	0,017	0,131	0,089	0,014	0,044	0,007	0,053	0,008
I1	0,763	1,665	0,159	0,585	0,077	0,019	0,006	0,062	0,020	0,004	0,009	0,002	0,012	0,003
I2	0,592	1,250	0,109	0,363	0,056	0,019	0,011	0,055	0,021	0,008	0,010	0,006	0,009	0,007
I3	0,532	0,200	0,060	0,192	0,025	0,005	0,002	0,018	0,013	bd	0,009	0,002	0,015	0,003
B1	0,711	0,389	0,233	1,270	0,237	0,066	0,038	0,335	0,223	0,042	0,100	0,010	0,053	0,008
B2	0,760	0,340	0,190	1,300	0,210	0,100	0,030	0,300	0,260	0,040	0,080	0,010	0,070	0,030
N1	0,632	0,603	0,295	1,488	0,260	0,059	0,026	0,195	0,108	0,023	0,043	0,011	0,039	0,011
HLT1	1,671	3,426	0,371	1,391	0,323	0,100	0,054	0,405	0,232	0,029	0,034	0,009	0,017	0,007
V1	0,260	0,342	0,045	0,206	0,078	0,021	0,011	0,090	0,060	0,010	0,025	0,003	0,018	0,003

7.3 Appendix C:

Appendix C contains in tabulated form the original mass of samples weighed for partial dissolution of the iron oxide using oxalic acid; the iron-oxide fraction of the original sample as filtered, captured and weighed after the reaction with oxalic acid; the mass of iron converted to weight percent; and the measured bulk Fe-oxide for the same original samples as determined via XRF. The samples of Hotazel area were excluded from this consideration due to their very high content of Mn.

Sample	Original sample (mass, g)	Fe fraction (mass, g)	Fe fraction (mass, %)	Bulk Fe oxide (wt%, XRF)
Q1	0,5221	0,5113	97,9	98,8
Q2	0,5195	0,4984	95,9	98,9
Q3	0,5097	0,5011	98,3	99,5
Q4	0,5161	0,5083	98,5	96,3
Q7	0,5233	0,5000	95,6	93,8
Q8	0,4921	0,4509	91,6	95,7
Q9	0,5295	0,4887	92,3	95,1
A1	0,5121	0,4980	97,3	98,5
A2	0,5162	0,5038	97,6	98,3
A3	0,5122	0,5043	98,5	98,3
A4	0,5134	0,4528	88,2	88,9
A5	0,5088	0,4976	97,8	98,4
A6	0,5299	0,5156	97,3	98,5
A7	0,5496	0,4397	80,0	81,9
A8	0,5486	0,4583	83,5	84,1
W2	0,5276	0,4361	82,6	85,3
W3	0,5196	0,4376	84,2	84,3
W4	0,5124	0,4926	96,1	92,9
P1	0,5298	0,5132	96,9	98,7
P2	0,5266	0,5080	96,5	95,5
P3	0,5294	0,4509	85,2	85,2
I1	0,5324	0,5010	94,1	98,0
I2	0,5395	0,5281	97,9	98,9
I3	0,5443	0,5333	98,0	98,9
HLT1	0,5298	0,4986	94,1	96,9
V1	0,5487	0,5136	93,6	96,9